OAK RIDGE
NATIONAL LABORATORY
MANAGED BY UT-BATTELLE
FOR THE DEPARTMENT OF ENERGY

ORNL/TM-2010/156

An Overview of Liquid-Fluoride-Salt Heat Transport Systems

September 2010

Prepared by
David E. Holcomb
Sacit M. Cetiner

UT-BATTELLE
ORNL-27 (4-00)

ORNL/TM-2010/156

Nuclear Science and Technology Division

AN OVERVIEW OF LIQUID-FLUORIDE-SALT HEAT TRANSPORT SYSTEMS

Author(s)
David E. Holcomb
Sacit M. Cetiner

Date Published: September 2010

Prepared by
OAK RIDGE NATIONAL LABORATORY
Oak Ridge, Tennessee 37831-6283
managed by
UT-BATTELLE, LLC
for the
U.S. DEPARTMENT OF ENERGY
under contract DE-AC05-00OR22725

CONTENTS

Page

LIST OF FIGURES

LIST OF TABLES

ABBREVIATED TERMS

AEC	Atomic Energy Commission
AHTR	Advanced High-Temperature Reactor
ANP	Aircraft Nuclear Propulsion
ARE	Aircraft Reactor Experiment
CCS	Chemistry control system
FHR	Fluoride-Salt-Cooled High-Temperature reactor
HTGR	High-Temperature Gas-Cooled reactor
HTR-10	10 MW High-Temperature Gas Cooled Reactor in China
IHX	Intermediate heat exchanger
LSHT	Liquid-salt heat transport
MSBR	Molten salt breeder reactor
MSR	Molten salt reactor
MSRE	Molten Salt Reactor Experiment
NASA	National Aeronautics and Space Administration
NGNP	Next-Generation Nuclear Plant
NHI	Nuclear Hydrogen Initiative
ORNL	Oak Ridge National Laboratory
PHX	Primary heat exchanger
SHX	Secondary heat exchanger
SSC	Structures, systems and components

EXECUTIVE SUMMARY

Heat transport is central to all thermal-based forms of electricity generation. The ever increasing demand for higher thermal efficiency necessitates power generation cycles transitioning to progressively higher temperatures. Similarly, the desire to provide direct thermal coupling between heat sources and higher temperature chemical processes provides the underlying incentive to move toward higher temperature heat transfer loops. As the system temperature rises, the available materials and technology choices become progressively more limited.

Superficially, fluoride salts at ~700°C resemble water at room temperature being optically transparent and having similar heat capacity, roughly three times the viscosity, and about twice the density. Fluoride salts are a leading candidate heat-transport material at high temperatures. Fluoride salts have been extensively used in specialized industrial processes for decades, yet they have not entered widespread deployment for general heat transport purposes.

This report does not provide an exhaustive screening of potential heat transfer media and other high temperature liquids such as alkali metal carbonate eutectics or chloride salts may have economic or technological advantages. A particular advantage of fluoride salts is that the technology for their use is relatively mature as they were extensively studied during the 1940s–1970s as part of the U.S. Atomic Energy Commission's program to develop molten salt reactors (MSRs). However, the instrumentation, components, and practices for use of fluoride salts are not yet developed sufficiently for commercial implementation.

This report provides an overview of the current understanding of the technologies involved in liquid salt heat transport (LSHT) along with providing references to the more detailed primary information resources. Much of the information presented here derives from the earlier MSR program. However, technology has evolved over the intervening years, and this report also describes more recently developed technologies such as dry gas seals.

This report also provides a high-level, parametric evaluation of LSHT loop performance to allow general intercomparisons between heat-transport fluid options as well as provide an overview of the properties and requirements for a representative loop. A compilation of relevant thermophysical properties of useful fluoride salts is also included for salt heat transport systems.

Fluoride salts can be highly corrosive depending on the container materials selected, the salt chemistry, and the operating procedures used. The report includes an overview of the state-of-the-art in reduction–oxidation chemistry control methodologies employed to minimize corrosion issues. Salt chemistry control technology, however, remains at too low a level of understanding for widespread industrial usage. Loop operational issues such as start-up procedures and system freeze-up vulnerability are also discussed.

ABSTRACT

Liquid fluoride salts are a leading candidate heat transport medium for high-temperature applications. This report provides an overview of the current status of liquid salt heat transport technology. The report includes a high-level, parametric evaluation of liquid fluoride salt heat transport loop performance to allow intercomparisons between heat-transport fluid options as well as providing an overview of the properties and requirements for a representative loop. Much of the information presented here derives from the earlier molten salt reactor program and a significant advantage of fluoride salts, as high temperature heat transport media is their consequent relative technological maturity. The report also includes a compilation of relevant thermophysical properties of useful heat transport fluoride salts. Fluoride salts are both thermally stable and with proper chemistry control can be relatively chemically inert. Fluoride salts can, however, be highly corrosive depending on the container materials selected, the salt chemistry, and the operating procedures used. The report also provides an overview of the state-of-the-art in reduction-oxidation chemistry control methodologies employed to minimize salt corrosion as well as providing a general discussion of heat transfer loop operational issues such as start-up procedures and freeze-up vulnerability.

1. INTRODUCTION

1.1 PURPOSE AND SCOPE

The purpose of this document is to provide an integrated overview of the engineering aspects of high-temperature, liquid-salt heat transfer (LSHT) systems. Development of LSHT systems inherently requires consideration of issues across a broad span of engineering disciplines due to the high temperatures and the consequent chemical and physical properties of the materials involved. A considerable body of knowledge has been developed describing specific scientific and technical aspects of the materials and components comprising LSHT systems. This report integrates information from the more narrowly focused preexisting literature into a practice oriented engineering overview of the state-of-the-art in LSHT system practice and design.

As with any heat transfer fluid fluoride salts have distinctive chemical and physical properties that necessitate particular operational practices, component designs, and materials selection. The interrelated set of issues involving structural material creep strength, work hardening, salt purity, corrosion, and reduction–oxidation (redox) chemistry remain the most technically challenging aspect of employing liquid salts for heat transfer. A primary purpose for this report is thus describing the state-of-the-art in the materials science for LSHT.

Despite century-long, widespread, high-volume industrial use often at temperatures above those proposed for power generation cycles, liquid fluoride salts are perceived as impractical or unproven. The focus of one report section is thus on assembling existing liquid-fluoride-salt industrial experience into an illustrative summary. The rapid advance of materials and automation technologies over the past few decades offers the potential to simplify and lower the cost for LSHT systems. Thus an interwoven theme throughout the report is documentation of recent and likely near-term system advances that offer potential cost and performance improvements over historical implementations.

This report is organized to first provide a conceptual overview of LSHT system design and operational issues to enable development of rapid system scoping estimates. The report then provides an evaluated summary of the existing technical literature on required technologies for LSHT systems. Next the report subdivides LSHT systems into heat transfer modeling and simulation, components and instruments, salt chemistry and corrosion control, and operational practices providing a state-of-the-art overview of each as a separate section. The report scope includes the both the LSHT system as well as the energy transfer interface with the salt from and to high pressure, high-temperature gas systems. The report is limited to heat transfer from and to helium, helium-nitrogen mixtures, carbon dioxide, and/or other liquid fluoride salts and does not address the materials compatibility issues arising from loop interconnection to more corrosive environments.

1.2 SYSTEM CONCEPTUAL OVERVIEW

The ever-increasing demand for higher system thermal efficiency necessitates power generation cycles transitioning to progressively higher temperatures. Similarly the desire to provide direct thermal coupling between heat sources and higher temperature chemical processes provides the underlying incentive to move towards higher temperature heat transfer loops. As the system temperature rises, progressively fewer and fewer material combinations remain candidates for the loop. The requirement to operate at above 700°C (and the desire to continue to accommodate progressively higher temperatures) eliminates all but a few materials from consideration. An earlier evaluation of molten salt reactor secondary coolants provides a broad overview of the requirements and issues for a similar heat transfer loop albeit focusing on somewhat lower temperatures. [1]

Design decisions within the possible material combinations arise from a combination of heuristics (avoiding highly toxic or highly reactive materials and maintaining a low system pressure), quantitative

comparisons (minimizing pumping power, reducing heat transfer area, minimizing raw material cost, etc.), and engineering judgment about technological difficulties of system development (e.g., developing a high-temperature, lead compatible structural alloy appears impractical). Liquid salts stand out as the most advantageous overall heat transfer media when all design considerations are applied. Explaining this judgment and quantifying how liquid fluoride salts fulfill the requirements for high temperature heat transport forms the body of this report.

Functionally, all heat transfer loops consist of a heat source, a heat sink, and a heat transfer mechanism. A simplified overview of an LSHT loop is shown in Fig. 1. As a single-phase, incompressible liquid, the loop also is required to have an expansion volume. A drain tank is also necessary to enable initial filling and to allow for servicing. Since the fluoride salts have melt points well above ambient, loop preheating is also required. Further, chemistry control is required since fluoride salts only maintain their relatively inert nature when the free fluorine potential is minimized. In addition, since a primary purpose for an LSHT loop is to physically separate two energetic processes (possibly at high pressure) sufficient physical loop length is required to prevent severe accidents (blast wave, fire, caustic chemicals) from propagating between the heat source and heat sink processes and pressure relief mechanisms are required to prevent the liquid salt itself from propagating the accident. Additionally, when the heat source is nuclear reactor security requirements will necessitate either applying nuclear power level security to the heat sink process plant or providing sufficient distance between the reactor and the process plant to incorporate a security boundary.

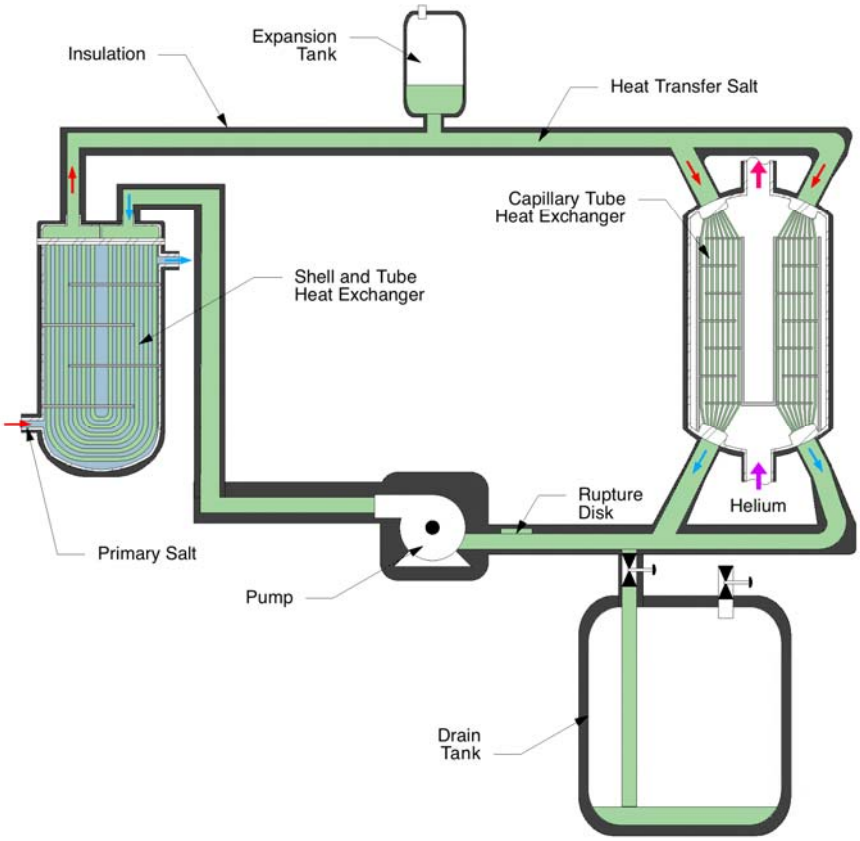

Fig. 1. Schematic drawing of a liquid-salt heat transport system.

1.3 SUMMARY OF PRIOR EXPERIENCE WITH LIQUID FLUORIDE SALTS

1.3.1 Aluminum Smelting

The largest industrial use of liquid fluoride salts is as the alumina solvent in the Hall-Héroult process for the electrowinning of aluminum from a cryolite (Na_3AlF_6) bath. The Hall-Héroult process was developed in the late 19th century and has been in continuous, progressively increasing usage since then. Currently, more than 30 million tons of aluminum is produced each year via this high-temperature (roughly 1000°C), liquid-fluoride bath based technique.

The aluminum industry has over the past century developed simple, robust techniques for large-scale industrial use of liquid fluoride salt. [2] Several aluminum industry practices are of particular note. The primary aluminum reaction pot employs a frozen wall of cryolite to protect the structure behind it. Similarly, a frozen top crust of cryolite is employed as thermal insulation, an evaporation barrier, as well as to minimize the interaction of the fluoride salt with moisture in the air. These frozen surface techniques combine to make a virtue of the salt's inherent high melting point, protecting container materials while minimizing interaction of the liquid salt with the environment. Aluminum smelters also employ a fume exhaust hood routed to a water bath maintained at an elevated pH to capture and neutralize the small remaining amount of evaporation from the salt pool.

1.3.2 Molten Salt Reactor Program

Investigation of molten salt reactors started in the late 1940s as part a U.S. program to develop a nuclear powered airplane. Molten fluoride salts were adopted in 1950 as the mainline effort of the Aircraft Nuclear Propulsion (ANP) program. In carrying out this program, much information on the physical, chemical, and engineering characteristics of molten salt systems was obtained from studies of fluoride salt chemistry and materials compatibility, and from development of components, materials, fabrication methods, and reactor maintenance processes. In 1954, the Aircraft Reactor Experiment (ARE), a 2.5-MW(t) MSR fueled with UF_4 dissolved in a mixture of zirconium and sodium fluorides, moderated with beryllium oxide, was built and operated successfully for 9 days at steady-state outlet salt temperatures approaching 900°C. No mechanical or chemical problems were encountered, and the reactor was found to be stable and self-regulating.

The MSR program was initiated in 1957, drawing upon the information developed in the ANP program as well as beginning new lines of investigation. By 1960, favorable experimental results were obtained to support authorization for design and construction of a 10-MW(t) Molten Salt Reactor Experiment (MSRE). Design of the MSRE started in the summer of 1960, and construction started at the beginning of 1962. The reactor went critical in June 1965, and the MSRE initiated power operation in early 1966. The MSRE provided facilities for testing fuel salt, graphite, and Hastelloy N under reactor operating conditions. The basic reactor performance was outstanding and indicated that the desirable features of the molten salt concept could be embodied in a practical reactor that could be constructed, operated, and maintained safely and reliably.

The MSR development program operated numerous test loops over the course of its life. Of note the secondary cooling loop for the MSRE operated for in excess of 26,000 hours (mostly between 530 and 650°C) and showed negligible corrosion upon eventual disassembly. Most of the primary heat transport components necessary for a modern LSHT loop were developed and demonstrated. Technology evolution, however, has improved the format of many of these components. Also, since high-power Brayton electricity generation cycles were not yet available the interface between the low-pressure salt and high-pressure gas was not demonstrated.

1.3.3 Fusion First Wall Program

$LiF\text{-}BeF_2$ (67-33 mole %), commonly called flibe, is a candidate material for use as an advanced blanket material in fusion reactors. Most recently, the Japan–U.S. collaborative program, JUPITER-II (2001–2006), included flibe handling, reduction-oxidation corrosion control, and thermofluid flow experimentation and numerical analysis [3]. Of particular note, in the late 1970s, the U.S. fusion program studied the impact of reduction–oxidation control on corrosion providing support for the concept that if the salt can be kept in a sufficiently reducing condition the salt corrosion of stainless steel is slow [4].

1.3.4 Electrodeposition

Electrodeposition of refractory metals from molten salt baths is becoming more commonplace [5]. Both LiF-NaF-KF (46.5-11.5-42 mole %), commonly called flinak, and $LiF\text{-}CaF_2$ are often used as plating baths. As early as 1929 liquid salts were considered for the deposition of TiB_2 on Inconel [6]. Refinement of the techniques employed has been under continuous development from the 1970s onward. Copper, chromium, and niobium, as well as the actinides have all been electrodeposited from fluoride melts. While electrodeposition from fluoride melts remains at laboratory or small commercial scale the high elemental solubility, wide electrochemical window, low toxicity, high heat capacity, and high-temperature tolerance of the liquid fluoride salts is gradually increasing their frequency and volume of use.

2. STRUCTURES, SYSTEMS AND COMPONENTS FOR LIQUID FLUORIDE SALT HEAT TRANSPORT LOOPS

2.1 OVERVIEW OF COMMON STRUCTURES, SYSTEMS AND COMPONENTS

The primary function of a heat transport system is to transfer energy from one system to another. To provide a general overview of the heat transport processes, a generic heat transport loop is assumed in this report. Structures, systems and components (SSC) that are common to any heat transport system are included in the engineering analysis for figure of merit calculations.

A generic heat transport loop consists of the following components: (1) heat source, (2) heat sink, (3) pump, (4) piping and insulation.

The heat source can be the reactor core, where the fluoride salt comes in direct contact with the heat generation mechanism; or it might be a heat exchanger where two fluids exchange heat, but are not allowed to intermix. This formalism provides a generic means for systems analysis without loss of generality. A similar rationale applies to the heat sink.

For the Next-Generation Nuclear Plant/Nuclear Hydrogen Initiative (NGNP/NHI), the heat source would be the secondary heat exchanger (SHX), whereas the heat sink would be the process heat exchanger (PHX) in the proposed hydrogen production plant coupled to a high-temperature gas reactor (HTGR) [7].

Detailed system design is outside the scope of this report. Basic system performance calculations are provided to present a rough overview of system scale, and to enable comparison between design options. More extensive and elaborate sensitivity and trade studies would be required before embarking on a system design.

Recently, ORNL published a technical report that identifies the component testing requirements for fluoride-salt-cooled high-temperature reactors (FHRs) [8]. This report includes a detailed listing of components that are essential for proper operation of the plant. Below, we provide a tailored overview of these components focusing on their heat transport performance.

2.1.1 Heat Source and Heat Sink

For a LSHT system, the heat source is expected to be a heat exchanger coupled to an intermediate heat exchanger, which couples to the reactor primary system. A number of trade studies on options for connecting a heat transport system to a Next Generation Nuclear Plant (NGNP) for the purpose of producing hydrogen have been performed [7]. In Reference 7, seven configuration options were identified and a series of performance analyses was conducted. The selected configurations included both direct and indirect cycles for the production of electricity. All the options included an intermediate heat exchanger (IHX) to separate the operations and the safety functions of the nuclear and hydrogen plants. For the heat transport system that transfers heat from the reactor to a hydrogen production facility, both helium and liquid salts were considered as the working fluid. The study concluded that the liquid salts offer significant advantages as the working fluid especially for transferring more power to the hydrogen production facility. Although engineering development challenges for designing a liquid-salt-based system were recognized, it was also concluded that the safety risks are greatly reduced primarily because of the possibility of delivering high efficiency near atmospheric pressures.

Based on high-level engineering analysis, out of seven configurations, four options were eliminated and three were down selected for further consideration. One of the viable options used a direct electrical cycle—the primary fluid is sent directly to the turbines for electricity generation—

and a parallel IHX as shown in Fig. 2. The process heat exchanger (PHX), which delivers heat to the hydrogen production facility, is directly connected to the IHX. This configuration offers the smallest mass and the highest thermal efficiency. In this configuration, the heat is transferred from the primary helium to the liquid salt through the IHX interface.

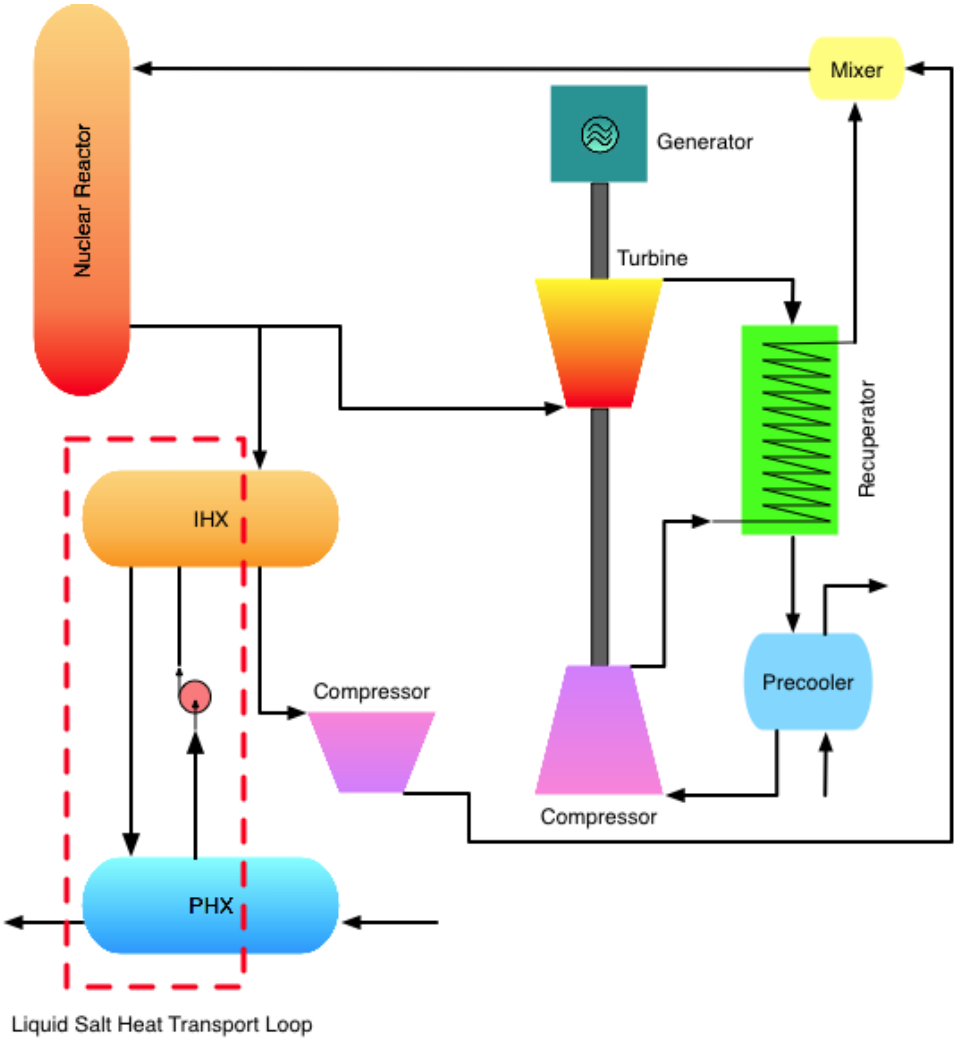

Fig. 2. Possible configuration option for a liquid salt heat transport loop—direct electrical cycle and a parallel intermediate heat exchanger (IHX).

Another option similar to the above used an indirect electrical cycle. The process heat exchanger (PHX) was connected to a secondary heat exchanger (SHX), which is then connected to the IHX, as shown in Fig. 3. This configuration provided the better separation between the nuclear island and the process facility. Because of additional components, this option turned out with the largest mass and the lowest thermodynamic efficiency—within the down-selected options—as expected. However, considerations such as operation and license acquisition may favor this option notwithstanding the increased cost and engineering complexity.

The advantage of the configuration shown in Fig. 3 is the possibility of using another working fluid for the power cycle. Recent design studies using supercritical CO_2 (S-CO_2) demonstrate that

these systems can deliver electricity with a high thermal efficiency [9]. If the LSHT loop is connected to a heat source in this configuration, the heat is transferred from the secondary fluid to the liquid salt via a secondary heat exchanger (SHX).

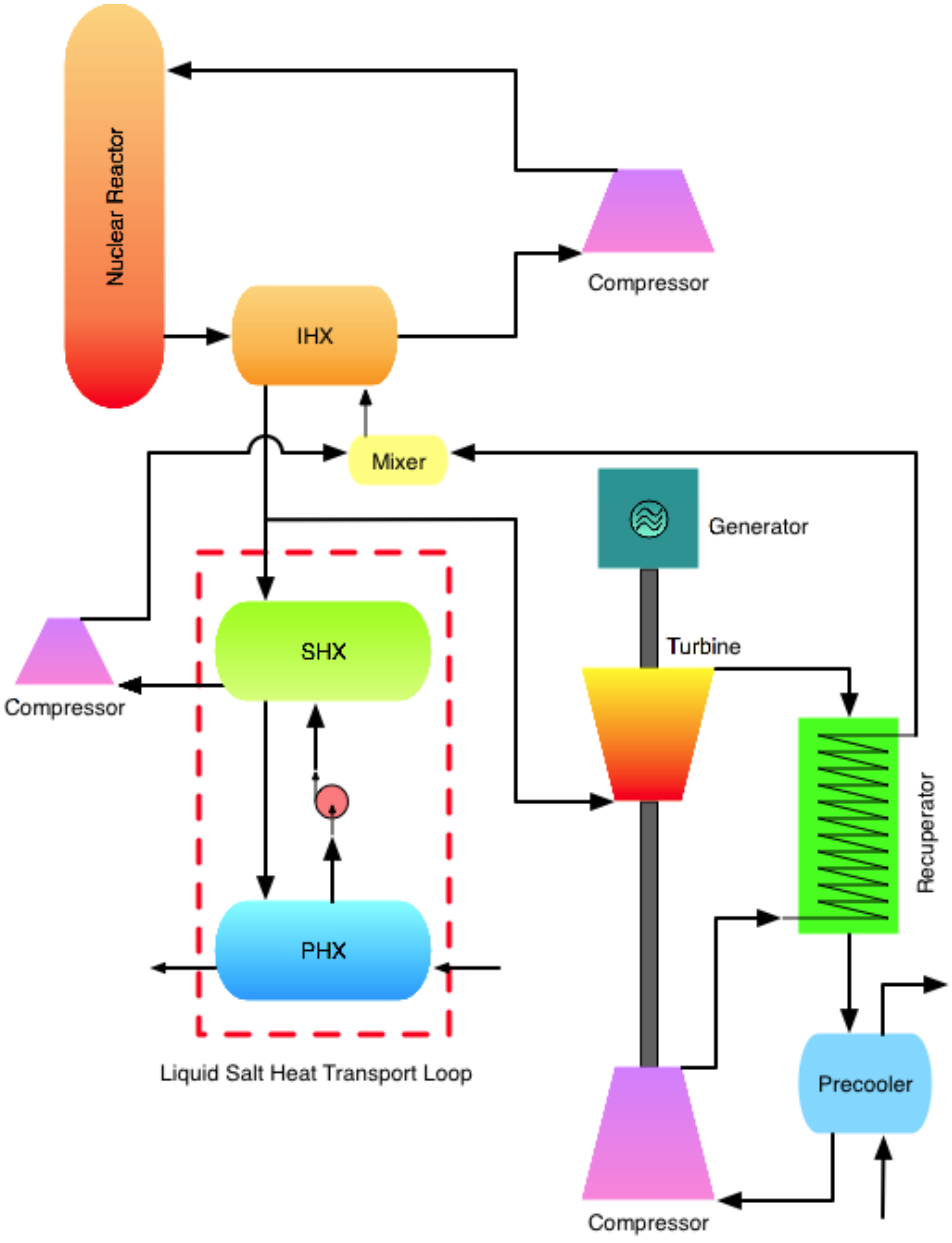

Fig. 3. Possible configuration option for a liquid-salt heat transfer loop—indirect electrical cycle and a parallel secondary heat exchanger (SHX).

The heat sink is a process facility that utilizes the heat delivered by the liquid-salt heat transport system. The heat is transferred to another medium through a process heat exchanger (PHX), as shown in Fig. 2 andFig. 3.

2.1.2 Piping and Insulation

Liquid salt systems operate at near atmospheric pressures, which eliminate the thick-walled pressure boundaries. This advantage greatly reduces the piping mass required. On the other hand, liquid salts have different interaction mechanisms with container materials than do the conventional fluids, as described in Sect. 3.2 in further detail. Thus, material selection is a key design aspect of any liquid-salt-based system.

A number of materials are generally compatible with liquid fluoride salts. Molybdenum, nickel, and carbon are all thermochemically stable to liquid fluoride salts. Hastelloy N (a limited-chromium nickel-based alloy) was developed specifically for liquid fluoride salt operation as part of the MSR program. Hastelloy N offers excellent chemical compatibility to over 700°C with fluoride salts and is the material presumed to be used as the loop structural material by this report.

Fluoride salts expand upon melting. It is therefore important to allow piping to drain before a loop is allowed to cool. Essentially the liquid salt cannot be allowed to freeze into a solid plug blocking the piping. The viscosity of liquid fluorides is only a few times that of liquid water, thus, the salt drains well and a combination of gravity draining and inert gas purging can be employed to prevent plug formation.

Because of very high operating temperatures, the piping must be furnished with sufficient insulation to minimize parasitic heat losses. As the pipe insulation does not contact the liquid salt, standard high-temperature pipe insulation can be used.

2.1.3 Liquid Salt Pumps

The primary function of the pump is to provide the mechanical energy to circulate the fluid for effective removal of heat. The fluid—the liquid fluoride salt in this context—experiences irreversible losses as it flows, which the pump has to recover.

Considerable operating experience with liquid salt pumps was obtained during the Molten Salt Reactor Experiment (MSRE) and Molten Salt Breeder Reactor (MSBR) test programs.

The liquid salt pumps used in the prior program were mechanical, free-surface, centrifugal, vertical-shaft sump pumps. The liquid salt pumps are generally divided into two groups:

1. Pumps with a short shaft with the impeller overhung, and
2. Pumps with a long shaft with at least one support bearing located in the pumped fluid.

The pump used in the primary loop of the MSRE was a vertical short-shaft sump pump with an overhung impeller and an oil-lubricated face seal [10]. A cross-sectional drawing of the MSRE fuel salt pump is shown in Fig. 4. It consists of three main components: (1) the pump tank, (2) the rotary assembly, and (3) the drive motor. The main components were bolted together and sealed with oval ring-joint gasketed flanges. The ring-joint grooves were connected to a leak detection system. The motor and rotary assembly could be removed from the pump tank either as a unit or separately.

The MSRE pump tank provided volume to accommodate thermal expansion of the salt within the system. The tank primarily contains the pump volute or casing, a xenon-removal spray device, salt level indicators and various access nozzles. The rotary assembly consists of the bearing housing, the pump shaft, the shaft seals, the shield plug and the pump impeller.

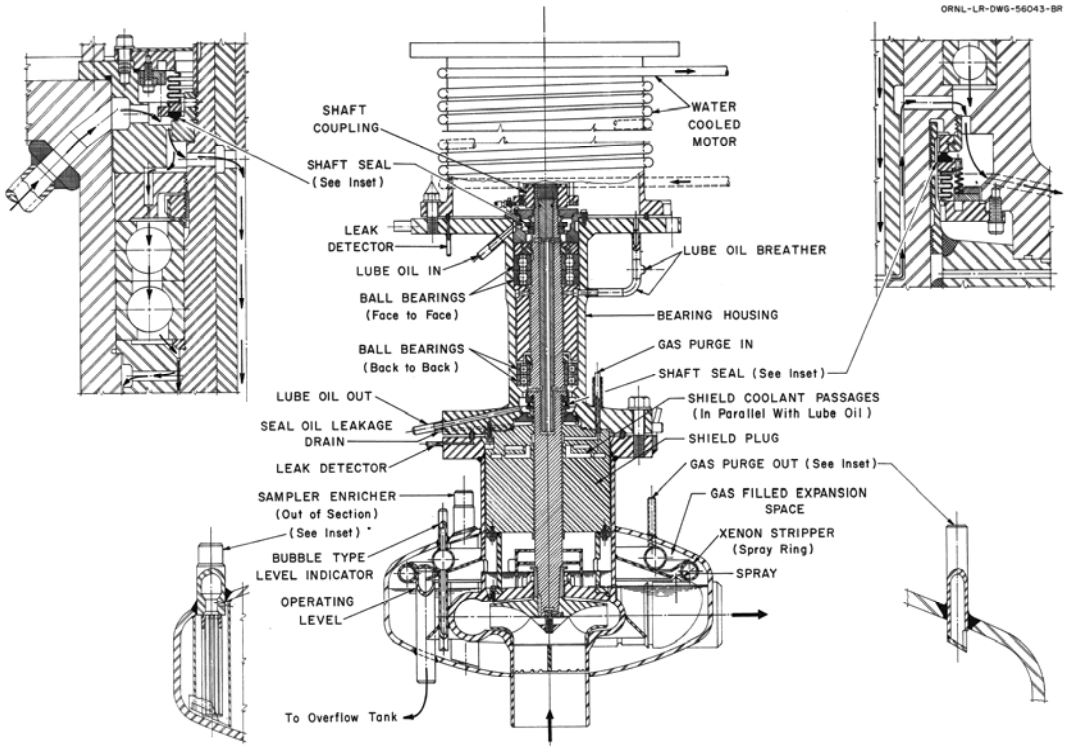

Fig. 4. MSRE fuel pump.

The second group, long-shaft pumps, generally includes reactor sodium pumps for various sodium fast reactors. A liquid salt pump of this type was designed and operated at ORNL. Long-shaft pumps have shaft support adjacent to the impeller provided by a journal bearing that is lubricated with the pumped fluid. This permits the use of long shafts to separate the drive motor and its sensitive electrical insulation, and hydrocarbon lubricant from the intense radioactivity of dissolved-fuel molten salt reactors as well as from high temperature.

Because the LSHT loop will not be highly radioactive development of long-shaft pump technology is not considered critical.

2.2 SUPPORT SYSTEMS AND COMPONENTS

An LSHT loop interconnecting to a high-pressure system will also include the following: (1) loop preheating system, (2) fill and drain system, (3) chemistry control system, (4) expansion tank, (5) rupture disk, and (6) instrumentation. The following sections will provide high-level description of these systems and the operating experience from the earlier salt programs.

2.2.1 Loop Preheating System

The loop preheating system consists of hot-gas blowers and/or electrical resistance-type heaters, heater mounting fixtures, power supplies and controllers, temperature sensors and temperature control instrumentation required to heat the liquid-salt-containing components. Loop preheating systems are required for systems with heat transfer fluids that are solid at ambient temperatures such as sodium fast reactors. The Power Reactor Innovative Small Module (PRISM), for instance, used a *Sodium Piping and Equipment Heating and Insulation System* to provide a similar functionality [11].

The loop preheating system preheats the solid metal parts of the loop at controlled heat-up rates before the systems are filled with liquid fluoride salt from ambient conditions to roughly 100ºC above

the liquidus temperature of the heat transfer salt. This system is also used to heat the salt process system from extended shutdown conditions to loop operating conditions in accordance with prescribed heat-up rates with the loop filled with liquid salt.

Key requirements in the loop preheating system design include the following: (1) equipment is heated up at similar rates such that temperature differences are minimized and kept within design limits, (2) thermal stress levels are accounted for in establishing the maximum allowable unheated length of piping, and (3) failure of the loop preheating system is not allowed to impair the safety function of associated systems and components.

The liquid salt temperature is maintained indefinitely at sufficiently high temperatures with an engineering margin. This is achieved by overcoming all heat losses, from normal heat leakage paths as well as from ongoing process functions, and accounting for all heat sources including the frictional heat from operating pumps. In that regard, the loop preheating system is intricately linked to piping insulation to limit piping and support component heat losses to the environment, and maintain insulation surface temperatures within acceptable limits.

The loop preheating system should be furnished with design provisions to bring the heat transport loop from potential freeze-out conditions resulting from planned or unplanned interruptions. This is achieved by applying heat to the frozen salt from a free surface to allow expansion of the fluid during the phase change.

Loop preheating can be achieved by circulation of hot gas, by operation of the electrical heat tracing units, or both. In the MSRE, preheating was accomplished by circulation of helium in the primary system using the fuel pump as an inefficient blower. Heat is introduced through use of the electric resistance heaters installed throughout the primary and secondary systems. The operation of the loop preheating system as part of the loop startup procedure is further explained in Sect. 5.1.

2.2.2 Fill and Drain System

The fill and drain system provides for the safe storage of the heat transport salt when the system is not in the circulating mode—such as during a scheduled maintenance. It is also used during the initial filling of the loop. Filling is achieved via application of an inert cover gas overpressure into the drain tanks. The loop inventory is simply transferred to the drain tanks by gravity

Once in the drain tanks, the salt temperature is maintained above the liquidus temperature. The tanks are kept at above atmospheric pressure with the inert gas—such as argon—to prevent the inleakage of moisture and oxygen.

The MSRE used a single drain tank for the coolant salt. This tank resembled the fuel-salt drain tank, as shown in Fig. 5, except that it was smaller and it had no thimbles or cooling system. The tanks were provided with devices to indicate high and low liquid levels and with weigh cells to indicate the weight of the tanks and their components. The tanks were installed in insulated furnaces, which are heated with electrical resistance heaters to maintain salt liquidity.

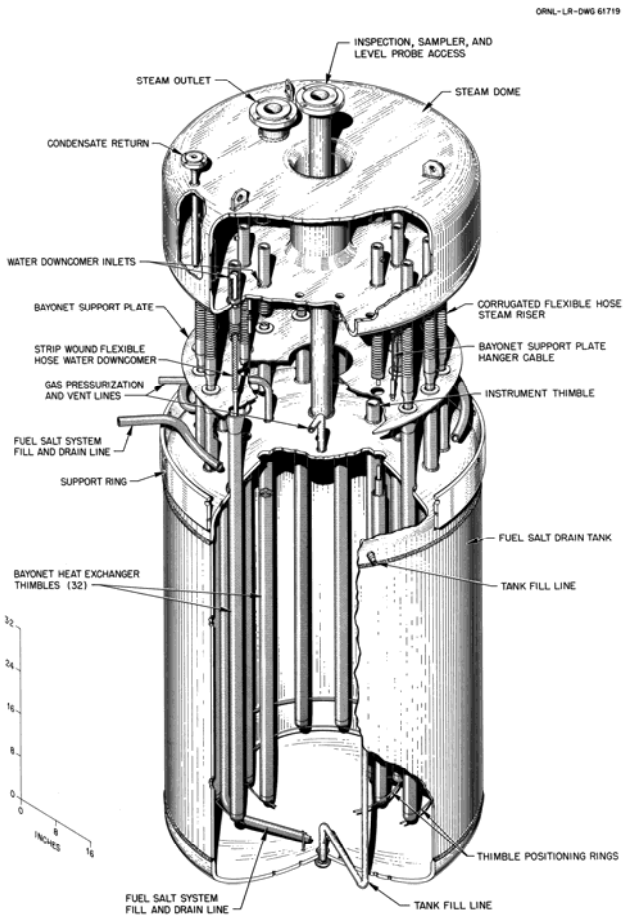

Fig. 5. Fuel-salt drain tank of the MSRE.

Considering the separation between the heat source and the heat sink, an LSHT system will have much larger fluid inventory compared to the MSRE. Though no definitive design exists for such a system, considering the volume of the inventory, it is anticipated that multiple drain tanks will be provided. Since the salt will drain simply by gravity, pipe sections should be installed with a few-degree tilt for proper drainage of the fluid.

2.2.2.1 Valves

Valves provide means for controlling the flow of liquid salt. The primary function of valves in the fill and drain system is to isolate the drain tanks from the loop during operation. Opening of the valves allow transfer of salt from the heat transport loop to the drain tanks, or vice versa.

Most circulating fluid systems use mechanical valves. Challenges to the use of mechanical valves include general material compatibility in a fluoride salt environment and operating temperatures. Fluoride salts are excellent fluxing agents, thus self-welding and galling are important design issues for valve seats and actuator seals.

To date most fluoride-salt circulating systems have avoided the use of mechanical valves. Freeze valves (discussed below) have been used, or the system is designed to operate without valves (such as controlling flow by adjusting pump speed rather than through a control valve). For common reactor applications such as containment isolation, however, mechanical valves may be needed to meet performance requirements such as actuation time or capacity to isolate larger diameter pipes.

An alternative to the mechanical cutoff valve is provided by a freeze valve. In a freeze valve, salt contained within a flattened section of pipe is either cooled below its freezing temperature by a stream of air or other coolant, or melted by electric heaters. For the freeze valves used in the MSRE, the time required to freeze a valve varied from 5 to 30 minutes depending on the starting temperature, and the time required to thaw varied from less than 15 minutes up to several hours depending on the mode of operation of the valves at the time of the demand.

An example freeze valve used on the drain lines in the MSRE is shown in Fig. 6. Extensive experience exists with freeze valves. As long as the stress produced in thermal cycling during freeze-thaw operation is properly managed, these valves perform well.

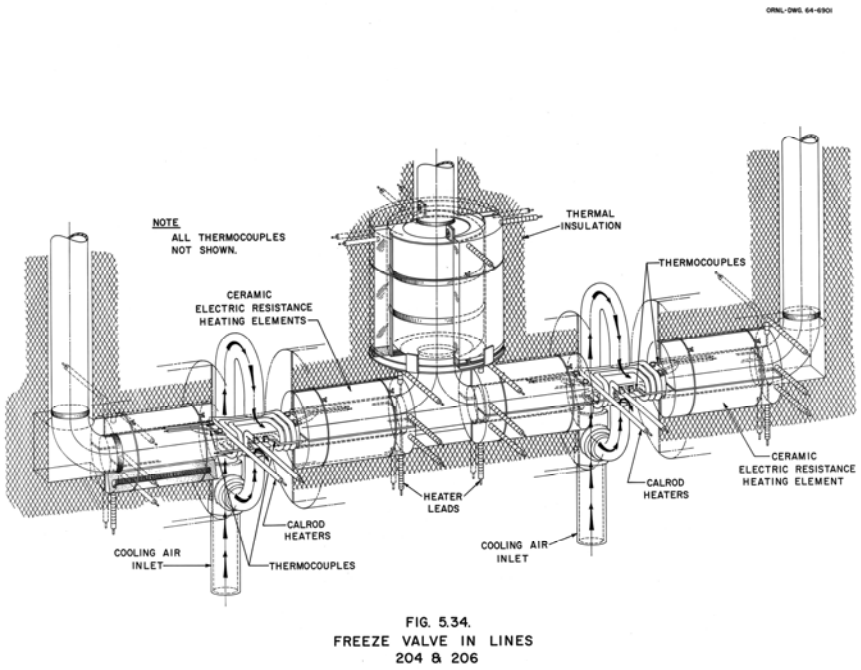

Fig. 6. A freeze valve design used in the MSRE.

2.2.3 Chemistry Control System

Long-term operation of the any LSHT loop relies heavily on maintaining the purity and low fluorine potential of the fluoride salt. Although high-purity fluoride salts can have low corrosive properties to engineering alloys, fluoride salts can become much more corrosive when contaminated by water vapor or oxygen.

The main function of the Chemistry Control System (CCS) is to maintain the desired composition and thereby to minimize the fluorine potential of the liquid fluoride salt. Oxygen is a competing electronegative element to fluorine and its level in the salt should be minimized to reduce salt corrosivity. Salt corrosion chemistry is described in further detail in Sect. 3.2 of this report. The CCS diverts a side stream from the heat transport loop, which is processed with an HF/H_2 or NF_3 purge to remove oxygen contamination. In this purge, fluorine-bearing gas is bubbled through the salt along with hydrogen gas, which chemically reacts with oxygen to produce water vapor and replaces oxygen with fluorine. The salt cleanup techniques employed in the CCS are essentially identical to those employed in initial preparation of the salt as described in Sect. 3.3.

2.2.4 Expansion Tank

Expansion tanks are commonly employed in single-phase flow systems to provide additional free volume for the fluid to tackle deviations from nominal operating conditions. These are typically the situations where salt specific volume varies slightly during transients such as temperature excursions or due to more gradual changes in the chemical composition of the salt. The expansion tank provides free surface for the salt in an inert gas environment—such as argon. The gas pressure can be regulated by a simple controller to keep the system pressure in a specified operating envelope, or a burst valve can be attached as a safety device to avoid overpressurization of the loop.

The MSRE provided the expansion volume and the free surface for the primary salt within the volute of the primary pump. A similar approach can be adopted for the salt heat transport system to avoid the cost of having extra components. The advantages and disadvantages of providing a separate expansion volume should be studied in detail, probably supported by some failure modes and effect analyses as well as economic analyses for a risk-vs-cost assessment.

2.2.5 Rupture Disks

Rupture disks are safety-related components to protect the heat source from pressure waves. Sudden pressure increases might result from a breach in an interface component that is coupled to a high-pressure system such as a steam generator or a salt-to-gas heat exchanger. Since the LSHT loop operates at near atmospheric pressures, such a failure would result in significant fluid ingress from the high-pressure system. A rupture disk provides a relief path for the high-pressure excursion, preventing failure of more expensive, safety-related components. The relieved fluid can be collected in a large-volume tank, or can be released to the atmosphere, depending on the nature and environmental compatibility of the fluid.

2.2.6 Instrumentation

The operational instrumentation requirements for liquid salt systems differ from other more conventional industrial applications primarily in that the transducers need to survive the high-temperature, fluoride salt environment.

A liquid salt heat transport environment typically requires measurement of basic process variables such as temperature and flow. Coolant chemistry measurements—as a corrosion indicator—and component health monitoring are also important for longer-term operation. For most process variables, several alternate measurement approaches are possible. This report includes overview descriptions of the principal candidate measurement approaches.

Temperature measurement is both indicative of process conditions as well as a primary component of the energy transfer measurements. Thermocouples are the most common transducer for process condition measurement. However, base metal thermocouples lack the long-term accuracy necessary for the heat balance measurements. Two optical instruments potentially have the stability and accuracy required to support efficient electricity generation. Both fiber optic coupled pyrometry and Fizeau cavity type thermometers are candidate technologies for high-accuracy temperature measurement. Ultrasonic wireline thermometry is also a strong candidate technology for low-uncertainty temperature measurement at elevated temperatures.

Although the field of ultrasonic temperature measurement has many embodiments, wireline, pulse-echo ultrasonic sensor is especially applicable to aggressive environment temperature measurement due to its rugged nature. Ultrasonic wireline thermometry has been demonstrated as early as the 1960s in nuclear applications within as severe an environment as molten corium [12]. A

review of the technology stressing nuclear power applications was published in 1972 [13]. More recently Lynnworth provided a detailed overview of ultrasonic probe temperature sensors [14].

Ultrasonic wireline thermometry is based upon the change in the velocity of sound within a wire with temperature. The speed of sound in a wire varies with its elastic modulus and density as described in

$$v(T) = \sqrt{\frac{Y(T)}{\rho(T)}} \tag{2.1}$$

where $Y(T)$ represents Young's modulus and $\rho(T)$ represents density of the waveguide, both as a function of local temperature. Although both parameters are temperature dependent, the temperature effect on elastic modulus dominates by about an order of magnitude over that of density, which causes sound velocity to decrease with increasing temperature.

Ultrasonic wireline temperature measurement begins by launching an extensional acoustic wave down a waveguide. The return time of reflections of the launched wave pulse is then recorded. The wireline contains a series of notches. The time difference between reflections from each notch is indicative of the temperature between the notches (Fig. 7).

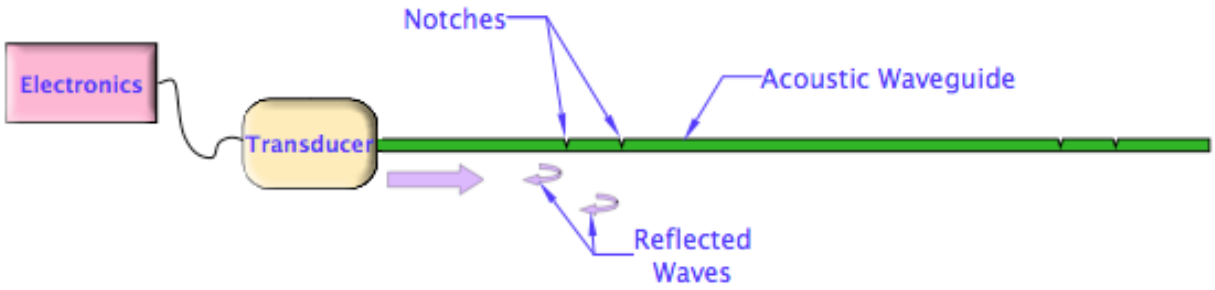

Fig. 7. An ultrasonic thermometry system including a notched waveguide.

Liquid-salt flow measurement will most likely either be performed using external, ultrasonic flowmeters or Venturi-type flowmeters that use differential pressure gauges as their active element. Ultrasonic flowmeters, as shown schematically in Fig. 8, are widely used across the industry due to their low uncertainty and stability. External ultrasonic flowmeters for high temperatures are semicommercial with remaining development and demonstration of the thermal buffer rods and pipe coupling required to become a fully commercial component. Both optical- and capacitive-type diaphragm deflection measurement techniques are candidate technologies for high-temperature implementation. The high temperature of the salt environment requires that mechanical standoffs be used to limit the ultrasonic transducer temperature exposure.

The differential pressure gauges required for Venturi-base flow measurement either require diaphragm deflection measurement tolerant of LSHT temperatures or impulse line interconnection between a high-temperature and a low-temperature diaphragm using a lower melt temperature fill material such as a lead bismuth eutectic. Optically based diaphragm deflection measurement is the leading candidate for direct, high-temperature implementation. Stoichiometric silicon carbide based

micro-electro-mechanical systems are a leading material candidate for forming the high-temperature tolerant, salt compatible pressure gauge bodies. However, a commercial pressure measurement technology that can be directly used in a high-temperature fluoride-salt environment is not yet available.

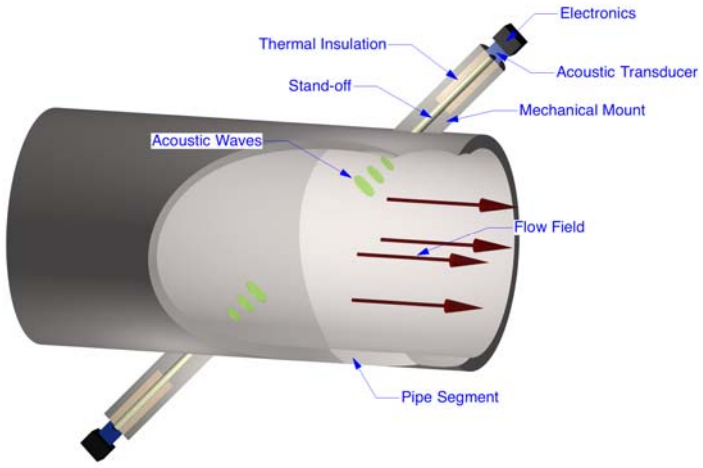

Fig. 8. Schematic representation of an ultrasonic flowmeter and its operating principle.

2.3 EMERGING COMPONENT TECHNOLOGIES

The major challenges to designing and operating a liquid-salt heat transport system come primarily from the mechanical and chemical considerations. Interactions of the salt with the container material—pronounced at elevated temperatures—create deleterious effects for components, particularly so for rotating equipment. For instance, proper design of bearings and seals has always been a determining parameter for successful operation of high-temperature systems.

These challenges are mostly attacked by incorporating fundamental physical and chemical provisions into the design (e.g., compatible material development). Technological advances in the last two decades also offer potentially viable paths to incorporate ingenious options into the design without compromising the safety case of the system. Following sections provide brief descriptions on a few example component technologies, namely canned rotor pump technology and dry gas seal technology that can be used in liquid salt systems. Some of these technologies have already been deployed in other high-temperature systems, and can be adapted for liquid-fluoride-salt service with reasonable development efforts.

Other technological advances that can be taken advantage in liquid-fluoride-salt systems include heat exchanger technologies. Examples are printed-circuit heat exchangers, formed-plate heat exchangers and hybrid heat exchangers. These components are generally formed from alternating layers, typically hot–cold–hot. These heat exchanger designs offer the possibility of smaller footprint and—potentially—lower capital cost. However, no experience exists in designing, constructing and operating these systems with liquid salts at high temperatures. A technology maturity evaluation was previously published on various emerging component technologies in a previous report [8], including novel heat exchanger technologies; hence, they will not be repeated here.

Another component technology that would potentially improve design and operation of liquid salt systems is the mechanical valve technology. To date, no single mechanical valve design has been demonstrated to meet the safety and operating requirements for liquid salt service, though significant research and development efforts were put in during the ANP and MSBR programs. Recently, some research focus is being directed at development of high-temperature mechanical valves for liquid salts by the U.S. Department of Energy [15].

2.3.1 Canned Rotor Pumps

A study of the problems of applying the canned-rotor motor and the short-shaft and long-shaft configurations of the centrifugal pump to molten salt service was made in 1967 [15]. The canned-rotor pump was concluded to be a very desirable configuration, since there are no orientation or elevation limitations on its application. However, it would require difficult and expensive development to provide pumps for an MSBR application including the development of a high-temperature electric motor with an electrical insulation system that also has a very high resistance to nuclear radiation damage.

Demonstrating integrated measurement and control of active magnetic bearings is a key technology to ensure successful transition to modern pumping systems. Oil leaks within circulator seals have been a major historic problem for gas, liquid-metal, and liquid-salt-cooled reactors. High-temperature canned rotor pumps and/or circulators are under development as a response to this problem. These types of systems often employ multiple active magnetic bearings that require thousands of position measurements each second. Such a demonstration should be made with a representative scale pump to show that active control can be applied under high temperature environments and with prototypic materials.

The canned-rotor pump configuration eliminates the requirement for a vertical pump shaft, avoids the vibration issues of mechanical bearings that are remote from the impeller, does not require seal gas, provides absolute mechanical sealing, but does require more advanced control algorithms and elevated temperature motor windings.

In a canned rotor pump, the rotor of the pump motor is located within the liquid and a thin walled container is located between the rotor and the stator. The rotor is prevented from mechanically contacting the container by the use of active magnetic bearings. In a liquid salt pump, the rotor can is the pump housing. Within the pump housing the stator and its wiring is isolated from the salt environment. The stator container wall is kept thin on the side facing the rotor and fabricated from a low conductivity metal to minimize the eddy currents generated within the wall. Enveloping the stator and its wiring within a shield avoids requiring sealed, multi-conductor electrical penetrations for the stator electromagnet drives as well as chemical compatibility issues between the electromagnet winding insulation and stator itself with the liquid salt.

HTGR vertical shaft turbine generators such as planned for the HTR-10 pebble-bed reactor employ magnetic bearings nearly identical to those anticipated for a liquid salt pump [17]. The electromagnets of HTGRs need to be fully enclosed within the helium pressure boundary because of the almost complete efficiency loss that would result from having to magnetically couple through the thick pressure boundary.

A reluctance type motor is the most likely choice for a liquid-fluoride-salt-type motor because of the high salt temperature. Reluctance motors do not require permanent magnets, rotor windings, or inlaid conductors all of which are problematic at high temperature. Of particular concern, all available permanent magnets lose their magnetic stiffness by 550°C. Above this temperature, only soft magnetic materials, such as those used in reluctance motors, are available [18]. Since the stator

windings are at high temperature ceramic insulation is required. Ceramic-coated wire has been a commercially available technology for several decades now.

A potential system configuration would be a reluctance drive, canned rotor type motor whose shaft drives the impeller of a centrifugal pump. Much of the required internal mechanical structure for the magnetic bearings is inherent in the rotor. An axial cross section of a three-phase, four-pole-per-phase reluctance motor with two perpendicular active magnetic bearings is shown in Fig. 9.

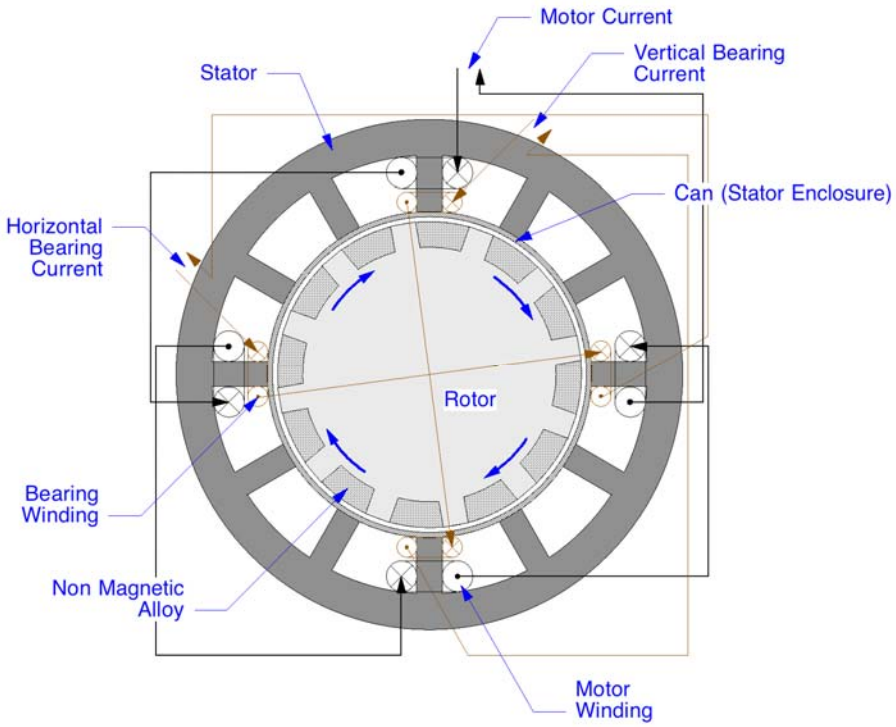

Fig. 9. Reluctance motor cross section showing A-phase motor windings and bearing windings.

2.3.1.1 Catcher Bearings

Catcher bearings are mechanical backups to the magnetic bearings to prevent catastrophic pump failure in the event of loss-of-shaft active positional control. The catcher bearings are positioned just beyond the acceptable magnetic bearing position control envelope and are designed to restrain the impeller shaft sufficiently to allow the shaft to spin down without damage following loss of active control. The advent of salt compatible ceramic bearings combined with the good salt lubrication properties decreases the catcher bearing design difficulty. However, catcher bearing design remains a significant engineering issue [19].

2.3.1.2 Bearing and Drive Control

Active magnetic bearing suspension is based upon varying the drive current to electromagnets based upon rotor displacement measurements. Shaft horizontal and vertical position is independently measured at each radial bearing-motor set. Rotor position measurement can be performed by monitoring the change in the resonant frequency of a driven coil located near the rotor due to the shift in position of the magnetic rotor material.

For the three-phase radial bearings illustrated in Fig. 9, each electrical phase provides suspension across two axes resulting in a threefold redundancy along each of the controlled axes. The thrust

bearing shown in does not have an equivalent natural redundancy and a complete replicate thrust bearing is required to provide redundant, active axial position control. Axial thrust bearings do not have an equivalent natural redundancy, hence complete replicate thrust bearing is required to provide redundant, active position control.

Depending on the specific design requirements, pump shafts can rotate rapidly (thousands of revolutions per minute). The combination of turbulent fluid motion and rapid impeller rotation typically results in vibration frequencies up to roughly 10 kHz. Further, even minor imperfections in the impeller balance or in the rotor position sensor targeting can result in the control system itself enhancing the inherent oscillations. Additionally, bearing-control response frequency needs to exceed the maximum credible vibration frequency to damp high-frequency impeller oscillations.

The power electronics have the highest failure probability of any component in a magnetic bearing system. For the described radial bearings, each electrical phase has two bearing control power supplies for a total of six power supplies for each bearing-motor set. Only two of the six power supplies are required to control the shaft position. If a power supply to an electromagnet fails its control axis will no longer be restrained. However, both of the other electrical phases can supply radial thrust at 30° and 60° offsets from the direction of the failed control axis. The remaining magnetic bearings thus need to combine to provide a vector force sum that continues to maintain the rotor within its control envelope. Key to preventing the pump shaft from impacting the container (and possibly failing catastrophically) is thus recognizing that control has been lost along an axis and rapidly compensating for the lost axis of radial position control.

Power supply failure can be measured independently of rotor position by monitoring the output current and voltage often through the power supply's built-in feedback control circuitry. Further, power supply aging and incipient failure can often be ascertained by a combination of temperature and voltage ripple monitoring. Due to the required response time (<100 μs), control failure monitoring will need to be implemented using a local dedicated logic module.

An improperly implemented fault response can accentuate the improper rotor acceleration driving the rotor into the catcher bearings resulting in gross system failure. Fault tolerant active magnetic bearing design control design remains an active development area [21].

2.3.2 Dry Gas Seals

Existing liquid salt pump designs derive chiefly from the prior U.S. Atomic Energy Commission (AEC) program to develop molten salt reactors (MSRs). The MSR era pumps were vertical shaft centrifugal pumps with external motors. External motor pumps require both bearings and seals to transfer both radial and axial forces and separate the interior and exterior environments. Both pumps with oil lubricated bearings outside the shaft seal (referred to as cantilever pumps) and with salt lubricated bearings were employed during the MSR program era. Salt lubricated metal bearings were a significant source of corrosion concern.

At the time of the MSR program oil-film, floating-ring seals were the state-of-the-art sealing technology. Oil film floating ring seals are radial seals, sealing the radial space between a rotating shaft and a stationary seal. Radial seals require a very high degree of precision to prevent contact between the stationary and rotating parts. In practice, somewhat larger clearance is allowed with radial seals making them vulnerable to sealing fluid leakage. Shaft seal leaks have been the root cause of significant historic problems in the nuclear industry. Lubricated end-face seals were next in the evolution of sealing technology. In an end-face seal the actual sealing surfaces are perpendicular to the rotating shaft enabling the faces to contact each other and dramatically improving the seal quality.

Dry gas seals were the next in the evolution of shaft sealing technology. Dry gas seals are gas-lubricated, mechanical, noncontacting, end-face seals. In a dry gas seal the seal is formed between a

stationary primary and rotating mating ring. The key innovation to enable dry gas sealing was the development mating rings with machined grooves half of the radial distance across the face of the seal ring as shown in Fig. 10. When the shaft is rotating, sealing gas is injected from the exterior radius of the sealing rings. The shaft rotation compresses the sealing gas at the tapered tips of the mating ring grooves. The elevated gas pressure causes the primary and mating rings to separate slightly (few microns). A small amount of gas leaks through the seal. The primary ring is spring loaded against the mating ring, so that when the shaft is not rotating the two rings are in tight contact. As the grooves in the mating ring do not extend across its entire mating surface, the two rings form a tight seal and seal leakage is prevented.

Fig. 10. Dry gas seal mating ring.

Dry gas sealing has now become commonplace dominating the commercial marketplace for applications where fluid purity is key or human contact with the fluid needs to be avoided. For a vertical shaft pump a combination of a labyrinthine seal and a dry-gas seal will separate the salt environment from the external motor environment. Shaft bearings can be either immersed in the salt or above the gas seal. This dry-gas seal configuration has the advantage of employing a low-temperature motor possibly with magnetic bearings to minimize wear and friction.

2.4 A PARAMETRIC ANALYSIS FOR THE HEAT TRANSPORT SYSTEM

The following calculations provide a highly simplified analysis of the design and comparative operational aspects of the several heat transfer fluid options for a high-temperature loop. The calculations are not of sufficient detail or fidelity design purposes and are intended only to illustrate the overall implications of selecting a particular heat transfer fluid. Physical parameters used in the calculations are listed in Table 1.

Table 1. Thermophysical parameters for fluids included in the analysis

Fluid	ρ (kg/m^3)	c_p (kJ/kg K)	ρc_p (kJ/m^{3}K)	$\mu \times 10^4$ (Pa s)	k (W/m K)
Flinak	2019.9	2.01	4060	29	0.60
Sodium	790	1.27	1000	1.9	62.0
Water[a]	732.3	5.49	4018	0.9	0.56
Steam[b]	37.4	4.73	176.9	0.2	0.063
Helium[c]	3.7	5.26	19.34	0.5	0.29

[a]7.5 MPa, 290ºC
[b]7.5 MPa, 300ºC
[c]7.5 MPa, 700ºC

The heat rating of the source was arbitrarily taken to be $\dot{Q} = 125$ MW(t), which is consistent with the value range considered for the Small Modular Reactor size. The temperature rise across the heat source for each fluid is listed in Table 2. The rationale for selecting this particular set of temperature rises was based on the fluid properties. All fluid calculations were performed for an average fluid temperature of 700ºC, except for water—calculated at 290ºC—and steam—calculated at 300ºC. Flinak and sodium were considered at near atmospheric pressure; while water, steam and helium properties were taken at 7.5 MPa. A functional block diagram of a representative heat transport loop was shown in Fig. 1.

Table 2. Selected temperature rise values for fluids included in the analysis

Fluid	ΔT (ºC)
Flinak	50
Sodium	100
Water	100
Steam	200
Helium	400

Estimates for required separation distance between the heat source and the heat sink (e.g., nuclear reactor and hydrogen production facility), vary considerably based on the design and safety criteria used [7]. In this study, the separation distance was taken to be 500 m, which gives a total pipe length of L = 1,000 m.

2.4.1 Flow Requirements

The volumetric flow rate Q in m^3/s is calculated from the total energy balance using

$$Q = \frac{\dot{Q}}{\left(\rho c_p\right)\Delta T} , \tag{2.2}$$

where $\dot{Q}$ is the thermal rating of the heat source in W, $\left(\rho c_p\right)$ is the volumetric heat capacity in J/m^{3}K and ΔT is temperature rise across the heat source in ºC. The mass flow rate $\dot{m}$ in kg/s is calculated using

$$\dot{m} = \rho Q . \tag{2.3}$$

The required pipe diameter D that satisfies the flow rate and bulk fluid velocity requirements can be calculated by

$$D = 2 \sqrt{\frac{Q}{\pi V}} . \tag{2.4}$$

where V is the bulk fluid velocity in m/s.

For an estimation of the pipe diameter, a parametric analysis has been performed as a function of bulk fluid velocity using the $\dot{Q}$ value of 125 MW(t) and ΔT values from Table 2. The fluid velocity is varied to find a channel dimension that yields a reasonable pumping power. Table 3 provides the results of the analysis—also plotted in Fig. 11. Values listed in bold indicate those combinations of fluid velocity and pipe diameter considered most reasonable.

Table 3. Required pipe diameter with respect to bulk fluid velocity

Bulk velocity (m/s)	**Pipe diameter** (m)				
	Flinak	**Sodium**	**Water**	**Steam**	**Helium**
0.1	2.80	3.99	1.99	6.71	14.34
1.0	**0.89**	**1.26**	**0.63**	2.12	4.54
2.0	**0.63**	**0.89**	**0.45**	1.50	3.21
5.0	**0.40**	**0.56**	**0.28**	**0.95**	2.03
10.0	0.28	0.40	0.20	**0.67**	**1.43**
20.0	0.20	0.28	0.14	**0.47**	**1.01**
50.0	0.13	0.18	0.09	0.30	**0.64**
100.0	0.09	0.13	0.06	0.21	0.45

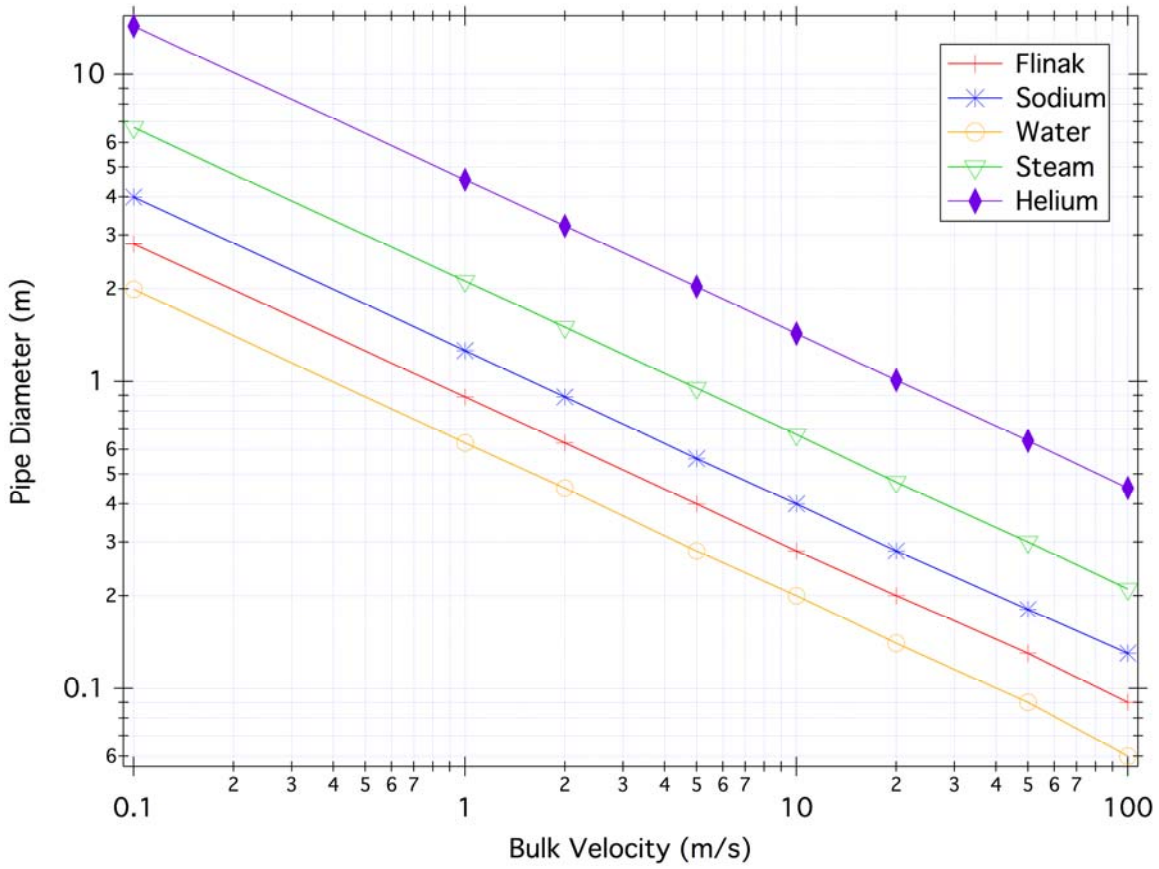

Fig. 11. Variation of pipe diameter as a function of bulk fluid velocity.

Note that the piping wall thickness—a primary piping cost differentiator—is not included in this estimate. The amount of metal volume necessary for the heat transport system piping can be calculated by

$$\mathbf{V}_{\text{pipe}} = \frac{\pi}{4}\left[(D+2w)^2 - D^2\right] L \ , \tag{2.5}$$

where $\mathbf{V}_{\text{pipe}}$ is the metal volume of the piping in m^3, D is the pipe inner diameter in m, w is the wall thickness of the pipe, and L is the total length of the pipe. With some algebraic operations, Eq. (2.5) can be reduced to

$$\mathbf{V}_{\text{pipe}} = \pi\, L\, w\, (D+w) \ . \tag{2.6}$$

Since the pipe length is fixed, for sufficiently large pipe diameters (i.e., $w \gg D$), it is possible to state

$$\mathbf{V}_{\text{pipe}} \propto w \ . \tag{2.7}$$

The high-pressure water, steam or helium systems will require much thicker piping walls than do the low-pressure sodium and flinak. As shown in Eq. (2.7), the piping mass will increase in proportion with the wall thickness resulting in higher capital expenses—with all other considerations being similar.

2.4.2 Pressure Loss

The two main components of pressure drop along the flow loop are frictional and form pressure drops. The form losses for the loop estimate consist of eight 90-degree pipe bends between the heat source and the heat sink. The friction pressure drop is calculated by

$$\Delta p_{fric} = f \left(\frac{L}{D} \right) \frac{\rho V^2}{2} , \tag{2.8}$$

where f is the friction factor, L is the channel length, D is the pipe diameter.

The form pressure drops are irrecoverable energy losses due to sudden change in geometry of the channel or direction of the fluid. They are calculated using

$$\Delta p_{form} = K \frac{G^2}{\rho} , \tag{2.9}$$

where K is the form factor, G is the mass flux in kg/m^{2}s and ρ is the fluid density. The form factor for 90-degree turns typically varies between K = 0.4–0.9 [20]. In the calculations, K = 0.9 was used as the form factor value. The total pressure drop is the sum of frictional and form pressure drops. Fig. 12 shows the variance of the loop pressure drop with the fluid velocity for each of the evaluated heat transport media.

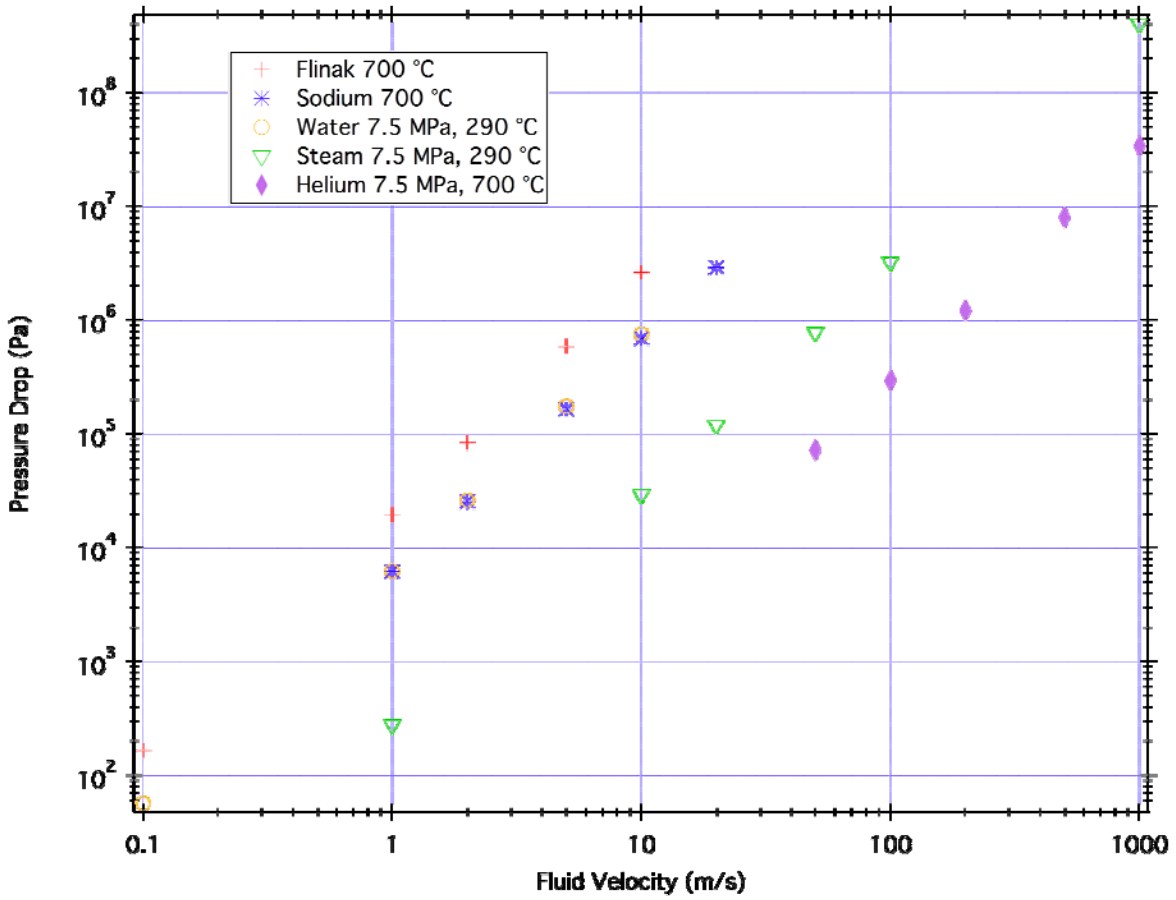

Fig. 12. Variation of total pressure drop with respect to bulk fluid velocity.

2.4.3 Pumping Power

The required hydrodynamic pumping power is calculated using the following equation:

$$P_{pump} = Q\,\Delta P_{total}\ , \tag{2.10}$$

where P_{pump} is the pumping power in kW, Q is the volumetric flow rate in m^3/s, and ΔP_{total} is the total pressure drop in Pa.

Table 4 lists the key quantities calculated with respect to the parameterized bulk fluid velocity for a number of fluids that can be considered as the heat transport medium. Pump power calculations do not include head losses due to elevation differences between heat source and the heat sink.

The pressure drop (markers), pumping power (solid lines) and resulting fluid velocity (dashed line with markers) for each candidate fluid to transfer the required amount of heat as a function of pipe diameter is shown in Fig. 13.

Table 4. Calculated thermal fluid quantities for selected fluids at various bulk velocities

V (m/s)	D (m)	Δp_{fric} (kPa)	Δp_{form} (kPa)	Δp_{total} (kPa)	P_{pump} (kW)
Flinak					
1.00	0.89	3.22	14.5	17.8	10.9
2.00	0.63	16.7	58.2	74.9	46.1
5.00	0.40	147	364	511	315
10.0	0.28	764	1450	2220	1370
Sodium					
1.00	1.26	0.52	5.69	6.20	7.75
2.00	0.89	2.67	22.8	25.4	31.8
5.00	0.56	23.5	142	166	207
10.0	0.40	122	569	691	864
Water					
1.00	0.63	0.97	5.27	6.24	1.94
2.00	0.45	5.01	21.1	26.1	8.12
5.00	0.28	44.2	132	176	54.8
10.0	0.20	229	527	756	235
Steam					
10.0	0.67	3.69	26.9	30.6	108
20.0	0.47	19.1	108	127	448
50.0	0.30	169	673	842	2970
Helium					
10.0	1.43	0.31	2.65	2.96	47.8
20.0	1.01	1.60	10.6	12.2	197
50.0	0.64	14.1	66.2	80.3	1300

These calculations were not performed based on optimal parameters.

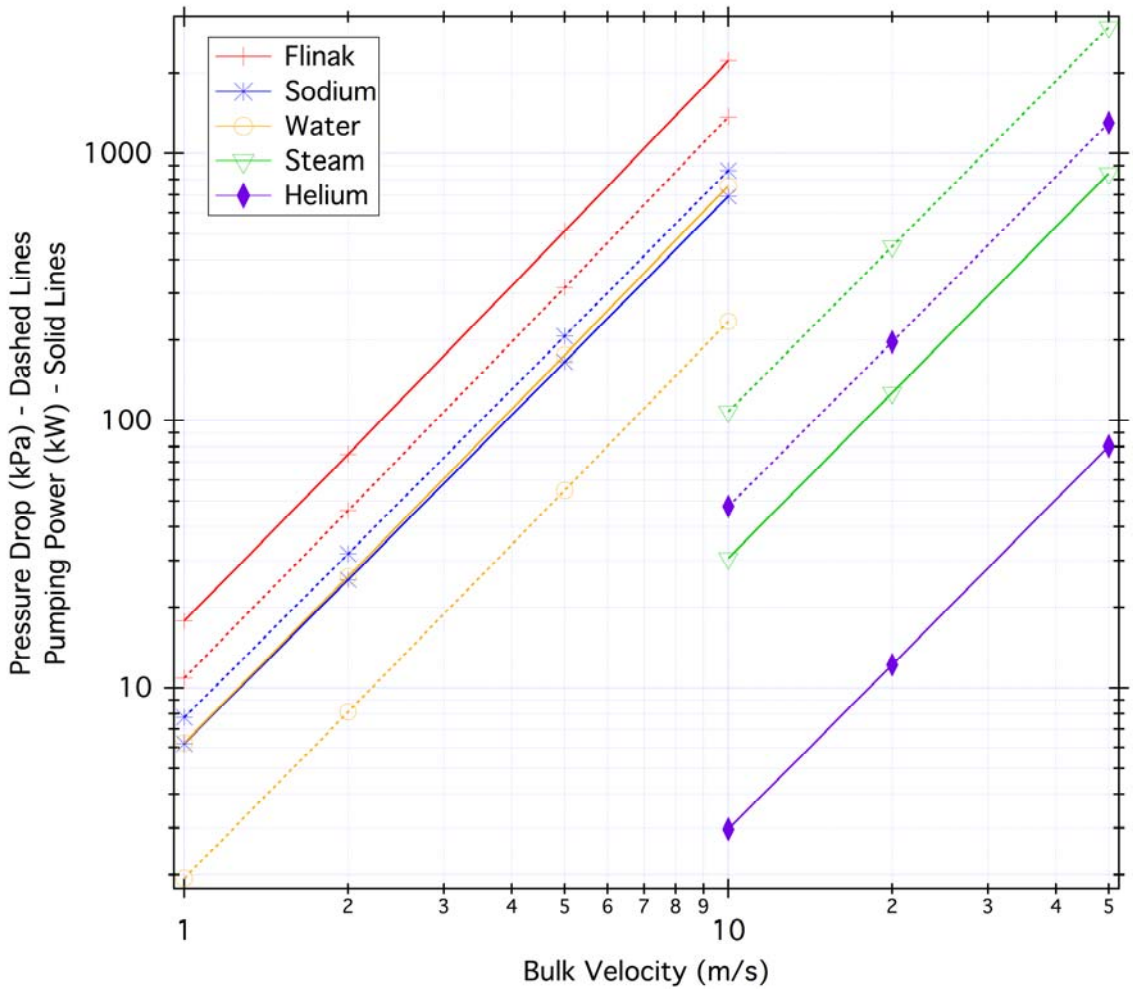

Fig. 13. Required pumping power for selected fluids as a function of fluid velocity.

2.5 OTHER ISSUES

A critical point of discussion in systems that contain liquid salts is the issue of salt freeze-out. The amount of time it takes for the salt to reach the onset of freezing is important, the magnitude of which determines the complexity of engineering design of support systems. The following section provides a rough engineering calculation for estimating the time it takes the liquid salt to reach the freezing point from the operating temperatures.

2.5.1 Salt Freeze-Out

This section provides a basic analysis of the time necessary for an LSHT loop line with reasonable size and insulation to begin to freeze up. In the simulation, the pipe was considered infinitely long. As an approximation, the isothermal processes have been neglected; only isobaric energy transfer is assumed—which is a reasonable assumption when the entire salt mass is liquid. This assumption is no longer valid if the fluid undergoes phase change.

The selected geometric parameters of the thermal system are shown in Fig. 14. The pipe diameter was selected based on the parametric thermal fluid analysis as discussed in the previous section. As

listed in Table 4, a pipe diameter of 400 mm required approximately 300 kW of pumping power for circulation of the fluid against friction and form losses—not including the head losses between the heat source and the heat sink, and the efficiency of the pump. This value was considered reasonable and taken as the base geometric parameter in this calculation.

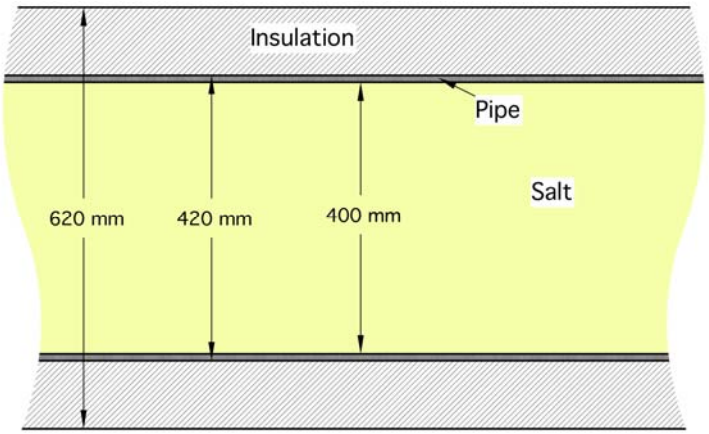

Fig. 14. Geometric parameters used in the freeze-out calculations.

The pipe wall thickness was taken to be 10 mm. Considering the fact that the liquid salt heat transport loops operate under near-atmospheric pressures, wall thickness is expected to be relatively small compared to pressurized systems. Because metals have considerably high thermal conductivity, a reasonable range of pipe wall thickness has essentially no impact on simulations. Industrial-grade mineral wool was used as the insulation material with 100-mm thickness. A parametric analysis was also performed to observe the sensitivity of the rate of heat loss on insulation thickness. The insulation was considered exposed to air. Flinak was used as the working fluid for the analysis.

The thermal model is shown in Fig. 15. Natural convection is the only mode of heat exchange between the insulation and the air. Impact of radiative losses is expected to be insignificant [REF UW]. The mode of heat exchange in the insulation and the pipe is conduction. Both conduction and natural convection modes are included in the analysis for salt heat transfer. Radiation mode can have some impact on the analysis, but has not been included in this simulation.

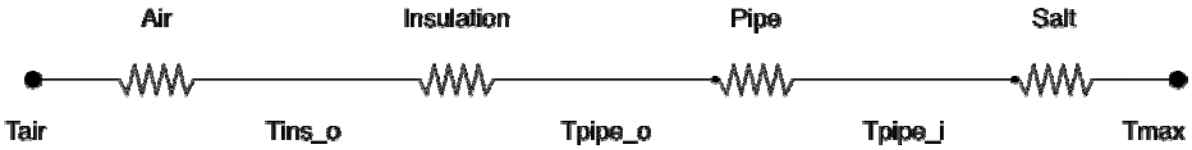

Fig. 15. Electrical circuit analogy of the thermal model used in the analysis.

The entire salt mass is assumed to lose energy uniformly at each time step of the simulation. This is a simplification of the process to achieve a gross estimate of the time required for the onset of salt freeze-out. Salts in general—and flinak in particular—have considerably high volumetric heat capacities and relatively low thermal conductivities, which results in comparatively low thermal diffusivities. Therefore, it takes longer for heat waves to propagate during a transient. In liquid metals, this dynamics is much faster.

All transients analyzed in the simulations assume that the pump coast-down is immediate compared to the process time constant, and no heat is added to the system, which provides a lower bound for the time to freeze-up.

The variation of bulk flinak temperature against time is plotted in Fig. 16. The initial fluid bulk temperature was selected 700ºC—the loop nominal hot leg temperature. With these parameters, the onset of freeze-up (flinak freezes at 454ºC) was calculated to be approximately 110 h into the transient. Time for complete crystallization of the salt is not included in this result.

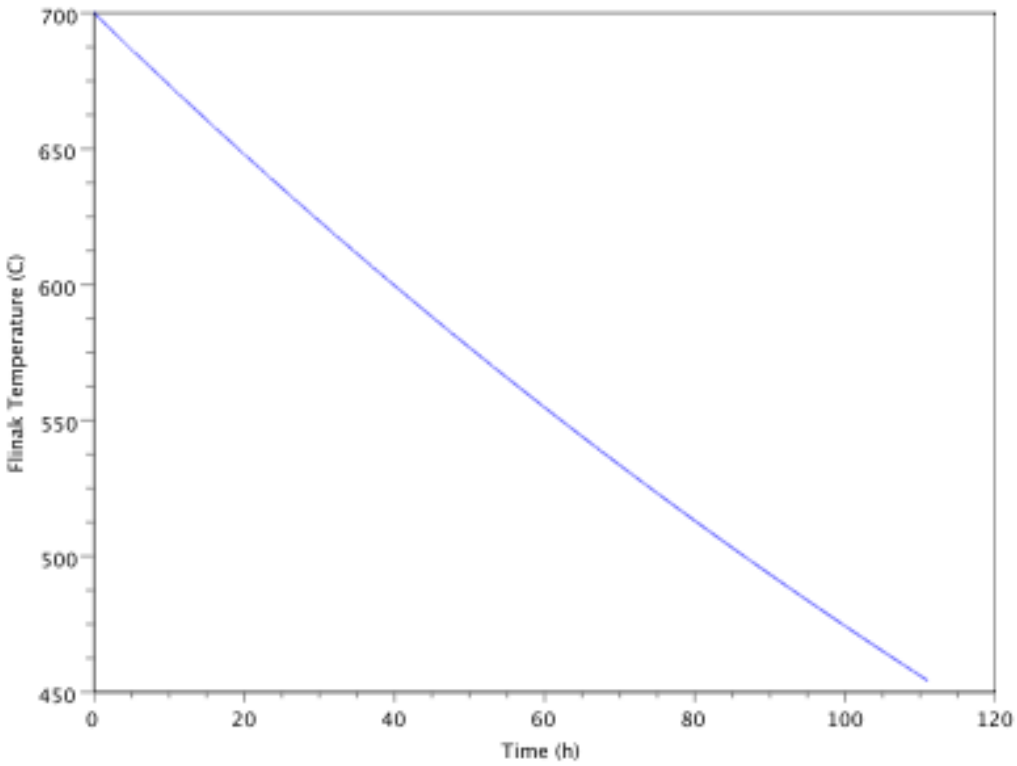

Fig. 16. Variation of bulk flinak temperature as a function of time.

The loop cold leg temperature is expected to be approximately 550ºC. Time to onset of freeze-up can also be found from Fig. 16 by subtracting the time required for bulk salt temperature to reduce from 700ºC to 550ºC, which yields approximately 50 h.

This computational model fails two critical phenomena: (1) the effect of phase change on the progress of heat transfer and (2) the effect of geometry changes at interfaces, such as connections, components, etc. First, the salt will naturally start to freeze from the periphery, and the solidification will progress toward the interior regions, as more heat is lost to the environment. This will results in gradual degradation of heat transfer because the solid salt will lose the natural convection heat transfer mode, which is expected to result in a larger heat resistance. For this reason, the results presented here can be considered conservative because the natural convection heat transfer mode was considered effective throughout the simulations.

The thermal model used in the calculations was based on an infinitely long horizontal pipe; therefore, no interfacial effects were taken into account. Components along the path of the flow will create geometric discontinuities, which might reduce the effectiveness of insulation resulting in

additional leakage paths for internal heat. This can be alleviated by better insulation design and component heat tracing.

The previous simulation was performed with a nominal pipe diameter of 400 mm. To investigate the impact of varying pipe diameters, a simulation was performed with the insulation thickness fixed at 100 mm, the initial bulk temperature of 700ºC, and varying pipe diameter. The result of the simulation is plotted in Fig. 17. As one would expect, the time required for the salt volume to come to the onset of freeze-up varies almost linearly with pipe diameter—except for small diameters. The result is consistent with the physics of heat transfer primarily because the surface-to-volume ratio is inversely proportional to the pipe diameter, and it increases as the pipe gets smaller resulting in more leakage per unit volume of salt.

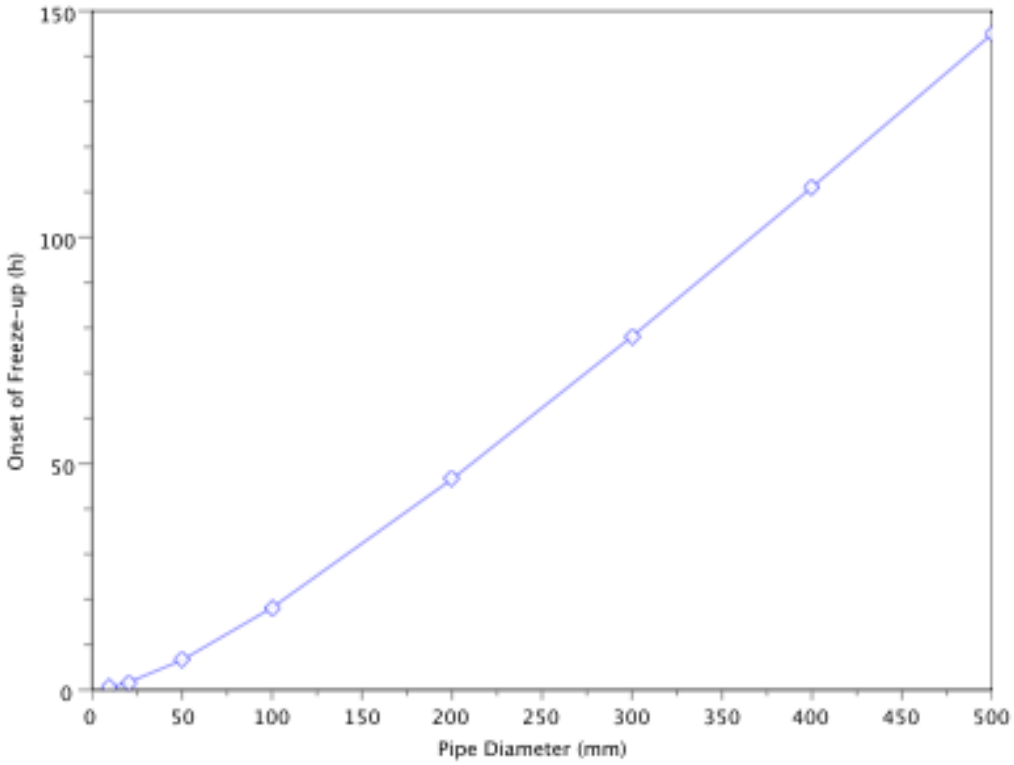

Fig. 17. Onset of salt freeze-up as a function of pipe diameter (100-mm insulation).

The effect of varying insulation thickness for a fixed pipe diameter (400 mm) is shown in Fig. 18. This simulation also uses 700ºC as the initial bulk fluid temperature. As seen in figure, the time to onset of freeze-up increases rapidly as the insulation thickness increases. The selection of insulation thickness will obviously be driven by material cost.

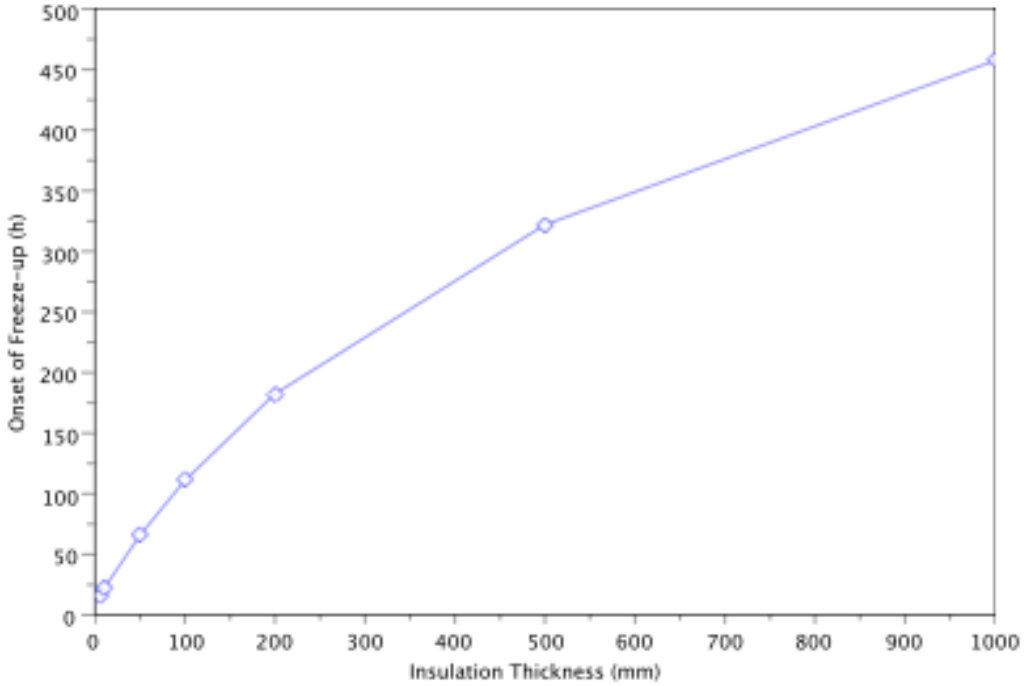

Fig. 18. Onset of salt freeze-up as a function of insulation thickness (400-mm-diameter pipe).

This simple thermal simulation suggests that, for a liquid salt heat transport system with proper amount of insulation, it would take days for the fluid inventory to come to freeze-out temperatures. This window gives operators sufficient time to transfer the salt into a storage canister, where it can be kept in liquid state with reasonable heat input. Partial heat tracing—particularly for regions where higher heat losses are expected such as the interconnections—might be necessary.

3. FLUORIDE SALT PROPERTIES AND CHEMISTRY

3.1 THERMOPHYSICAL PROPERTIES OF FLUORIDE SALTS

An extensive survey of thermophysical properties of fluoride salts was made by Williams for the NGNP Nuclear Hydrogen Initiative (NGNP/NHI) [22] and for the Advanced High Temperature Reactor (AHTR) [23]. Following sections provide a synopsis from these reports.

3.1.1 Melting Point

An extensive database of phase diagrams exists for salt systems of all types [24]; therefore, there is very little need to pursue estimation techniques. Because no single-component salt freezes at a sufficiently low temperature, multicomponent mixtures of salts are required. Nearly all of the binary phase diagrams of interest have been measured, and many of the ternary systems have also been investigated. In general, the primary lowering of freezing point (as much as 500ºC) occurs with the addition of the first salt to a pure component. Additional lowering of the freezing point can be achieved by adding a third component, but these freezing point depressions are of a lower order (~50ºC). Additional components are typically important for reasons other than lowering the freezing point, such as cost or some other physical or chemical property.

Salts that are useful as secondary coolants have been identified in previous reports [25–27]: (a) alkali fluorides, (b) ZrF_4 salt mixtures, (c) fluoroborate salts, and (d) chloride salts. This report focuses primarily on fluoride salt; hence, chloride salts have been excluded. Table 5 lists the primary eutectic compositions in each salt family in order of freezing point. Phase diagrams and properties of the alkali fluorides and ZrF_4 salt mixtures were discussed in Ref. 22.

Table 5. Useful salt compositions and eutectic temperatures for the NGNP/NHI heat transport loop

	Compound	Molar composition (%)	Melting point (ºC)
Alkali Fluorides	LiF-NaF-KF	46.5-11.5-42	454
ZrF_4 Salts	$NaF-ZrF_4$	59.5-40.5	500
	$LiF-NaF-ZrF_4$	42-29-29	460
	$LiF-NaF-ZrF_4$	26-37-37	436
	$NaF-RbF-ZrF_4$	33-24-42	420
	$KF-ZrF_4$	58-42	390
BF_4 Salts	$KF-KBF_4$	25-75	460
	$RbF-RbBF_4$	31-69	442
	$NaF-NaBF_4$	8-92	384

3.1.2 Vapor Pressure and Vapor Species

Most fluoride salts exhibit very low vapor pressures. Only compounds with higher oxidation state cations (such as BF_3, UF_6, and MoF_6) exhibit high vapor pressures. A few of the elements useful for coolants (BeF_2, ZrF_4) exhibit appreciable vapor pressures ($>1 \times 10^{-3}$ atm) at 800ºC. Table 6 lists normal melting and boiling points of single-component salts and of a few key multicomponent mixtures [28].

As is evident in Table 6, mixtures of these pure components will always exhibit lower vapor pressures (higher boiling points) than the most volatile constituent. Therefore, these salts do not exert significant partial vapor pressures (>1 atm) except at very extreme temperatures. The MSRE operated with a helium cover pressure of 0.35 atm, and the MSBR was designed for a cover pressure of 2.75 atm.

Table 6. Melting and boiling points of select salt compounds

Salt constituent(s)	Melting point (ºC)	Boiling point (ºC)
^{7}LiF	845	1681
NaF	995	1704
KF	856	1502
RbF	775	1408
BeF_2	555	1327 [a]
ZrF_4	903	600 (sublimes)
LiF-NaF-KF (46.5-11.5-42)	454	1570
LiF-BeF_2 (67-33)	458	~1400[a]
^{7}LiF-NaF-BeF_2 (31-31-38)	315	
NaF-BeF_2 (57-43)	340	~1400 [a]
NaF-ZrF_4 (59.5-40.5)	500	~1350 [a]
RbF-ZrF_4 (58-42)	410	~1450 [a]
KF-ZrF_4 (58-42)	390	~1450 [a]
KF-KBF_4 (25-75)	460	1070

[a]Estimated by extrapolation of lower-temperature data (~1100°C)

However, other factors are important. Even in a low-pressure system, the magnitude and nature of vapor produced from the salt needs to be evaluated. Experience with the ARE and the MSRE shows that very low salt vapor pressures (<1 mmHg) simplify the off-gas system design and that certain vapor species can present problems.

Vapor pressure is the physical property that is most sensitive to salt composition. Studies have been conducted to understand the effect of composition on the vapor pressure and vapor species of the thermodynamically nonideal systems containing ZrF_4 and BeF_2 [29, 30]. The results of these studies are useful for understanding and selecting the optimum coolant salt composition and are briefly reviewed in the following paragraphs.

The effect of salt composition on vapor pressure can be explained with the Lewis acid-base theory [31]. The native volatility of compounds containing the "acidic" constituent (Zr^{4+}, Be^{2+}) can be suppressed by donation of fluoride anions from the "basic" alkali fluoride constituent. The product of this donation is a low-volatility coordination-complex that is an integral part of the liquid salt solution. Not all the alkali fluorides are equal in their ability to donate fluoride anions for coordination compounds. The affinity of alkali cations for their own fluoride anion decreases with increasing atomic number; thus, the heavier alkali elements will more readily donate their fluoride anions. Therefore, heavier alkali fluorides are more effective in reducing the native volatility of the compounds containing the acidic species (Zr^{4+}, Be^{2+}).

The effect of salt composition on vapor pressure is readily apparent in the BeF_2 and ZrF_4 systems. Fig. 19 andFig. 20 display the suppression of volatility as the ratio of alkali fluoride content increases so that it satisfies the coordination-bonding demands of the polyvalent cation. These figures also show the heavier alkali fluorides are more effective in suppressing the native volatility of the compound containing the polyvalent element (e.g., beryllium or zirconium).

The decrease of vapor pressure due to coordination bonding is also accompanied by a change in vapor composition. For a system rich in alkali fluoride, the vapor consists primarily of the alkali fluoride. For salt compositions that exist at the optimum ratio that just satisfies the coordination demands of the system, the vapor species is an association complex of the alkali fluoride and the polyvalent cation. For systems deficient in alkali fluoride, the volatile species is the parent compound containing the polyvalent cation. These trends are also indicated in Fig. 19 and Fig. 20.

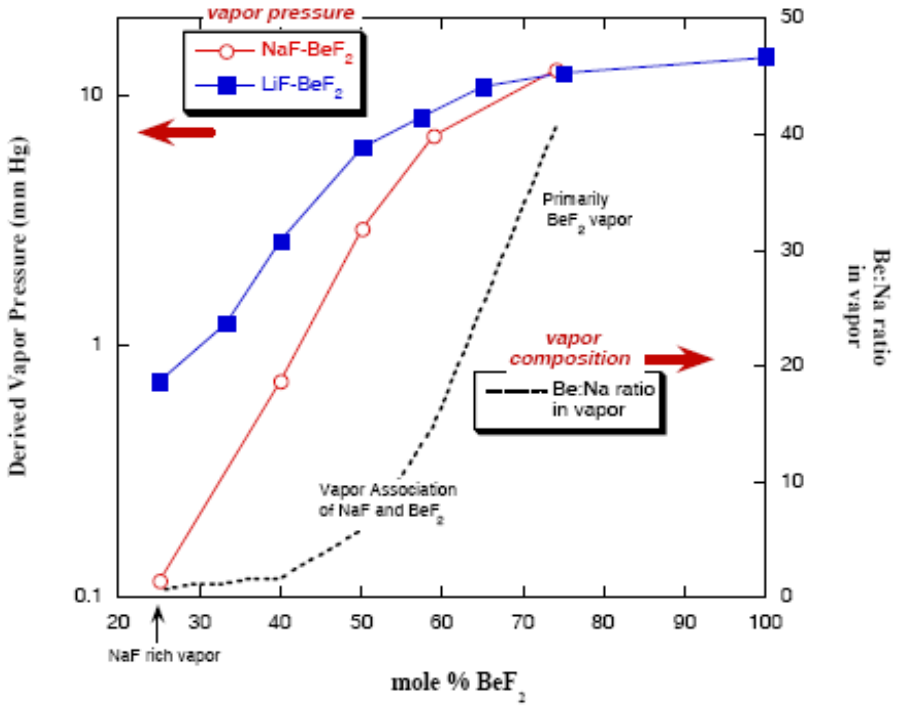

Fig. 19. Vapor pressure trends in alkali fluoride–BeF_2 systems at 900°C.

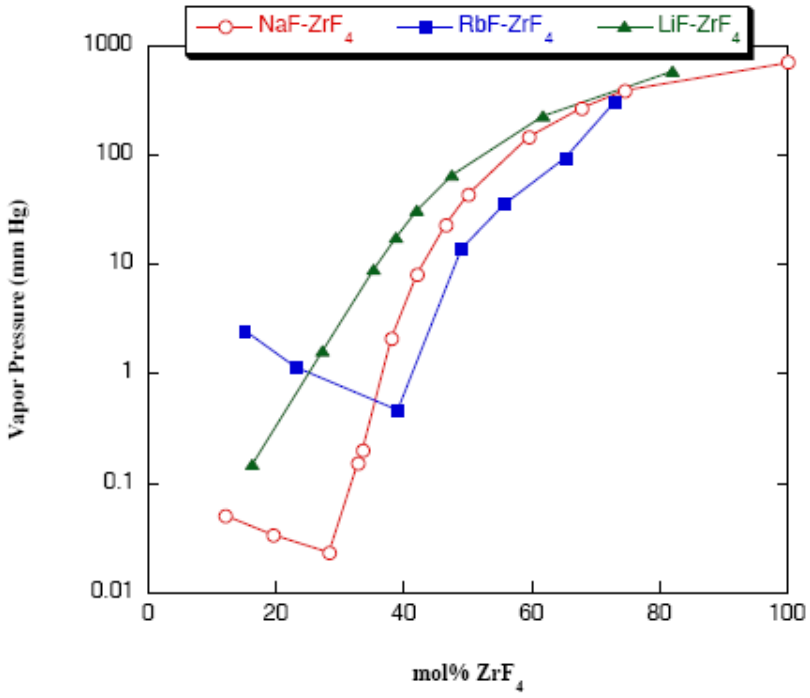

Fig. 20. Vapor pressure trends in alkali fluoride ZrF_4 systems at 900ºC.

From a practical standpoint, we should favor salt compositions with very low vapor pressures (<1 mmHg at 900 ºC) that generate vapor species that readily melt after condensing. This corresponds to salt compositions with a ZrF_4 mole fraction in the range of ~20–45%, and with a mole fraction of BeF_2 less than ~35–45%, depending on the alkali cations present and the temperature under consideration.

3.1.3 Density

Fluid density is important for the purpose of gauging the heat transport capability of a coolant in both forced convection and (especially) natural convection. Density is among the most straightforward of properties to measure and is one of the most readily estimated for new compositions. Liquid salt density decreases linearly with increasing temperature. As expected, low atomic number salts tend to be light (sp.g. ~2) and high atomic number salts tend to be heavy (sp.g. >4). Table 7 gives a list of selected fluoride salts with the density equation.

Table 7. Salt density equations for selected salts

Salt constituents	Molar composition (%)	Density equation [a] (kg/m^3)
LiF-NaF-KF	46.5-11.5-42	$2530 - 0.730 \times T$
$NaF-ZrF_4$	57-43	$3650 - 0.880 \times T$
$KF-ZrF_4$	58-42	$3416 - 0.887 \times T$
$LiF-NaF-ZrF_4$	26-37-37	$3533 - 0.517 \times T$
$NaF-NaBF_4$	8-92	$2252 - 0.711 \times T$
$KF-KBF_4$	25-75	$2258 - 0.803 \times T$
$RbF-RbBF_4$	31-69	$2946 - 1.047 \times T$

[a] T = temperature in degrees Celsius.

A simple and accurate method was discovered for predicting salt density based on additive molar volumes [32]. The following relationship allows prediction of molar volume and density for salt mixtures:

$$\rho_{mix}(T) = \frac{\sum_i x_i M_i}{\sum_i x_i V_i(T)} \ , \tag{3.1}$$

where x_i is the mole fraction of component i, M_i is the formula weight of component i, and $V_i(T)$ is the molar volume of component i at temperature T. Table 8 gives a list of single-compound molar volumes that allow estimation of mixture densities to an accuracy better than 5%.

Table 8. Standard molar volumes for use in estimation of mixture density

Component fluoride	Formula weight (g/mole)	Molar volume (cm^3/mole)	
		600ºC	800ºC
^{7}LiF	26.0	13.46	14.19
NaF	42.0	19.08	20.20
KF	58.1	28.1	30.0
RbF	104.5	33.9	36.1
CsF	151.9	40.2	43.1
BeF_2	47.0	23.6	24.4
MgF_2	62.3	22.4	23.3
CaF_2	78.1	27.5	28.3
AlF_3	86.7	26.9	30.7
ZrF_4	167.2	47.0	50.0

3.1.4 Viscosity

The viscosity, μ, of any fluid is defined by the equation

$$p_{xy} = \mu \frac{d\upsilon_y}{dx} \ , \tag{3.2}$$

where the stress p_{xy} is the force in the y direction exerted by fluid on a surface unit area, which is normal to the x direction, and υ_y is the velocity of the fluid in the y direction. Viscosities of liquids are measured in Pa·s in the SI system. The viscosities of liquid salts fall within the range of 0.5 to 5 mPa·s, which is similar to the viscosity of water (≈ 1 mPa·s) [33].

Liquid salts exhibit normal fluid behavior. They are Newtonian fluids and exhibit the typical exponential decrease in viscosity, μ, with reciprocal temperature:

$$\mu = A \exp\left(-\frac{B}{T}\right) \ . \tag{3.3}$$

Viscosity varies more with temperature than with any other fluid property. There are no truly predictive models for liquid salt viscosity; therefore, viscosity has been measured for many systems by complementary methods. Even though there is a significant database, there are a number of important mixtures for which no information exists; therefore, it is necessary to examine the variation of viscosity with composition and to identify trends and bounds.

The information for binary mixtures is fairly complete and is displayed in Fig. 21 [28]. All of the three families of low-melting salts have mixtures that exhibit reasonably low viscosities (<10 mPa·s) that make their use as industrial coolants possible. In contrast to other properties, compositional changes can have significant effects on fluid viscosity. These changes are evident in the variation of viscosity for different compositions within a binary or ternary system.

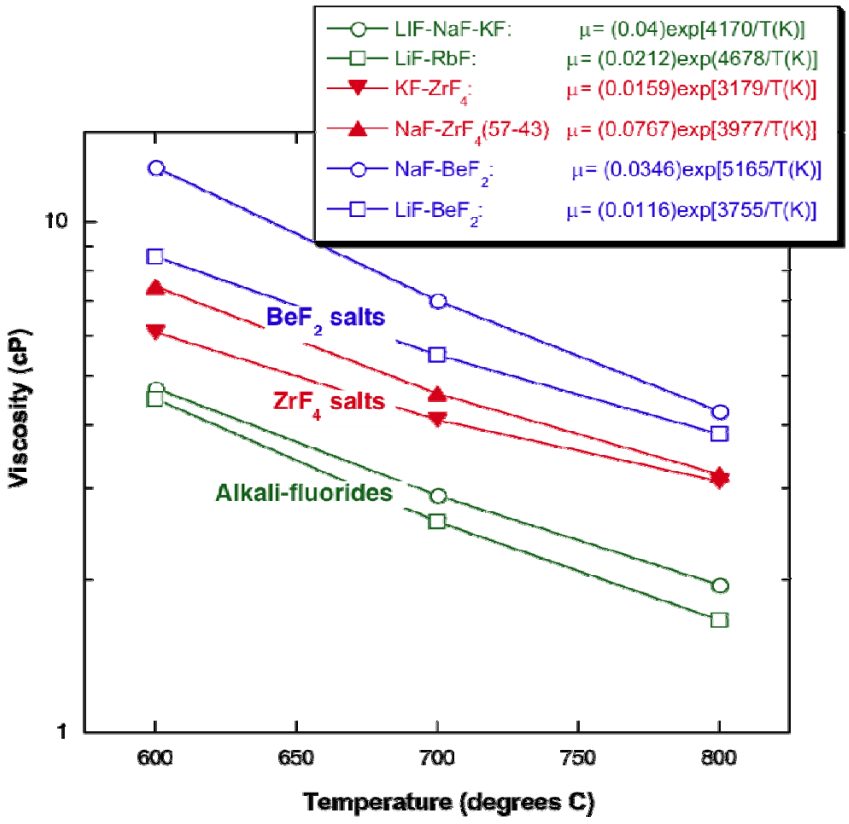

Fig. 21. Range of viscosities for various salt systems.

Viscosity, like vapor pressure and melting point, is strongly influenced by associative phenomena in the fluid phase. The influence of salt composition is most dramatic in the BeF_2 systems. The Be^{2+} cation has a special tendency to self-associate in fluoride melts that do not possess the requisite number of fluoride anions (1:4 Be:F) to satisfy the coordination demand of Be^{2+}. The association of Be^{2+} cations leads to an extended network that acts to increase the viscosity of the liquid salt. The thickening of the melt as the BeF_2 content increases (and the Be:F ratio in the entire melt decreases) is shown in Fig. 22 for $LiF\text{-}BeF_2$ [34] and in Fig. 23 for $NaF\text{-}BeF_2$ [35]. This thickening restricts the useful range of composition to less than 45% BeF_2.

Fig. 23 also reveals that the identity of the alkali cation in these systems has an effect. The more basic rubidium and sodium cations more readily donate the fluoride anion to Be^{2+} than does the lithium cation, resulting in a decreased amount of Be^{2+} self-association. Substitution of sodium for lithium, and rubidium for sodium or lithium, will lower the viscosity in these BeF_2 systems. The effect of potassium is expected to be intermediate between that of sodium and rubidium. Highly viscous pure BeF_2 was investigated to see whether it displayed non-Newtonian behavior. No deviation from Newtonian behavior was found [36].

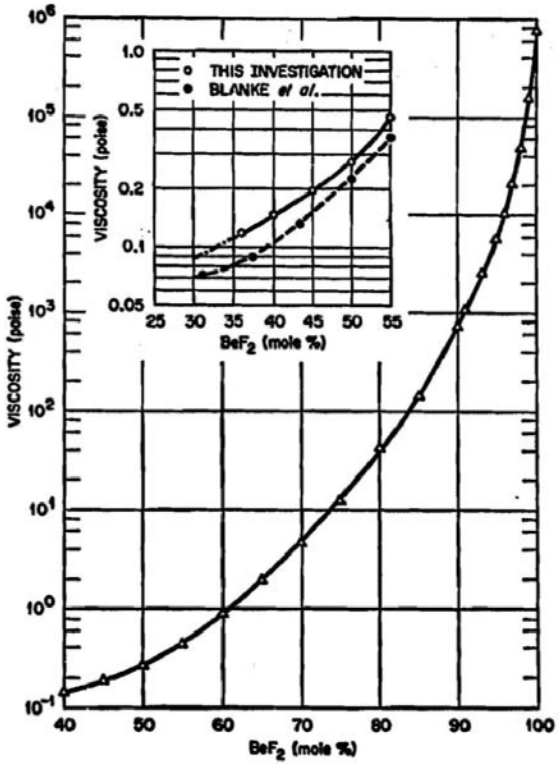

Fig. 22. Effect of BeF_2 composition on the viscosity of LiF-BeF_2 mixtures at 600°C.

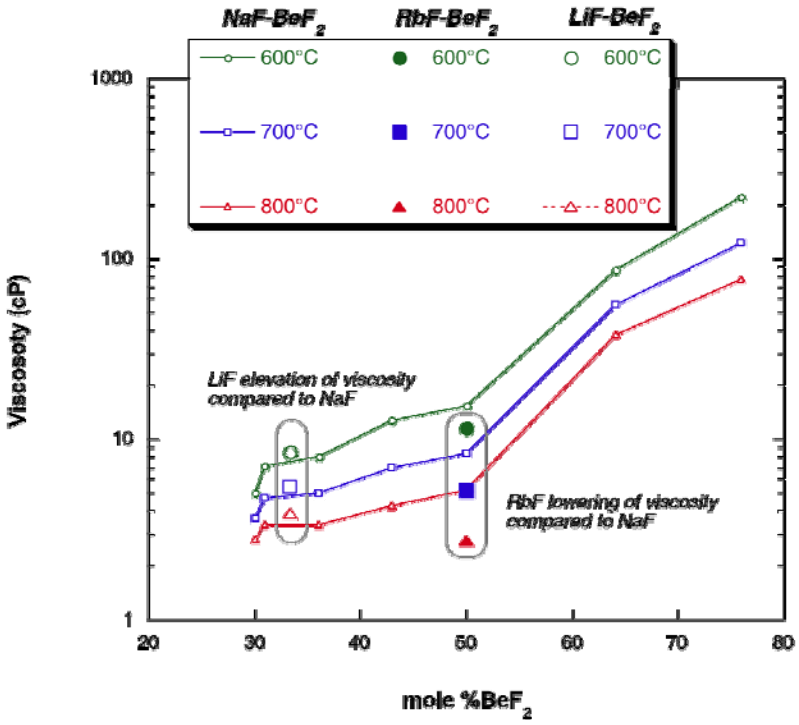

Fig. 23. Effect of alkali composition on the viscosity in BeF_2 salts.

It is more difficult to assess ZrF_4 salts in the same manner as BeF_2 salts [35]. The ZrF_4 phase diagrams have narrow low-melting regions; therefore, it is not possible to investigate large composition changes without also changing the alkali cation identity. Fig. 24 displays the broadest low-melting phase field of NaF-ZrF_4 with a solid line. Within this range of ZrF_4 content (42 to 52%), the change in viscosity is not large, but it does increase slightly with increasing ZrF_4 content. The effect of adding or replacing the alkali cation is the same in the BeF_2 system: lighter alkalis increase the viscosity, and heavier alkalis reduce the viscosity.

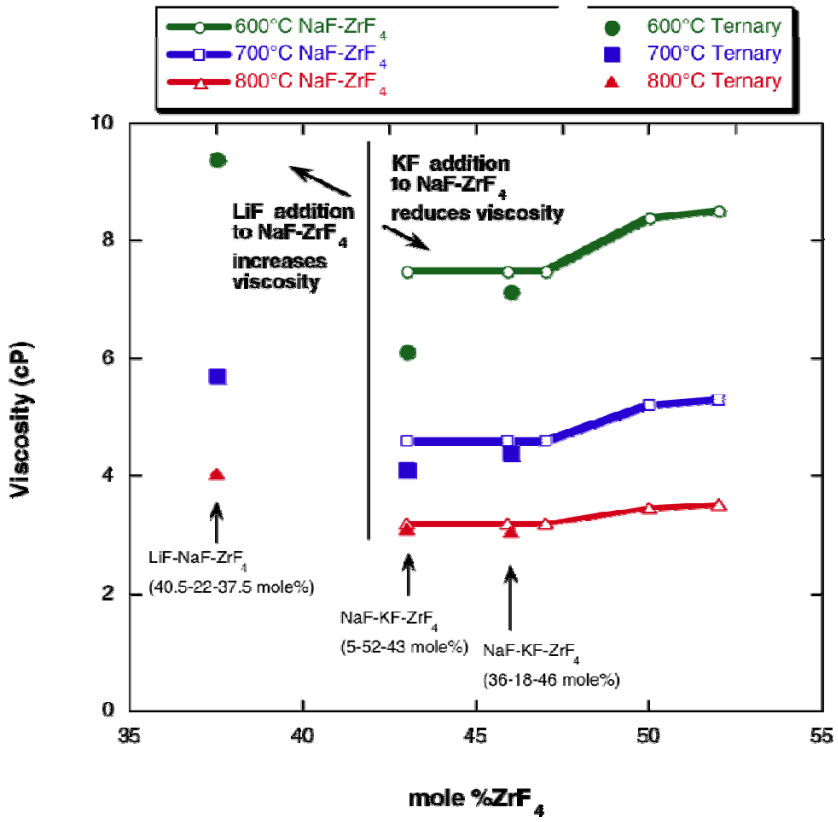

Fig. 24. Composition effects on viscosity in ZrF_4 mixtures.

The variation in viscosity of various alkali fluoride mixtures is not large (Fig. 21) and follows the same basic trend found for the BeF_2 and ZrF_4 systems. Heavier alkali mixtures are less viscous than lighter alkali systems.

It should also be noted that the three families of salts represent three distinct classes of liquid behavior. The alkali fluorides are ideal mixtures of very similar chemical constituents with very little associative behavior, whereas both ZrF_4 and BeF_2 mixtures are potential glass formers [37]. BeF_2-rich mixtures are "strong" glass formers characterized by extended association of cations into networks of large extent, thus giving rise to high viscosity "glassy" mixtures. BeF_2 is the fluoride analog to the SiO_2 glasses. Mixtures of ZrF_4 and alkali halides represent a different class of "fragile" glass mixtures that form due to a particular type of mixture thermodynamics that inhibits crystallization and preserves an amorphous structure during the liquid/solid phase transition. The ZBLA (ZrF_4-BaF_2-LaF_3) and ZBLAN (ZrF_4-BaF_2-LaF_3-NaF) glasses used for infrared optics are examples of this type of fragile glass [38].

These types of fragile glasses are different from network glasses in that the glass-forming compositions are relatively low-viscosity fluids rather than high-viscosity fluids [35].

The accuracy of previous viscosity determinations can be assessed by comparing the early ORNL measurements conducted during the 1950s and 1960s and the few recent investigations [39, 40]. These comparisons can be made for systems of alkali fluorides and ZrF_4-mixtures and are shown in Fig. 25 and Fig. 26. The deviation between the older and newer measurements is about 10%, with the older measurements predicting higher values. The older ORNL values are based on agreement of measurements obtained from capillary efflux and rotational viscometers. The newer measurements were obtained from a novel oscillating cup viscometer customized for high temperatures and sensitive to low-viscosity fluids. This agreement between newer and older values is within the error band reported for the older measurements (±20%). For more sophisticated viscosity correlations and extrapolation to higher temperatures, the methods recommended by Veliyulin can be used [41].

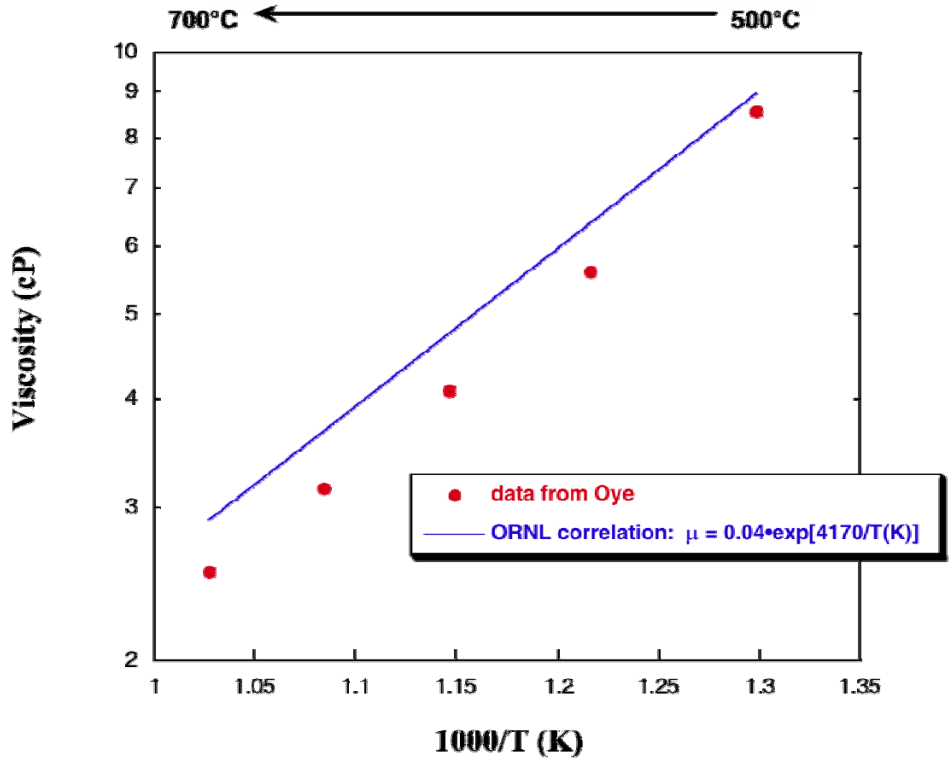

Fig. 25. Comparison of values measured for the viscosity of LiF-NaF-KF eutectic.

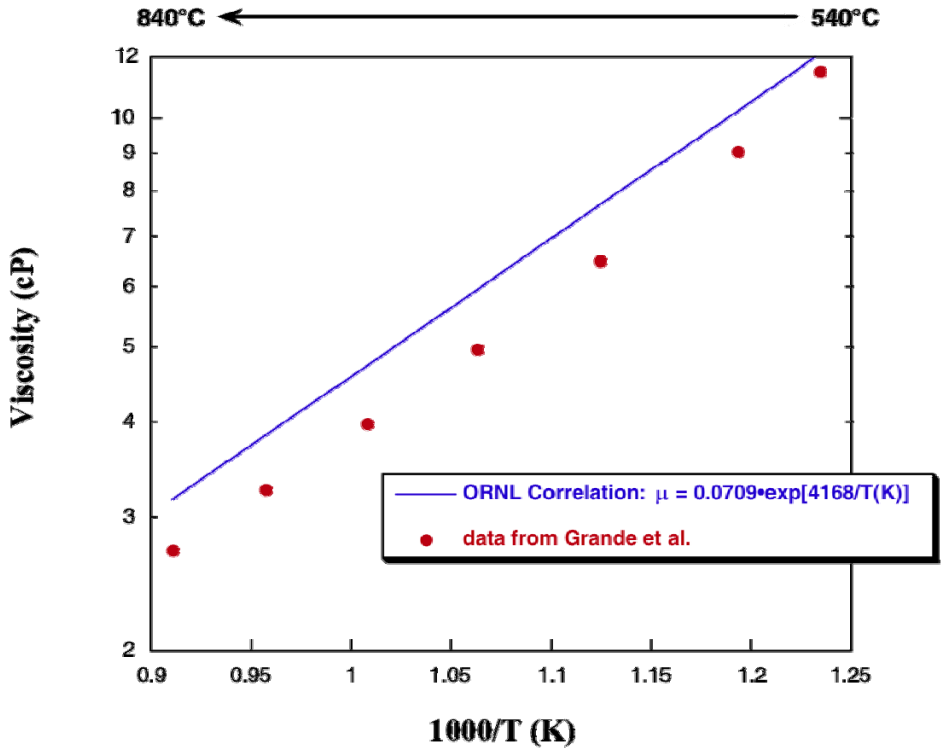

Fig. 26. Comparison of values measured for the viscosity of NaF-ZrF_4, 50-50 mol %.

3.1.5 Thermal Conductivity

Modern theories generally assume that the thermal conductivities of liquid salts are predominantly due to two mechanisms: the vibration mechanism arising from short-range order of the molecules in the liquid state and the translational or diffusion mechanism due to the motion of the ions. It was originally postulated that ionic diffusion—or the electrical conduction mechanism—made a substantial contribution, but the high ratio of thermal diffusivity to mass diffusivity, and the high value of the Lorenz number indicate a low contribution from diffusion. Turnbull showed this to be the case and found the ratio of diffusion conduction to total conduction to be less than 5%. Any theory which is to lead to useful results must therefore be based on the vibrational mechanism. It is for this reason that liquid salts have thermal conductivity values of a similar order to solid dielectrics [42].

The most successful model for predicting the thermal conductivity of liquid salts was proposed by Rao and refined by Turnbull [42]:

$$k = 0.119 \frac{T_m^{0.5} \rho_M^{0.667}}{(M/n)^{1.167}} \quad , \tag{3.4}$$

where k is the thermal conductivity in W/mK, T_m is the melting point in K, ρ_M is the molar volume of the liquid salt in cm^3/mole, M is the average formula weight of the salt, and n is the number of discrete ions per salt formula (i.e., $n = 2$ for simple salts like NaCl).

This model was originally proposed for simple, one-component salts, such as NaCl; but has been extended to mixtures with polyvalent cations. Mixtures of salt components are expected to exhibit a thermal conductivity slightly below the mole-fraction weighted average of the single components due to disruption of the vibrational modes of the quasi-crystalline lattice. The application of this model to salts with polyvalent cations requires an assignment of the ion number, *n*, based upon some assumption for speciation. Both of these factors introduce some uncertainty in the predictions for more complex salt systems.

The thermal conductivity of liquid salt is the most difficult property to measure, and it has led to the greatest amount of confusion and error in heat transfer calculations. This state of affairs is reflected in the general scientific literature on salt conductivity [42–44] and in the work focused on liquid salt reactors [45–47]. In early studies at ORNL using a variable-gap apparatus, conductivities were reported that were four times higher than the value now believed to be correct [35]. An improved variable-gap apparatus was designed to minimize the errors due to convection and bypassing heat flow [46]. A far lower thermal conductivity was measured with the improved apparatus, and these results were more similar to the values found for other salt systems using hot-wire and annular cylinder techniques [47].

These errors in the measurement of thermal conductivity led to a number of erroneous conclusions [48]. All of the systematic errors in measurement led to higher apparent values for thermal conductivity. When heat-transfer studies were conducted using the "high" value for thermal conductivity, it was found that the heat flow was lower than expected based on universal correlations for convective heat transfer. Because of the unexpected "low" heat flux, it was postulated that a significant film resistance must exist, and it was assumed that some type of insulating film impeded heat flow between the salt and the metal. A film coefficient was assumed in order to correct for this apparent discrepancy—but the discrepancy actually resulted from an error in calculating the thermal conductivity of the salt. Numerous corrosion studies on alloys exposed to salt for many years show that there is no such film on the surface of metals and that there is no heat transfer impediment due to insulating films. Fluoride salts are excellent fluxes for both oxides and fluorides and quickly dissolve corrosion products. Metallic corrosion products are dissolved in the salt solution. It was also found that "the overall heat transfer coefficient of the MSRE heat exchanger did not change during 22,000 h of salt circulation and 13,000 equivalent full-power hours of operation, thus indicating no buildup of scale and no evidence of gas filming" [49]. Detailed forced-convection heat-transfer measurements confirmed this same behavior in out-of-pile tests with the MSBR fuel salt composition [50].

Ignatiev [51] and Khoklov [54] recommend an empirical equation that is simply a function of temperature (T) and salt formula weight (M) for correlating thermal conductivity:

$$k = 5 \times 10^{-4} T + \frac{32.0}{M} - 0.34 \ . \tag{3.5}$$

The database for the Russian correlation includes a large number of alkali halides, BeF_2-salts, and salts containing UF_4 and ThF_4. Table 9 presents the measured thermal conductivity values for halide salts that are expected to be the most reliable and the results of both predictive methods. The trend of decreasing thermal conductivity with increasing formula weight of the salt has been found in other measurements on pure halide salts and their mixtures [42, 52–54]. There is almost no reliable data on the thermal conductivity of ZrF_4-containing salts.

Table 9. Comparison of measured and predicted thermal conductivities of selected fluoride salts

Salt constituents	Molar composition (%)	Temperature (°C)	Measured conductivity (W/mK)	Rao-Turnbull prediction (W/mK)	Khoklov correlation (W/mK)
LiF-NaF-KF	46.5-11.5-42	500	0.60	0.68	0.82
		700	–	–	0.92
LiF-NaF-RbF	42-6-52	700	–	0.42	0.62
LiF-BeF_2	66.7-33.3	600	1.0	0.79	1.1
NaF-BeF_2	57.43	700	–	0.58	0.87
LiF-NaF-BeF_2	26-37-37	700	–	0.62	0.97
LiF-ZrF_4	51-49	700	–	0.35	0.48
NaF-ZrF_4	59.5-40.5	700	–	0.36	0.49
KF-ZrF_4	58-42	700	–	0.32	0.45
RbF-ZrF_4	58-42	700	–	0.26	0.39
LiF-NaF-ZrF_4	26-37-37	700	–	0.36	0.53
NaF-AlF_3	75-25	1000	0.80	0.79	0.91

3.1.6 Heat Capacity

Fluoride salts have relatively large heat capacities. In fact, they rival water in their ability to carry heat. Heat capacities of selected single-component salts are listed in Table 10 [55].

The simplest rule for estimating high-temperature heat capacities in the condensed state is that of Dulong and Petit, which states that the specific heat capacity—regardless of the nature the substance of crystal—is equal to 3 *R/M*, where *R* = 8.314472 J/K mole is the gas constant, and *M* is the molar mass in kg/mole.

Based on Dulong-Petit, the heat capacities of liquid fluorides per kg-atom were approximately equal to 25 kJ/K. However, the experimental measurements for pure compounds at ORNL in the 1960s indicated that the heat capacity per kg-atom was approximately 33 kJ/K, and the data for fluoride mixtures would seem to indicate the average value to be somewhat higher than this value.

Table 10. Heat capacities of selected salts

Salt	Temperature (°C)	Measured heat capacity C_p (J/K)
LiF	848	64.85
NaF	995	68.62
KF	858	66.94

The temperature dependence of heat capacity in liquids is weak. Based on the Dulong-Petit law and the weak temperature dependence, specific heat capacity of mixtures can be estimated using the following equation

$$c_p = 33.47 \frac{\sum_{i=1}^{n} N_i p_i}{\sum_{i=1}^{n} N_i M_i} , \quad (3.6)$$

where c_p is the specific heat capacity in J/kg K, n is the number of salt components, p_i is the number of atoms in a molecule of component i, and N_i and M_i are the mole fraction and the molecular weight, respectively, of component i. A listing of predicted and experimentally measured specific heat capacities is given in Table 11 for a number of selected salts.

Table 11. Experimentally measured and estimated values of specific heat capacity for selected salt mixtures

Salt composition[a]	Measured heat capacity (J/kg K)	Dulong-Petit prediction (J/kg K)
LiF-NaF-KF	1882.8	1619.2
LiF-KF	1840.96	1594.10
LiF-NaF-RbF	–	987.42
LiF-RbF	1188.26	945.58
LiF-BeF_2	2414.17	2368.14
NaF-BeF_2	2175.68	1840.96
LiF-NaF-BeF_2	–	2045.98
LiF-ZrF_4	–	1221.73
LiF-NaF-ZrF_4	–	1238.46
NaF-ZrF_4	–	1150.60
KF-NaF-ZrF_4	1087.84	1054.37
KF-ZrF_4	–	1050.18
RbF-ZrF_4	–	836.80

[a]Molar compositions are identical to previously defined salt mixtures.

A recent study indicated a more accurate model for flinak specific heat capacity in J/kg K [56]

$$c_p = 976.13 + 1.063\, T , \quad (3.7)$$

where T is the fluid temperature in ºC. As indicated in Eq. 3.7, the temperature dependence is insignificant.

3.1.7 Component Separation and Snow

In any high-temperature salt system, a purged cover gas will be necessary. The transport of significant amounts of salt vapor in this cover gas system can cause problems. In the operation of the ARE, it was found that the vapor over the ARE salt (53%NaF-41% ZrF_4 -6%UF_4) was nearly pure ZrF_4. Because ZrF_4 sublimes rather than boils, ZrF_4 "snow" was found in the exhaust piping. The ZrF_4 was not returned to the salt reservoir by condensing as a liquid and draining back to the salt reservoir. Elaborate "snow traps" were designed, as shown in Fig. 27, to mitigate this problem [48], but it appears that a wise choice of salt composition can eliminate it completely.

The experience with the MSRE was quite different. The MSRE salts (65%LiF-29%BeF_2-5% ZrF_4-1% UF_4) exhibited very low vapor pressure, more than 100 times lower than the ARE salt. The vapor over the MSRE salt was also of a different character. This vapor contained both LiF and BeF_2 in a proportion that melted at a low temperature, such that the condensate would drain back to the reservoir as a liquid.

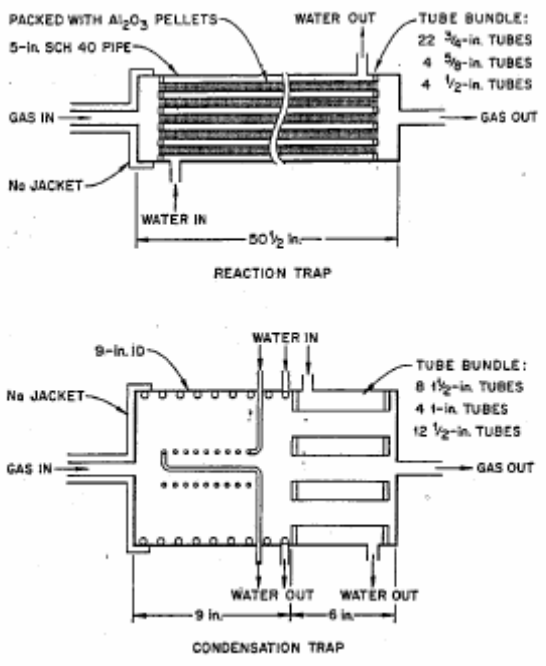

Fig. 27. ZrF_4 "snow-trap" designs developed for the Aircraft Reactor Test.

3.2 CORROSION CHEMISTRY

The underlying reaction for container corrosion by a liquid fluoride salt is the reduction–oxidation reaction of a fluorine atom with a container atom. Fluorine is the most electronegative element and reacts aggressively with almost all other elements. Pure fluoride salts are on average electrochemically neutral with each fluorine atom ionically bonded to electropositive atoms. However, the instantaneous (as opposed to the average) configuration of the atoms, molecules, and ions, comprising the liquid determines its chemical behavior. Even small electronegative impurity additions to the melt, transient bond disturbances, or random thermally induced liquid structural fluctuations result in fluorine atoms becoming chemically available [70].

While the fluorine atoms on average remain strongly coulombically bonded to the electropositive atoms comprising the salt molecule, in a liquid the association becomes more generalized with coordination between neighboring atoms and molecules. Moreover, the local configuration of the salt molecules continually shifts due to thermal fluctuations. Salts capable of accepting two electrons (Lewis acids) from fluorine ions reduce the free fluorine potential by forming complexes. An example of BeF_2 complexation with two fluorine atoms to form $BeF_4^=$ is shown in Fig. 28. The lack of a Lewis acid structure to capture free fluorine atoms results in pure alkali metal fluoride salts—e.g., LiF-NaF-KF (flinak) being more corrosive.

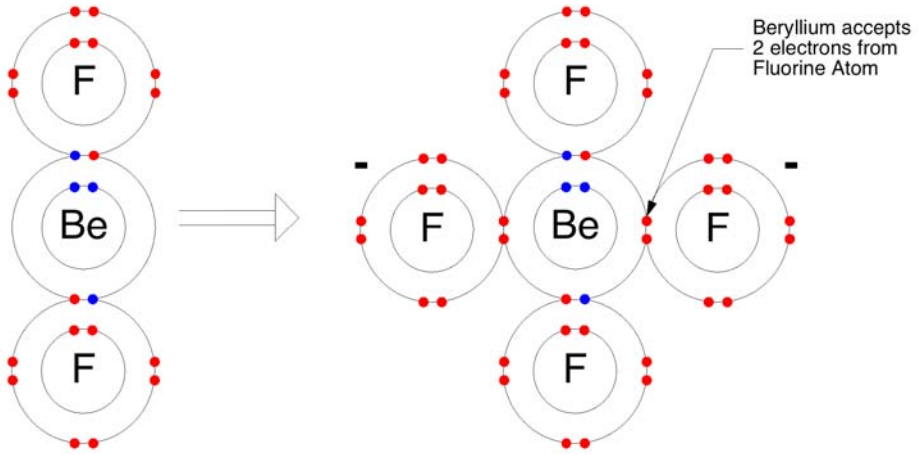

Fig. 28. Beryllium fluoride complexation.

The electrochemical corrosion potential of the liquid salt relative to the container wall is the sum of the chemical and electrical potential differences between the two. The electrochemical (or Galvani) potential difference between the container and melt results from differences in the work function (Fermi level difference) of electrons in the two materials. The Galvani potential difference is determined entirely by inherent chemical characteristics of the two materials. An electrical double layer is formed across the material interface consisting of two parallel layers of charge. The first layer is a surface charge on the container alloy. The other layer is in the salt, and electrically screens the first layer. This second layer is diffuse, because it forms from free ions in the fluid under the influence of electric attraction and thermal motion, and is thus called the diffuse layer.

In practical terms, the chemical potential of the system at a particular temperature is its Gibbs energy, *G*. The Gibbs energy is at a minimum when the system is in equilibrium and as such Gibbs energy differences provide a measure of the spontaneity of chemical reactions between the salt and container. In liquids and solids at constant pressure *P*, the Gibbs energy increases slowly with temperature, *T*, as the entropy *S* increases according to

$$\left[\left(\frac{\delta G}{\delta T}\right)_P = -S\right] . \tag{3.8}$$

Plots of the Gibbs energy of structural and salt fluorides are shown in Fig. 29 (data from HSC Chemistry software). The small slope increases in the Gibbs energy versus temperature relationship in KF at 759ºC and NaF at 883 ºC arise from the boiling points of potassium and sodium.

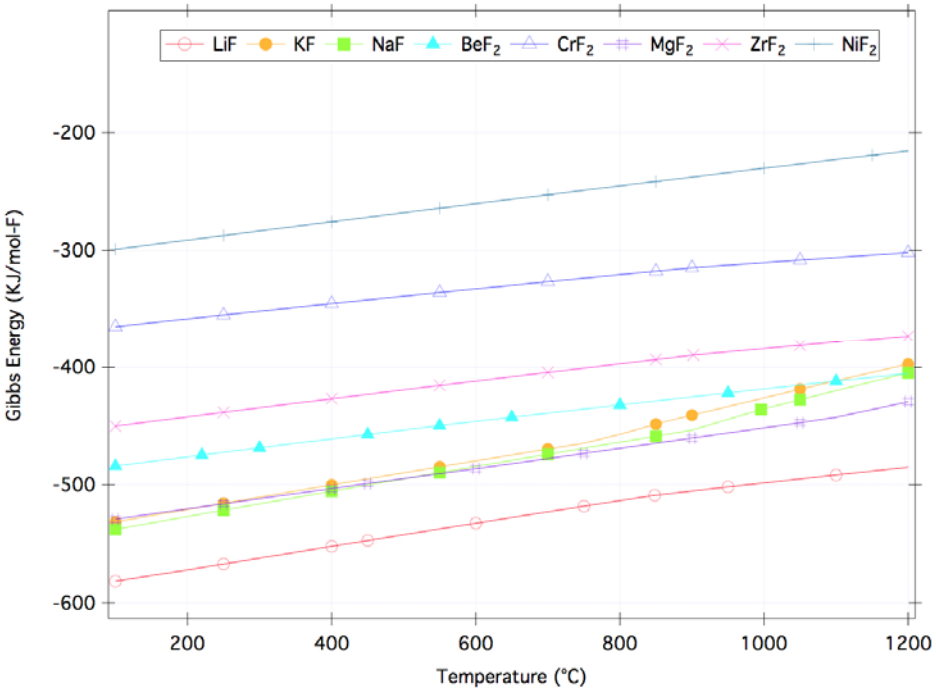

Fig. 29. Gibbs free energy of structural and salt fluorides.

The overall electrochemical stability of useful coolant fluoride salts relative to the alloy constituent elements (gap between CrF_2 and ZrF_2) shows that none of the salts are intrinsically corrosive to the container walls. However, fluoride salts are good solvents for metal oxides [71]; hence alloy surface passivation using an oxide layer is not possible, and corrosion depends directly on the thermodynamic driving force of the corrosion reactions. Design of a chemically stable system utilizing molten fluoride salts, therefore, requires the development of containers whose components are in near-thermodynamic equilibrium with the salt medium [72].

The corrosion that liquid fluoride salts have demonstrated in practice for metal alloys arises from the impact of impurities and transient phenomena within the melt. In particular, electronegative impurities within the salt increase its free fluorine potential and thus its corrosivity. Oxygen and halide (sulfur and chlorine) impurities are particularly problematic in terms of corrosion, and almost all commercial sources of supply for fluoride salts contain significant amounts of electronegative impurities. A discussion of salt purification techniques is included in Sect. 3.3.

Chromium fluoride has the least negative Gibbs energy of any of the likely structural material elements. As such fluoride salts will preferentially corrode the chromium from the container alloy [73, 74]. Chromium, however, remains and important element in many structural alloys due to the chromium oxide passivation layer that forms on its surface in air protecting the container on its exterior surface. The impact of chromium corrosion can be accentuated in some alloys at the grain boundaries where the chromium concentrates as carbide. In addition to removing material from the surface of the container changing the chromium concentration distribution within the alloy will result in high temperature solid-state diffusion of chromium within the structural material that can deleteriously impact the overall material structural properties [75]. The attack proceeds by the formation of subsurface voids that become progressively larger and deeper as the temperature and period of exposure increases. An optical micrograph of a grooved piece of Inconel 600 showing the subsurface void formation exposed to flinak for approximately sixty days at 700ºC is shown as Fig. 30.

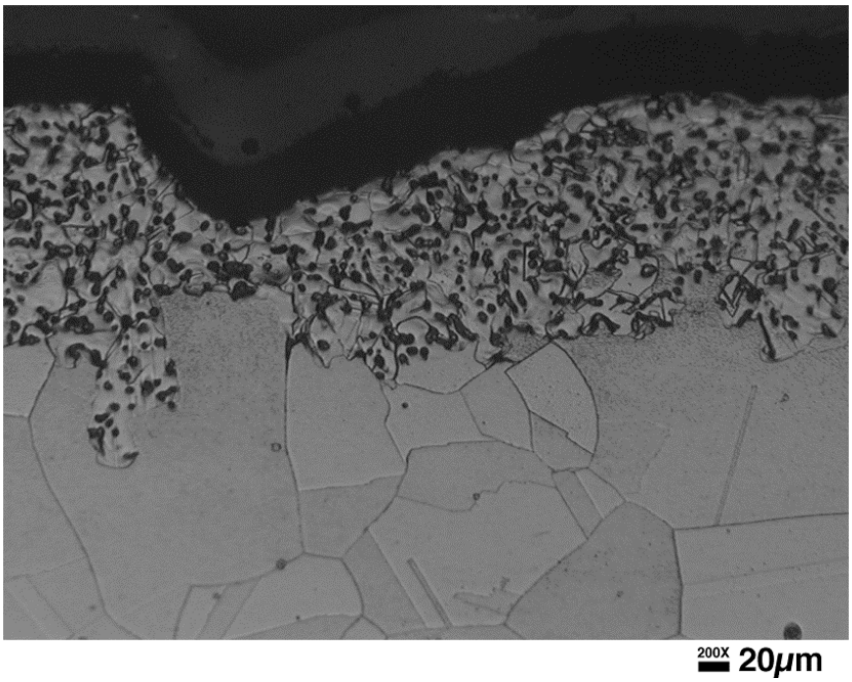

Fig. 30. Inconel 600 sample exposed to flinak at 700ºC for approximately 60 days.

The solubility of chromium within fluoride salts increases with temperature. If corrosion is not controlled, the chromium concentration within the salt will increase until it reaches the saturation limit. As the salt in the heat transfer loop circulates the salt will pick up additional chromium at the high-temperature portions of the loop and redeposit the chromium at lower temperature portions of the loop due to the solubility variation with temperature. The rate-limiting step in this process is the diffusion of the chromium within the alloy [76].

3.3 PREPARATION OF FLUORIDE SALT INVENTORY

Fluoride salts are not directly available at the purity level and volume necessary for heat transfer loop applications. Thus the first steps in liquid fluoride salt use are to purchase and purify the precursor chemicals that when melted together form the heat transfer salt. Purifying the component salts prior to melting is typically easier than subsequently purifying the melt. For example, as received potassium fluoride invariably includes adsorbed moisture. Adsorbed moisture can be removed by heating the salt to 105–150°C and holding in a dry atmosphere. In contrast, water that has been dissolved into a flinak melt requires sparging with hydrogen fluoride to remove.

As part of the MSR program, considerable effort was devoted to developing techniques for cleaning fluoride salts and much of the following discussion derives from the MSR era techniques [77]. The most important impurities in fluoride salts that must be removed to prevent severe corrosion are moisture and oxides. Oxides are removed from the salt by sparging with anhydrous hydrogen fluoride.

$$O^{2-} + 2HF \rightleftharpoons 2F^{-} + H_2O \quad . \tag{3.9}$$

During the MSR program, the sparging was continued beyond practical reaction completion to ensure an excess of "oxide capacity" remained in the salt to accommodate inadvertent contamination during operation. Sulfur and chlorine also need to be removed (<10 ppm) from the salt to minimize corrosion. Sulfur can be removed from the melt by first reducing the sulfate ion be reacting melt with an active metal such as magnesium.

$$SO_4^{2-} + 4Mg^0 \rightleftarrows 4MgO + S^{2-} \quad . \tag{3.10}$$

The sulfide ion is then removed by hydrogen fluoride sparging yielding H_2S in the exhaust gas stream. Sulfide and moisture measurement in the exhaust gases are thus the key process completion indicators. A significant portion of the expense of the MSR era salt cleaning was in the process control. Repeatedly extracting samples for off-line analysis was time-consuming and required custom sampling equipment.

Hydrogen fluoride was stripped from the exhaust gas by passing through a sodium fluoride bed. Insoluble impurities were removed using a combination of decanting and straining through a sintered nickel filter with a 38-micron pore diameter.

Hydrogen fluoride at elevated temperature is highly corrosive to the salt container structural alloy and halogen salts as received frequently include significant iron contamination. Nickel is the preferred element to as the structural material in a fluorine processing system since a tightly adherent film of NiF_2 (through which additional fluorine must diffuse in order to cause further corrosion of the nickel) forms on its surface. The rate of attack is greatly reduced, although not to zero, once the protective film of NiF_2 is formed on the exposed nickel surface [78].

Structural metal impurities can be removed from the salt by through electroplating. Once the metal oxides impurities have been reduced by sparging with hydrogen fluoride (or hydrogen) the resultant metal fluorides can be plated onto a cathode held at a voltage sufficiently negative to dissolve the metal fluorides but not attack the primary melt constituent fluorides (Fig. 29). The electroplating process is analogous to the Hall-Héroult process used to electrowin aluminum from a cryolite melt. Alternatively, the structural metals can be plated out of the fluoride melt by exposing the melt to a free surface of metal with a more negative Gibbs energy for fluoride formation than the structural metal fluoride such as zirconium or beryllium (as shown in Fig. 38).

The continuous fluorinator design developed at ORNL employed a frozen wall technique to minimize the structural alloy corrosion by the hydrogen fluoride [79]. The combination of a cooled nonelectrically conductive wall and induction heating of the salt enabled developing a protective frozen layer of salt against the container wall.

4. LIQUID-FLUORIDE-SALT HEAT TRANSFER CHARACTERISTICS

The heat transfer characteristics of liquid salts have been a topic of discussion since their first use as heat transfer media. These materials are generally characterized by low vapor pressures—allowing near atmospheric operation, high melting points and good thermal properties. Thermal conductivities of liquid salts are somewhere between those of water and the poorer liquid metals, and the heat capacities per unit volume are as good as that of water. Studies of the heat and momentum transfer characteristics indicate that these the liquid salts compete favorably with the liquid metals [57].

In the early 1950s, an experimental program was initiated at ORNL to obtain heat transfer coefficients for liquid fused salts, primarily because of the lack of comprehensive data [58, 59]. The first fused salt studied were sodium hydroxide; the eutectic mixture of sodium, potassium and lithium fluoride (11.5-42.0-46.5 mole %); the mixture of $NaNO_2$-$NaNO_3$-KNO_3 (40-7-53 wt %), which is commercially known as HTS; and the mixture of NaF-ZrF_4-UF_4 (50-46-4 mole %). Grele and Gedeon also performed experimental measurements on flinak at NASA [60].

Earlier tests performed with flinak flowing in an Inconel test tube yielded lower overall heat transfer. This observation lead the investigators to believe that liquid salts either do not wet the surface of the container indicating the formation of a gas film at the metal surface, or they cause buildup of a thin deposit on the metal surface, both of which would result in increased thermal resistance. It was calculated during one experiment with flinak flowing in Inconel, the heat transfer was as much as a factor of 2 lower than the heat transfer for sodium hydroxide or other ordinary fluids. The mismatch was also attributed to a possible error in physical properties used, particularly either thermal conductivity or viscosity. Post-experiment investigations of the Inconel test section confirmed that a green deposit was formed on the inside tube surface. Petrographic and electron diffraction examinations of the film showed that the major constituent of the deposit is K_3CrF_6. Some Li_3CrF_6 and small amounts of oxides of chromium and nickel were also present. The thickness of the film was determined to be approximately 0.01 mm. Follow-up experiments with nickel and stainless steel test sections performed at the same experimental setup did not show any indication of deposit buildup, and gave heat transfer measurements as expected. The measurement results confirmed that flinak, in the absence of the interfacial film, behaves as an ordinary fluid with respect to heat transfer [61].

4.1 A REVIEW OF LIQUID SALT HEAT TRANSFER MEASUREMENTS

The first reported measurements for fused salt heat transfer were from Kirst et al. for the HTS [62]. Although the data had some scatter when plotted in terms of Colburn *j*-factor—as will be defined later in the report—against Reynolds number, the results suggested that fused salts behaved as ordinary fluids from the standpoint of heat transfer.

Measurements by Grele et al.

Grele's measurements used flinak flowing through an electrically heated horizontal test section [60]. The range of variable included Reynolds numbers from 2000 to 20,000 corresponding to bulk fluid velocities from 1.25 m/s to 4.5 m/s, average bulk fluid temperatures from 540°C to 730°C, average surface temperature from 570°C to 793°C, and heat flux up to about 1.26 MW/m^2. The test section was fabricated from Inconel X tubing having an outside diameter of 9.525 mm and a wall thickness of 1.65 mm. Outside tube wall temperatures were measured with 14 chromel-alumel thermocouples spotted at intervals along the test section. The physical property data used in Grele's calculations for flinak was obtained from Reference [63].

The experimental data is shown in Fig. 31. The straight line shown in the plot is the Dittus-Boelter correlation. The measured data is approximately off by the Dittus-Boelter correlation by 60%.

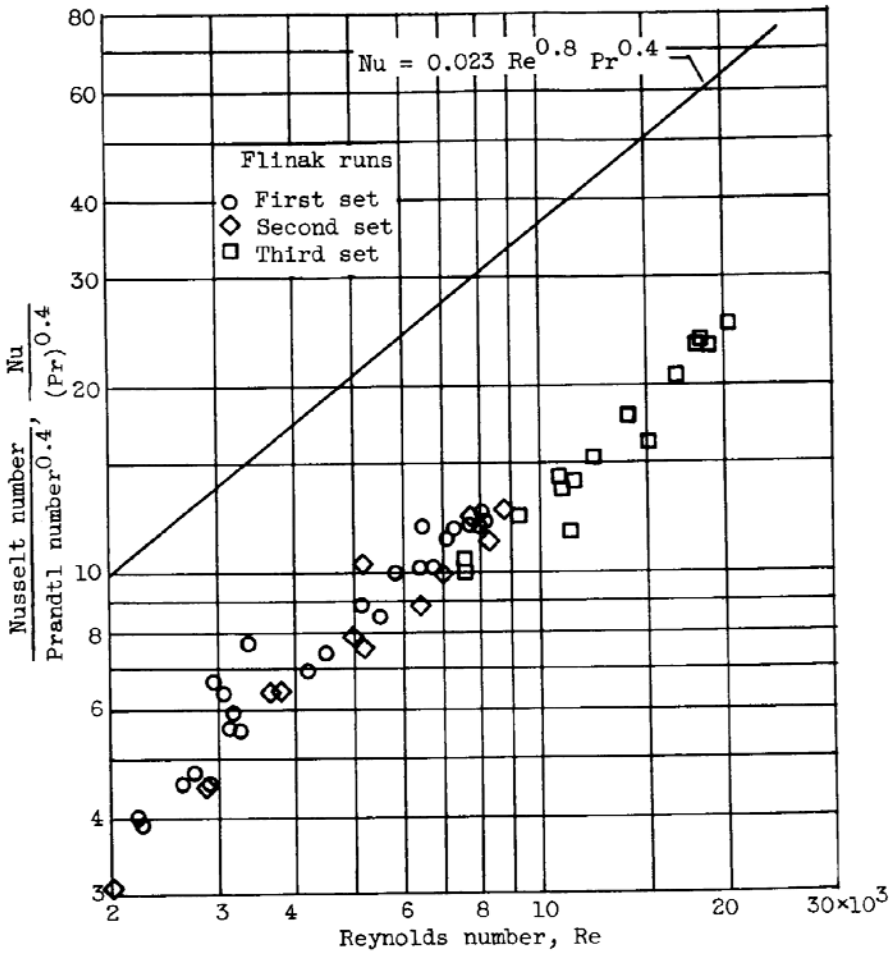

Fig. 31. Flinak heat transfer data [60].

Analysis of the data suggested that the discrepancy was a result of either errors in heat transfer coefficients, or the formation of a high-resistance layer. It was concluded that even a large deviation in thermophysical data alone could not cause such a dramatic mismatch between the theory and experimental results. Fig. 32 shows the correlation of experimental results obtained with the test setup to the theoretical Colburn *j-function*.

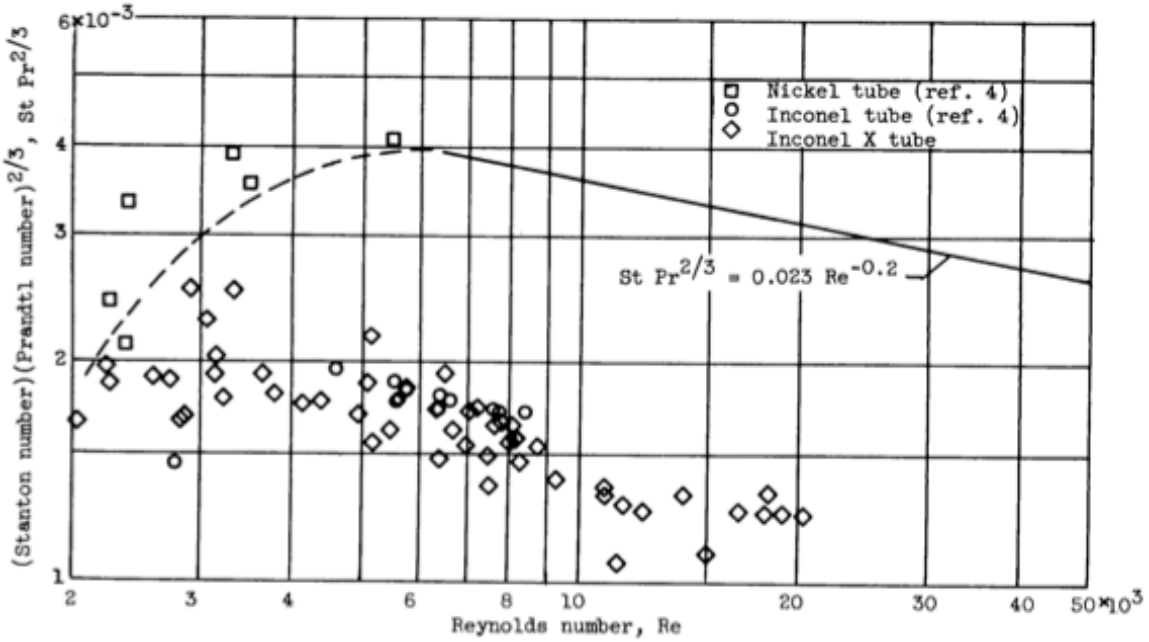

Fig. 32. Comparison of flinak heat transfer data [60].

It was observed during the post-experiment investigations that a scale was indeed formed on the inside surface of the test section. Micrographic analyses indicated severe intergranular penetration of flinak into the Inconel X matrix.

As a side note, the experimental system that Grele et al. used did not employ any corrosion control techniques.

Measurements by Hoffman et al. [61]

Later measurements by Hoffman et al. also used NaF-KF-LiF eutectic flowing in forced convection through circular tubes. The range of variables included Reynolds numbers between 2300 and 9500, Prandtl numbers between 1.6 and 4.0, average bulk fluid temperature between 527ºC and 743ºC, and heat flux between 28.4 kW/m^2 and 605.7 kW/m^2.

The test section included 61-cm long tubes of nickel, Inconel and Type 316 stainless steel. Each tube was long enough ($x / D > 100$) to allow fully developed flow. The outside surface temperature profile of the test section was monitored by 24 equally spaced thermocouples.

It was found that forced convection heat transfer of flinak can be represented by general heat transfer correlations for ordinary fluids ($0.5 < \mathrm{Pr} < 100$). The Colburn *j-function* was used as the correlating parameter with the measured data. The Colburn j-function is expressed by

$$j = \mathrm{St}\ \mathrm{Pr}^{2/3} = 0.023\ \mathrm{Re}^{-0.2}\ , \tag{4.1}$$

where St is the Stanton modulus defined as

$$\mathrm{St} = \frac{h}{c_p G} \ . \tag{4.2}$$

The experimental data in correlation with the Colburn *j*-function is shown in Fig. 33. The heat transfer coefficient in each measurement was calculated for a position far downstream ($x / D > 100$) where fully developed turbulent conditions existed. The data demonstrated that variations in the entrance conditions, arising from slight differences in geometry between the two ends of the test section, strongly affect transition region heat transfer. This is illustrated in Fig. 33 by normal and inverted open triangles, which indicate flow in opposite directions.

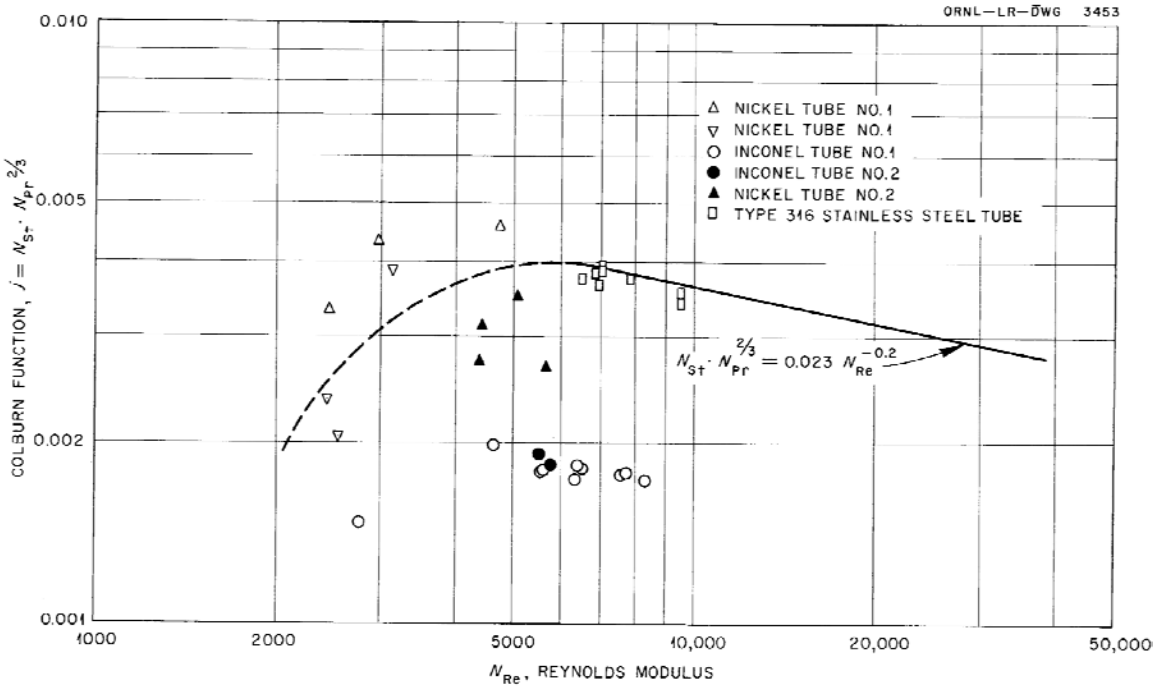

Fig. 33. Experimental data by Hoffman et al. [61] for flinak heat transfer.

Measurements with the Inconel test section demonstrated a significant deterioration in heat transfer. Three possibilities were considered: (1) the experimental measurements were in error, (2) the physical property data used in the analysis were incorrect, or (3) "non-wetting" occurs or an interfacial resistance (film) existed at the metal surface. Heat balance eliminated the possibility of error in measurements. The erroneous physical property data alone was not found sufficient to explain the deviation from the expected values; at least such drastic deviation was only the case for Inconel. Evidence suggested that flinak readily wets Inconel surfaces, eliminating the "non-wetting" condition. The only reasonable explanation was the possibility of the formation of an interfacial resistance layer between flinak and the inside surface of Inconel. Post-experiment investigations of the Inconel test section confirmed that a thin layer was formed on the inside surface of the Inconel test section. Petrographic and electron diffraction examination of the film showed that major constituent was K_3CrF_6, and some Li_3CrF_6 was also found. The thickness of the film was measured to be approximately 0.1 mm.

Nickel and 316 stainless steel tubes did not show any film formation.

The experimental data was also used to obtain information on hydrodynamic behavior. The entrance system consisted of a thermal entrance region length preceded by a hydrodynamic entrance length of 8 to 13 tube diameters. The $(x/D)_e$ was taken as the position at which the local heat transfer coefficient had decreased to within 10% of its fully developed value. The variation of local heat transfer coefficient as a function of x/D for a typical experimental run can be seen in Fig. 34.

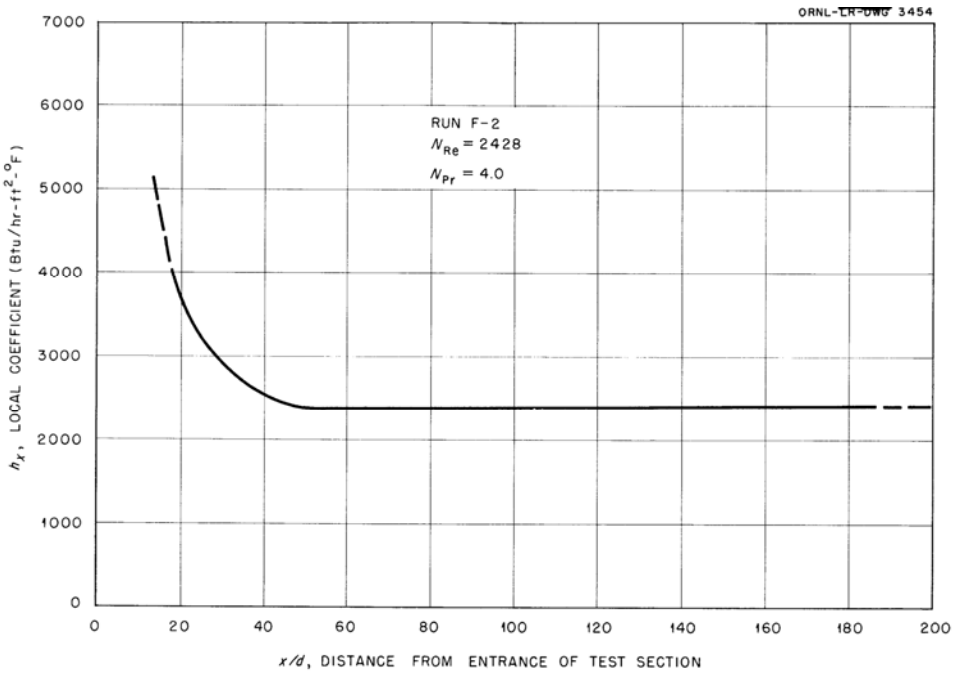

Fig. 34. Local heat transfer coefficient for flinak flowing in a pipe under uniform heat flux conditions.

The observed dependence of $(x/D)_e$ on the Peclet number ($\mathrm{Pe} = \mathrm{Re}\,\mathrm{Pr}$) is shown in Fig. 35. This variation also suggests that fused salts behave as ordinary fluids from the heat transfer standpoint.

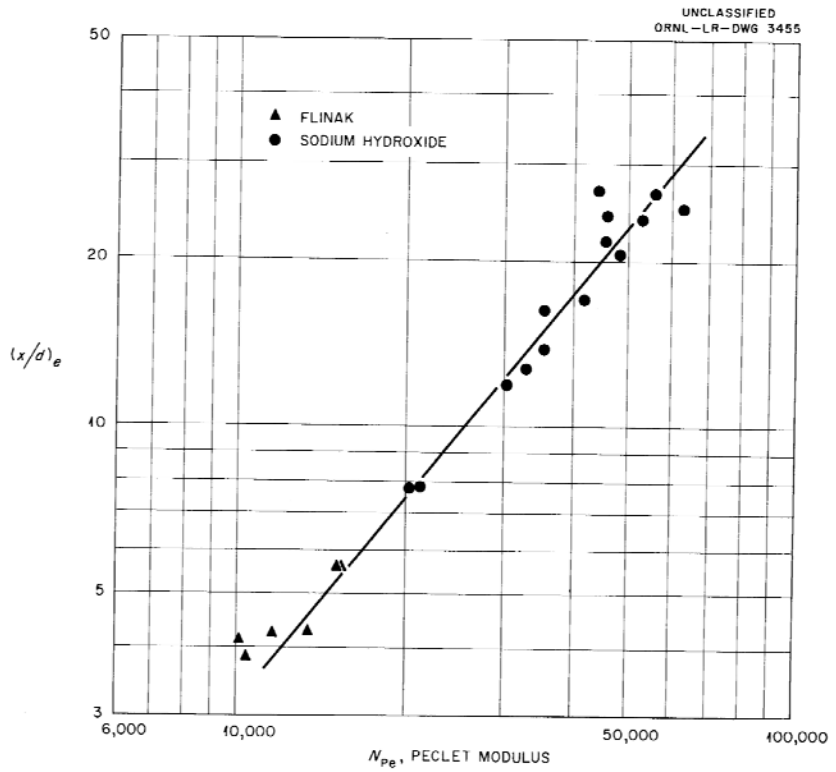

Fig. 35. Variation of thermal entrance length for flinak and sodim hydroxide with Peclet number.

The Hoffman's experimental setup also did not employ any corrosion control techniques.

As the knowledgebase on liquid salts developed, it was recognized that film formation on the inner surface of the Inconel test section with the flinak as the working fluid was expected unless corrosion control was used to reduce the chemical potential of fluorine.

Cooke and Cox [50]

Cooke and Cox later performed experiments on forced convection heat transfer for a proposed MSBR fuel salt LiF-BeF_2-ThF_4-UF_4 (67.5-20.0-12.0-0.5% mole). The test section consists of a horizontal tube made of smooth Hastelloy N 62.2 cm in length with a 6.35-mm outside diameter and 0.9-mm wall thickness. The range of variables included Reynolds number between 400 and 30,600, Prandtl number between 4 and 14, average bulk fluid temperature between 565°C and 843°C, and heat flux between 69.4 kW/m^2 and 1.77 MW/m^2. The inlet and outlet salt temperatures are measured by four Chromel-Alumel-sheated thermocouples inserted into two wells in each mixing chamber. The temperature distribution along the test section is measured by a series of 24 Chromel-Alumel thermocouples spot-welded at 2.5-cm intervals to the outside tube wall. The experimental data is shown in Fig. 36 along with the theoretical trends for normal heat transfer fluids. The results were found to be approximately 13% below the standard literature heat transfer correlations. This minor discrepancy was attributed to possible errors present in the thermophysical data.

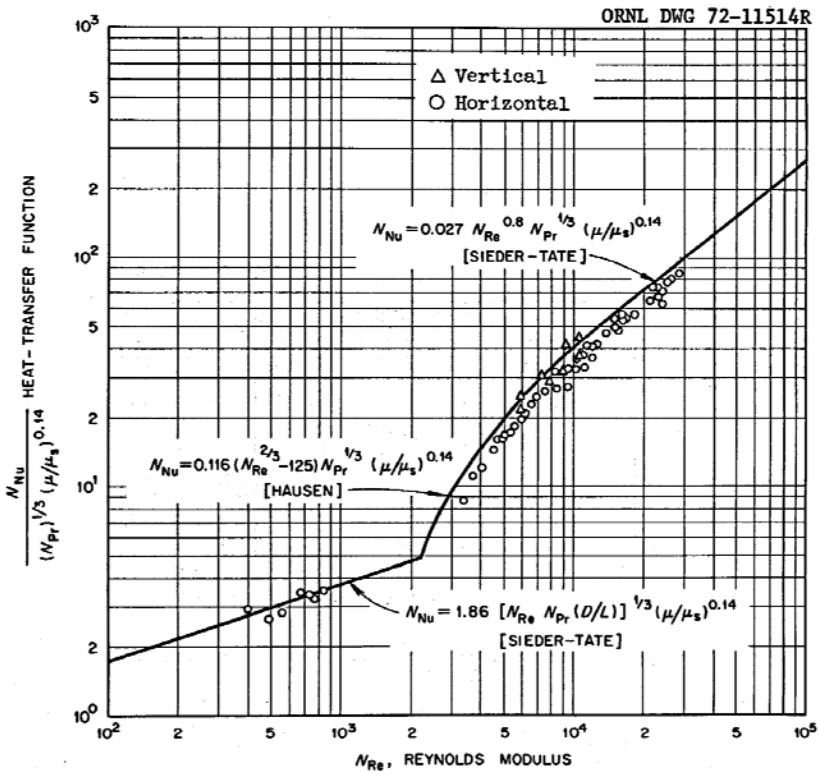

Fig. 36. Comparisons of the molten salt data obtained by Cooke and Cox [50].

The post-experiment investigations did not reveal any low-conductance film formation on the inner surface of Hastelloy N test section.

4.2 HEAT TRANSFER CORRELATIONS

Experimental measurements suggest that liquid salts behave as a normal fluid in the range $0.5 < \mathrm{Pr} < 100$ with regard to heat transfer for forced flow in the absence of natural circulation [61].

For laminar flow region (i.e., $\mathrm{Re} < 1000\ 0$, the Seider-Tate correlation or the Martinelli-Boelter correlation can be used:

$$Nu = 1.86 \left[\mathrm{Re}\ \ \mathrm{Pr}\ \left(\frac{D}{L}\right) \right]^{1/3} \left(\frac{\mu_B}{\mu_S}\right)^{0.14} \tag{4.3a}$$

$$Nu = 1.62 \left[\mathrm{Re}\ \ \mathrm{Pr}\ \left(\frac{D}{L}\right) \right]^{1/3} . \tag{4.3b}$$

For the transition region beyond the entrance region (i.e., $3500 < \mathrm{Re} < 12,000$), a modified form of the Hausen equation can be used:

$$Nu = 0.116\ \left(\mathrm{Re}^{2/3} - 125\right)\ \mathrm{Pr}^{1/3}\ \left(\frac{\mu_B}{\mu_S}\right)^{0.14} . \tag{4.4}$$

For the turbulent flow region (i.e., $\mathrm{Re} > 12,000$), correlations proposed by McAdams or Seider and Tate can be used:

$$Nu = 0.023\ \mathrm{Re}^{0.8}\ \mathrm{Pr}^{0.4} \tag{4.5a}$$

$$Nu = 0.027\ \mathrm{Re}^{0.8}\ \mathrm{Pr}^{1/3}\ \left(\frac{\mu_B}{\mu_S}\right)^{0.14} . \tag{4.5b}$$

Colburn proposed a slightly different correlation defined by

$$j = \mathrm{St}\ \mathrm{Pr}^{2/3} = 0.023\ \mathrm{Re}^{-0.2} , \tag{4.6}$$

which enables—under certain conditions—a direct comparison between heat transfer and friction. In this correlation, j is defined as the Colburn j-factor, and St is the Stanton modulus defined by

$$\mathrm{St} = \frac{h}{c_p G} . \tag{4.7}$$

The Colburn correlation—also called Colburn-Chilton analogy—is based on correlations and data rather than on assumptions about transfer mechanisms, and is one of the most widely used analogies in heat transfer.

Note that all of the correlations given above are applicable only at moderate ΔT conditions.

5. OPERATION AND MAINTENANCE ISSUES

5.1 STARTUP PROCEDURES

Recommended startup procedures for LSHT loops are based on those documented by Crowley et al. in 1963 [64]. Initial loop startup begins with equipment and instrumentation checkout. The performance of all electrical, instrumentation, and control circuits are validated and the loop is measured to be leak tight by monitoring loop pressure changes from an introduced inert gas overpressure. The entire loop is then preheated to roughly 100°C above the salt melting point with the pump shaft rotating slowly. A clean-up batch of salt at a temperature slightly higher the loop is then forced into the piping by providing an inert gas over pressure to the drain tank. The cleanup salt is used to remove the oxide scale and any other fluoride-soluble deposits from the surface of the loop. The inert gas that initially fills the loop is vented at the upper portion (expansion tank) of the loop. The drain tank level gauge indicates when sufficient salt has been introduced into the loop.

The progress of salt filling is indicated by the temperature readings of thermocouples placed along the loop. Level probes at the pump and expansion tank indicate when the loop is full. The freeze valve on the interconnecting line between the drain-supply tank and loop is then chilled externally with airflow. The initial cleaning batch of salt is circulated for at least two hours. The freeze valve on the drain-supply tank is then reheated; pressure is then applied to the upper portion of the loop via expansion tank valve and the cleanup salt is collected in its supply tank. A key system design constraint is to avoid catch pockets were salt will not drain from the loop. Once the cleanup salt has resolidified, the salt tank is replaced with a clean batch of salt to be used in the measurements. The testing salt is introduced into the loop via the same procedure as the initial cleanup salt.

A less favored alternative to employing salt scale removal is to use an acid based pickling process. An advantage of the acid based processes is that they take place at low temperatures. However, acid pickling of nickel alloys employ concentrated nitric and hydrofluoric acids and evolve noxious gases. Consequently, pickling of nickel alloys requires significant attention to the process safety. Pickling process details are alloy dependent and are available from the alloy manufacturer [65] or in the case of stainless steels have been codified into a standard [66].

5.2 ACTIVE REDOX CORROSION CONTROL

In addition to initially removing impurities from the salt before use, the electrochemical fluorine potential of the salt can be adjusted on-line to compensate for changes during operation. Water pick-up through incidental atmospheric exposure is a typical salt contamination route. The essence of reduction–oxidation control in a liquid fluoride salt is minimization of the fluorine potential by providing plentiful, energetically preferential reaction sites within the melt for any free fluorine that develops. In other words, the redox potential of the salt is kept highly reducing to prevent oxidation of the container by fluorine atoms.

The container metal atoms are generally in their most reduced phase. Consequently, the salt can be maintained in a highly reducing condition without concern for providing an alternative corrosion mechanism. If, however, the loop includes carbon components under strongly reducing conditions the salt will attack the carbon (i.e., lithium and carbon can combine to create lithium carbide under sufficiently reducing conditions). The salt itself can also become reduced (i.e., sodium can plate out from flinak) if the salt environment becomes too strongly reducing.

One technique to decrease the fluorine potential is to provide a Lewis acid to the melt. For beryllium-based salts the salt would be allowed to corrode metallic beryllium both providing an excess of an

electropositive element as well as a Lewis acid to complex fluoride ions [80]. Other less toxic Lewis acids such as zirconium (as in NaF-ZrF_4) also provide some protective effect [22].

The impact of beryllium addition on thermally driven corrosion and mass transport between 650ºC and 525ºC in a stainless steel 316 natural convection loop containing a molten mixture of LiF–BeF_2 (66-34 mole %) is shown in Fig. 37 [81]. The presence of excess metallic reductant (beryllium) reduced the corrosion rate to less than 2 µm/year over the 2000-h test period. The change in the slope of the *as received* salt near 1000 hours of exposure shows the impact of impurities on the corrosion rate. Once sufficient electropositive impurities (chiefly chromium) have been corroded from the container wall to bind with the electronegative impurities in the salt the rate of corrosion decreases (but still remains roughly four times that of a reducing environment salt).

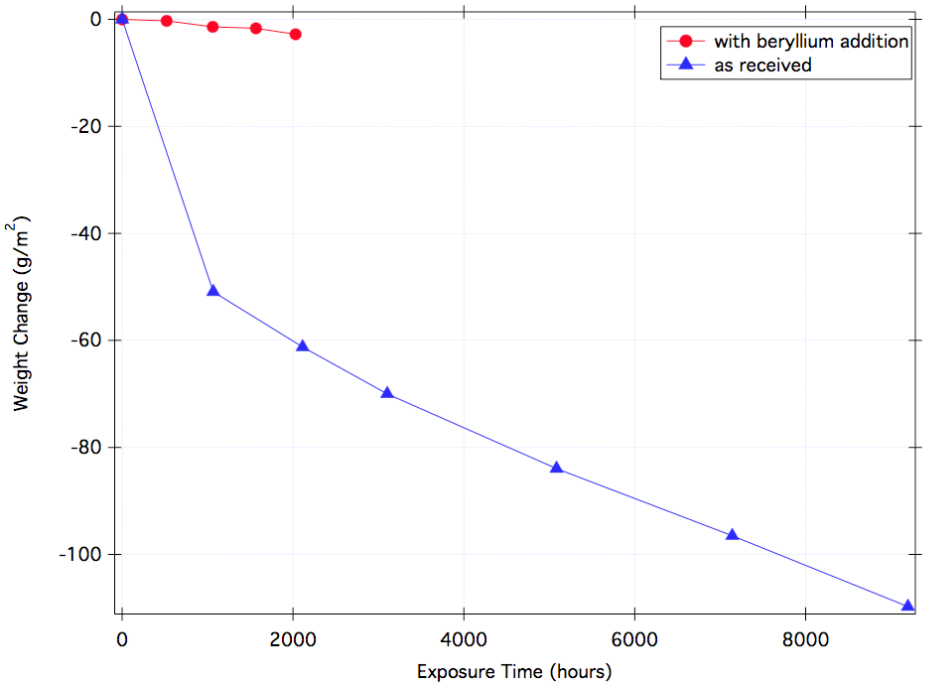

Fig. 37. Weight change with exposure for Type 316 stainless steel in LiF-BeF_2 (66-34 mol %) at 650ºC. (adapted from Ref. 81)

Nonprimary constituent Lewis acids have also been shown to be effective in removing structural metals from salt melts [82]. Fig. 38 shows the reduction of dissolved chromium in a LiF-BeF_2 (66-34 mol %) melt at 600ºC resulting from additions of zirconium metal to the melt. While the individual experimental results are promising, high-temperature, multicomponent chemical processes (particularly those involving temperature gradients and moving fluids) are complex, and significantly more investigation is required to be able to establish Lewis acid addition-based corrosion control recommendations for specific material combinations, temperatures, and geometries.

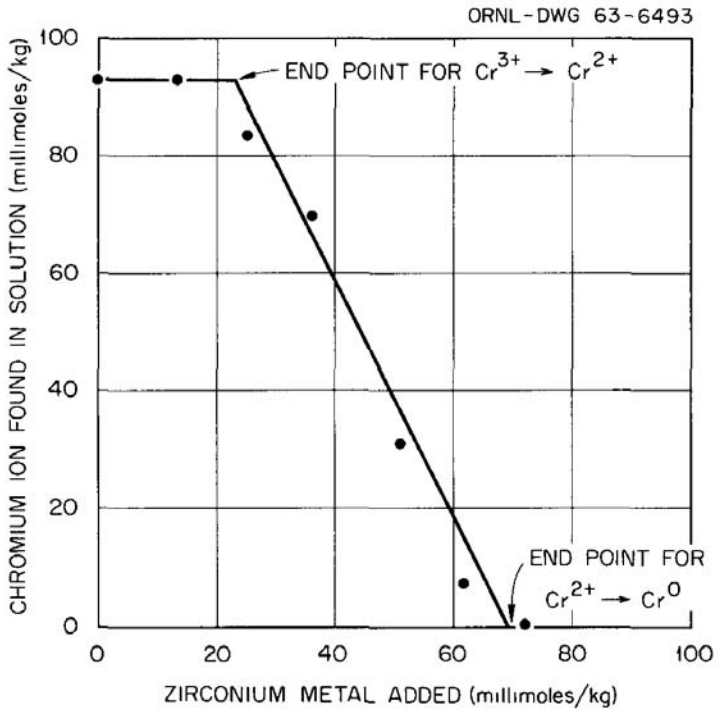

Fig. 38. Removal of chromium from solution in LiF-BeF_2 (66-34 mol %) at 600ºC by addition of zirconium metal.

A critical step in corroding nickel-based alloys in liquid fluoride salts is dissolving chromium into the salt. Dissolving chromium into the salt oxidizes neutral metallic chromium into a doubly positively charged ion leaving behind two electrons and negatively charging the remaining metal. The oxidation process can be inhibited electrochemically.

The exterior salt container will almost inevitably be electrically connected to ground. In order to establish a potential difference within the melt, and, thereby force a reducing environment at the container wall a second electrode (anode) electrically connected to the salt is required. The anode is held negative relative to the container wall (cathode). Electrons thus flow into the container wall to neutralize electropositive material deposition. Impressed current cathodic protection is in widespread, common industrial use.

The magnitude of the applied voltage necessary to provide cathodic protection depends upon the elements involved and the temperature of the materials. Standard electrode potentials for the structural and salt elements of interest at 25ºC are given in Table 12 [83]. The voltage difference between the anode (polarizing electrode) and cathode (container wall) needs to be held between the chromium and sodium half-cell potentials ($-0.91 > \Delta V > -2.71$) so that chromium remains reduced on the wall and sodium remains oxidized in the melt. The cell standard electrode potential, $\mathcal{E}$, is a convenient representation of the change in the Gibbs energy accompanying the cell reaction:

$$\Delta G = -n\, e\, N_A\, \mathcal{E}\ , \tag{5.1}$$

where n represents the number of electrons exchanged in the reaction, N_A is Avogadro's number, and e is the charge of an electron.

Table 12. Standard electrode potentials at 25ºC

Element	Electrode potential (V)
Fluorine	+2.87
Carbon	+0.207
Nickel	–0.25
Iron	–0.44
Chromium	–0.913
Sodium	–2.71
Potassium	–2.93
Lithium	–3.04

A power supply is required to provide the necessary current and voltage to maintain the required potential difference. While no current is required from the power supply to prevent chemical reactions, once the initial bias is established, leakage current will flow through the salt due to its electrical resistance. The electrical resistivity of flinak varies from 0.74 Ω-cm at 600ºC to 0.57 Ω-cm at 800ºC [84, 85]. Depending upon the electrode geometry and temperature, a significant amount of current may be required to maintain the potential difference. Both the voltage difference required and resultant current distribution to maintain a reducing environment at the container wall shifts due to the difference in the change in the Gibbs energy and electrical resistivity of the salt and container material with temperature.

Graphite is an appropriate large-area electrode material for fluoride salts. As a rule-of-thumb, no more than roughly 100 mA/cm^2 should be employed with a carbon electrode or excessive voltage drop at the electrode surface and consequent undesirable electrochemical reactions (e.g., CF_4 evolution) may occur.

Alternatively, a multivalent buffer element with a standard electrode redox reaction potential difference between that of chromium and sodium can be employed to shift the electrochemical potential of the salt. In this case a small amount of a multivalent element is added to the salt (10^{-2} M to 10^{-3} M concentration) [86]. The multivalent element initially reacts with the salt to become a fluoride and is then reduced within the salt by contacting it with an electrode maintained at a negative voltage using a large contact area flow electrode. For example, ytterbium has both 2+ and a 3+ oxidation states. The YbF_3 gains an electron at the electrode, reducing it to YbF_2. The ytterbium in the flowing salt can then donate an electron to capture a fluorine ion.

For systems where all of the container materials are in their most reduced phase (metals) the salt can be maintained in a highly reducing condition. To provide redox control and avoid either reducing the salt itself or carbon container materials, however, provision needs to be made to measure the redox condition of the melt. Redox condition measurement can be performed either optically or electrochemically. Often a third, smaller electrode using the same material as the driven electrode is employed in electrochemical cells to form a potentiostat.

5.3 TRITIUM CONTROL

A fluoride salt heat transfer loop may receive tritium through its primary heat exchanger as hydrogen readily diffuses through applicable heat exchanger metals at temperature. Dissolved tritium contamination can be removed from the liquid salt by transfer of the tritium into another phase within the heat transport loop, subsequent separation the second phase material from the liquid salt, and then chemical trapping of the tritium.

If the tritium is chemically bound to a salt atom it must first be converted to a gas molecule to enable removal from the stream. Reacting the salt containing the bound tritium with a sacrificial metal (e.g., Fe, Cr, W) yields dissolved tritium gas.

$$2\,{}^{3}HF \;+\; M \;\rightleftharpoons\; {}^{3}H_2 \;+\; MF_2 \;. \tag{5.2}$$

The use of beryllium to remove dissolved ^{3}HF from flibe under a generation rate of 1.2×10^{18} molecules/m^{3}s has been experimentally shown to keep the ^{3}HF concentration well below 20 parts per trillion [67].

Sparging the salt stream with inert gas (argon) bubbles promotes tritium transfer to the gas phase due to concentration-driven diffusion. Coupling high power ultrasonic energy into the salt encourages tritium bubble nucleation and subsequent buoyancy-driven gas evolution. The combination of sparging and ultrasonic degassing promotes rapid evolution of dissolved gas [68]. The tritium can then be stripped from the evolving gas bubbles by reacting the gas with a hydrogen trap such as titanium sponge to form a solid metal hydride [69].

6. CONCLUSIONS

Heat transport is at the core of many important industrial processes. The efficiency and expense of transporting heat vary strongly with the heat transfer medium selected. High-temperature, low-pressure, heat-transport systems are not yet commercial items and thus development risk accrues for any technology selected. Fluoride salts are a leading candidate heat-transport material at high temperatures.

This report provides a high-level, parametric evaluation of LSHT loop performance to allow intercomparisons between heat-transport fluid options as well as providing an overview of the properties and requirements for a representative loop. A compilation of relevant thermophysical properties of candidate heat transport fluoride salts is also included in the report. This report also provides a discussion of loop operational issues such as start-up procedures, system freeze-up vulnerability, and tritium removal techniques (as would likely be required when the heat source is a nuclear reactor.

Low-pressure, high-boiling point liquids have large advantages in terms of both pumping power and piping mass (capital cost) for high-temperature heat transport. Of the materials evaluated, at 700°C both sodium and flinak would be viable options as heat transport media with principal salt advantages of lack of stored chemical energy and being optically transparent. Superficially, fluoride salt under operating conditions resembles water at near room temperature with similar heat capacity, roughly three times the viscosity, and about twice the density. This report does not provide an exhaustive screening of potential heat transfer media and other high-temperature liquids such as alkali metal carbonate eutectics or chloride salts would also be useful heat transfer media options.

Candidate heat-transport fluoride salts have been extensively used in specialized industrial processes for decades. Further, as combinations of highly electropositive and highly electronegative elements the salts are both thermally stable and with proper chemistry control can be relatively chemically inert. Fluoride salts can, however, be highly corrosive depending on the container materials selected, the salt chemistry, and the operating procedures used. Fluoride salt chemistry control has shown great promise for corrosion prevention in the limited set of material combinations under which it has been deployed. However, chemistry control is not sufficiently technologically mature to be confidently deployed as a general-purpose tool for corrosion prevention.

Much of the understanding of LSHT derives from the earlier MSR program and one advantage of selecting fluoride salts for a heat transport system is the relative technological maturity of these systems due to the prior development efforts. While over the intervening decades revolutionary improvements have occurred in several areas of science and technology to a large extent the resultant improved materials, components, and instrumentation have not yet been applied to LSHT.

REFERENCES

1. J. P. Sanders, *A Review of Possible Choices for Secondary Coolants for Molten Salt Reactors*, ORNL CF 71-8-10, Oak Ridge National Laboratory, Oak Ridge, TN, August 1971.
2. http://www.aluminumsmeltingprocess.com/.
3. K. Abe et al., "Development of Advanced Blanket Performance under Irradiation and System Integration through JUPITER-II Project," *Fusion Eng. Design*, **83**, pp. 842–849 (2008).
4. J. R. Keiser, J. H. DeVan, and D. L. Manning, *The Corrosion Resistance of Type 316 Stainless Steel to Li_2BeF_4*, ORNL/TM-5782, Oak Ridge National Laboratory, Oak Ridge, TN, April 1977.
5. W. Simka, D. Puszczyk, and G. Nawrat, "Electrodeposition of Metals from Non-Aqueous Solutions," *Electrochimica Acta*, **54**, pp. 5307–5319 (2009).
6. G. Ett and E. J. Pessine, "Pulse Current Plating of TiB_2 in Molten Fluoride," *Electrochimica Acta*, **44,** pp. 2859–2870 (1999).
7. C. B. Davis, R. B. Barner, S. R. Sherman, and D. F. Wilson, *Thermal-Hydraulic Analyses of Heat Transfer Fluid Requirements and Characteristics for Coupling a Hydrogen Product Plant to a High-Temperature Nuclear Reactor*, INL/EXT-05-00453, Idaho National Laboratory, Idaho Falls, ID, June 2005.
8. D. E. Holcomb, S. M. Cetiner, G. F. Flanagan, F. J. Peretz, and G. L. Yoder, Jr., *An Analysis of Testing Requirements for Fluoride Salt-Cooled High Temperature Reactor Components*, ORNL/TM-2009/297, Oak Ridge National Laboratory, Oak Ridge, TN, November 2009.
9. P. Hejzlar, V. Dostal, M. J. Driscoll, P. Dumaz, G. Poullennec, and N. Alpy, "Assessment of Gas Cooled Fast Reactor with Indirect Supercritical CO_2 Cycle," *Nuclear Engineering Technology—Special Issue on ICAPP'05*, **38**(2), pp. 109–118 (2006).
10. P. G. Smith, *Development of Fuel- and Coolant-Salt Centrifugal Pumps for the Molten-Salt Reactor Experiment*, ORNL-TM-2987, Oak Ridge National Laboratory, Oak Ridge, TN, October 1970.
11. *PRISM—Preliminary Safety Information Document*, GEFR-00793 (UC-87Ta), Volumes I–VI, General Electric–Advanced Nuclear Technology, San Jose, CA, December 1987.
12. G. A. Carlson, W. H. Sullivan, and H. G. Plein, "Application of Ultrasonic Thermometry in LMFBR Safety Research," *1977 IEEE Ultrasonics Symposium Proceedings*, pp. 24–8, Phoenix, AZ, October 26–28, 1977.
13. L. C. Lynnworth and E. H. Carnevale, "Ultrasonic Thermometry Using Pulse Techniques," *Temperature: Its Measurement and Control in Science and Industry*, Instrument Society of America, **4**(1), pp. 715–32 (1972).
14. L. C. Lynnworth, *Ultrasonic Measurements for Process Control*, Academic Press, Inc., pp. 369–447 (1989).
15. D. Nagle and Y-R. Rhim, "Carbide Coatings for Nickel Alloys and Carbon/Carbon Composites to be Used in Fluoride Salt Valves," FY10 proposal submitted to U.S. Department of Energy under Nuclear Energy University Program (NEUP), Johns Hopkins University, Whiting School of Engineering.

16. P. G. Smith, *Experience with High Temperature Centrifugal Pumps in Nuclear Reactors and their Application to Molten-Salt Thermal Breeder Reactors*" ORNL-TM-1993, Oak Ridge National Laboratory, Oak Ridge, TN, September 1967.

17. Y. Guojun, X. Yang, S. Zhengang, and G. Huidong, "Characteristic Analysis of Rotor Dynamics and Experiments of Active Magnetic Bearing for HTR-10GT," *Nuclear Engineering and Design*, **237**, pp. 1363–1371 (2009).

18. R. V. Major and V. Samadian, "Physical Metallurgy and Properties of a New High-Saturation Co-Fe Alloy," *Journal of Materials Engineering*, **11**(1), pp. 27–30 (1989).

19. W. Li, X. Yang, Z. Lei, and W Xinxin, "Impact Analysis of the Catcher Bearing for the Magnetic Suspending Rotor in HTR10-GT Project," in *2nd International Topical Meeting on High Temperature Reactor Technology*, Beijing, China, September 22–24, 2004.

20. R. B. Bird, W. E. Stewart, and E. N. Lightfoot, *Transport Phenomena*, Revised Second Edition, John Wiley & Sons, Inc., New York, 2007.

21. M.-H. Li, A. B. Palazzolo, A. Kenny, A. J. Provenza, R. F. Beach, and Albert F. Kascak, "Fault-Tolerant Homopolar Magnetic Bearings," *IEEE Transactions on Magnetics*, **40**(5), pp. 3308–3319 (September 2004).

22. D. F. Williams, *Assessment of Candidate Molten Salt Coolants for the NGNP/NHI Heat-Transfer Loop*, ORNL/TM-2006/69, Oak Ridge National Laboratory, Oak Ridge, TN, June 2006.

23. D. F. Williams, L. M. Toth, and K. T. Clarno, *Assessment of Candidate Molten Salt Coolants for the Advanced High-Temperature Reactor (AHTR)*" ORNL/TM-2006/12, Oak Ridge National Laboratory, Oak Ridge, TN, March 2006.

24. H. F. McMurdie et al., "Phase Diagrams for Ceramists," National Bureau of Standards, *Multivolume Compilation*, American Ceramic Society.

25. A. D. Kelmers, *Evaluation of Alternate Secondary (and Tertiary) Coolants for the Molten-Salt Breeder Reactor*" ORNL/TM-5325, Oak Ridge National Laboratory, Oak Ridge, TN, 1976.

26. W. R. Grimes, *Chemical Research and Development for Molten-Salt Breeder Reactors*, ORNL/TM-1853, Oak Ridge National Laboratory, Oak Ridge, TN, 1967.

27. M. Morishita, K. Koyama, M. Murase, and Y. Mori, "Improvement in the Electrodeposition of Corrosion Resistance of Zinc-plated Magnesium from a Molten Salt," *ISIJ International*, **36**(6), pp. 714–719 (1996).

28. G. J. Janz, *Molten Salts Handbook*, Academic Press, NY, 1967.

29. K. A. Sense, C. A. Alexander, R. E. Bowman, and R. B. Filbert, Jr., "Vapor Pressure and Derived Information of the Sodium Fluoride-Zirconium Fluoride System: Description of a Method for the Determination of Molecular Complexes Present in the Vapor Phase," *Journal of Physical Chemistry*, **61**(3), pp. 337–344 (March 1957).

30. K. A. Sense and R. W. Stone, "Vapor Pressures and Molecular Composition of Vapors of the Sodium Fluoride–Beryllium Fluoride System," *Journal of Physical Chemistry*, **62**(4), pp. 453–457 (April 1958).

31. D. F. Williams et al., "The Influence of Lewis Acid/Base Chemistry on the Removal of Gallium by Volatility from Weapons Grade Plutonium Dissolved in Molten Chlorides," *Nuclear Technology*, **136**, p. 367 (2001).

32. W. R. Grimes, *Reactor Chemistry Division Annual Progress Report for Period Ending December 31, 1965*, ORNL-3913, Oak Ridge National Laboratory, Oak Ridge, TN, 1966.

33. A. Klemm, "Transport Properties of Molten Salts," in *Molten Salt Chemistry*, edited by M. Blander, John Wiley and Sons, Inc., New York, 1964.

34. S. Cantor, W. T. Ward, and C. T. Moynihan, "Viscosity and Density in Molten LiF-BeF_2 Solutions," *Journal of Chemical Physics*, **50**(7), p. 2874 (1969).

35. S. I. Cohen, W. D. Powers, and N. D. Greene, *Viscosity Measurements on Molten Fluoride Mixtures*, ORNL-2278, Oak Ridge National Laboratory, Oak Ridge, TN, 1957.

36. C. T. Moynihan and S. Cantor, "Viscosity and its Temperature Dependence in Molten BeF_2," *Journal of Chemical Physics*, **48**(1), p. 115 (1968).

37. T. Grande, S. Aasland, and S. Julsrud, "Some Comments on the Thermodynamic Aspects of Glass Formation in Fluoride Systems," *Journal of Non-Crystalline Solids*, **184**, p. 114 (1995).

38. J. Lucas, "Fluoride Glasses," *Journal of Material Science*, **24**, p. 1 (1989).

39. T. Grande, H. A. Oye, and S. Julsrud, "Viscosity and Density of Molten Barium Zirconate and Related Melts," *Journal of Non-Crystalline Solids*, **161**, p. 152 (1993).

40. K. Torlep and H. A. Oye, "Viscosity of Eutectic LiF-NaF-KF," *Journal of Chemical Engineering Data*, **25**, p. 16 (1980).

41. E. Veliyulin, A. Voronel, and H. A. Oye, "Universal Features in the Viscosity Behavior of Salt Melts and Their Mixtures," *Journal of Physics: Condensed Matter*, **7**, p. 4821 (1995).

42. K. Cornwell, "The Thermal Conductivity of Molten Salts," *Journal of Physics D: Applied Physics*, **4**, pp. 441–45 (1971).

43. E. McLaughlin, "Thermal Conductivity of Liquids and Dense Gases," *Chemical Reviews*, **64**, pp. 389–428 (1964).

44. D. T. Jamieson et al., *Liquid Thermal Conductivity: A Data Survey to 1973*, National Engineering Laboratory, Her Majesty's Stationary Office, Edinburgh, 1975.

45. C. H. Gabbard, *Reactor Power Measurement and Heat Transfer Performance in the Molten Salt Reactor Experiment*, ORNL-TM-3002, Oak Ridge National Laboratory, Oak Ridge, TN, 1970.

46. J. W. Cooke, *Development of the Variable-Gap Technique for Measuring the Thermal Conductivity of Fluoride Salt Mixtures*, ORNL-4831, Oak Ridge National Laboratory, Oak Ridge, TN, 1973.

47. J. W. Cooke, *Experimental Determination of the Thermal Conductivity of Molten Fluoride Mixtures*, ORNL CF 66-5-1, Oak Ridge National Laboratory, Oak Ridge, TN, 1966.

48. U.S. Atomic Energy Commission, *Reactor Handbook Vol. 4: Engineering*, edited by S. Mclain and J. H. Martens, p. 53, Interscience Publishers, NY (1964).

49. M. W. Rosenthal, P. N. Haubenreich, and R. B. Briggs, *The Development Status of Molten Salt Breeder Reactors*, ORNL-4812, Oak Ridge National Laboratory, Oak Ridge, TN, 1972.

50. J. W. Cooke and B. W. Cox, *Forced-Convection Heat Transfer Measurements with a Molten Fluoride Salt Mixture Flowing in a Smooth Tube*, ORNL-TM-4079, Oak Ridge National Laboratory, Oak Ridge, TN, 1973.

51. V. Ignatiev et al., "Transport Properties of Molten Salt Reactor Fuel Mixtures," paper presented at *Actinide and Fission Product Partitioning Transmutation—7th Information Exchange Meeting*, Jeju, Korea, October 14–16, 2002.

52. J. McDonald and H. T. Davis, "Determination of the Thermal Conductivities of Several Molten Alkali Halides by Means of a Sheathed Hot Wire Technique," *Physics and Chemistry of Liquids*, **2**, pp. 119–134 (1971).

53. M. V. Smirnov et al., "Thermal Conductivity of Molten Alkali Halides and Their Mixtures," *Electrochimica Acta*, **31**(7), p. 1019 (1987).

54. V. A. Khoklov, E. S. Filatov, A. Solheim, and J. Thonstad, "Thermal Conductivity in Cryolitic Melts: New Data and its Influence on Heat Transfer in Aluminum Cells," in *Light Metals 1998—Proceedings of the Technical Sessions presented by TMS Light Metals Committee at the 127th TMS Annual Meeting*, San Antonio, Texas, pp. 501–506, February 15–19, 1998.

55. M. Blander, "Thermodynamic Properties of Molten Salt Solutions," in *Molten Salt Chemistry*, edited by M. Blander, Interscience Publishers—A Division of John Wiley and Sons, New York, 1964.

56. D. J. Rogers, T. Yoko, and G. J. Janz, "Fusion Properties and Heat Capacities of the Eutectic LiF-NaF-KF," *Journal of Chemical Engineering Data*, **27**, p. 366 (1982).

57. M. W. Rosenthal, H. F. Poppendiek, and R. M. Burnett, *A Method for Evaluating the Heat Transfer Effectiveness of Reactor Coolants*, ORNL CF 54-11-63, Oak Ridge National Laboratory, Oak Ridge, TN, November 1954.

58. H. W. Hoffman, *Preliminary Results on Flinak Heat Transfer*, ORNL CF 53-8-106, Carbide and Carbon Chem. Co., Oak Ridge, TN, August 1953.

59. H. W. Hoffman, *Molten Salt Heat Transfer*, ORNL CF 58-2-40, Oak Ridge National Laboratory, Oak Ridge, TN, February 1958.

60. M. D. Grele and L. Gedeon, *Forced Convection Heat Transfer Characteristics of Molten Flinak Flowing in an Inconel X System*, RM E53L18, National Advisory Committee for Auronautics, Washington, DC, February 1954.

61. H. W. Hoffman and J. Lones, *Fused Salt Heat Transfer, Part II: Forced Convection Heat Transfer in Circular Tubes Containing NaF-KF-LiF Eutectic*, ORNL 1777, Oak Ridge National Laboratory, Oak Ridge, TN, February 1955.

62. W. E. Kirst, W. M. Nagle, and J. B. Castner, "A New Heat Transfer Medium for High Temperatures," *Trans. American Inst. Chem. Eng. (AIChE)*, **36**, pp. 371–394 (1940).

63. H. F. Poppendick, *Physical Property Charts for Some Reactor Fuels, Coolants and Miscellaneous Materials*, ORNL CF 54-6-188, Oak Ridge National Laboratory, Oak Ridge, TN, June 1954.

64. J. L. Crowley, W. B. McDonald, and D. L. Clark, *Design and Operation of Forced-Circulation Corrosion Testing Loops with Molten Salt*, ORNL-TM-528, Oak Ridge National Laboratory, Oak Ridge, TN, May 1963.

65. http://www.specialmetals.com/documents/fabricating.pdf, pp. 30–35.

66. ASTM A380–06, "Standard Practice for Cleaning, Descaling and Passivation of Stainless Steel Parts," *Equipment and Systems*, ASTM International, West Conshohocken, PA.

67. M. F. Simpson, G. R. Smolik, J. P. Sharpe, R. A. Anderl, D. A. Petti, Y. Hattano, M. Hara, Y. Oya, S. Fukada, S. Tanaka, T. Terai, and D. Sze, "Quantitative Measurement of Beryllium-

Controlled Redox of Hydrogen Fluoride in Molten Flibe," *Fusion Engineering and Design*, **81**, pp. 541–547 (2006).

68. H. Xu, Q. Han, and T. T. Meek, "Effects of Ultrasonic Vibration on Degassing of Aluminum Alloys," *Materials Science and Engineering A*, **473**, pp. 96–104 (2008).

69. S. H. Lee and H. Chung, "Characteristics of Hydrogen Absorption by Zirconium and Titanium," *Journal of Industrial and Engineering Chemistry*, **6**(6), pp. 380–384 (November 2000).

70. L. V. Woodcock, "Some Quantitative Aspects of Ionic Melt Microstructure," in *Proceedings of the Royal Society of London. Series A*, Mathematical and Physical Sciences, The Royal Society (1972).

71. W. D. Manly et al., "Metallurgical Problems in Molten Fluoride Systems," *Progress in Nuclear Energy*, Series IV, **2**, pp. 164–179 (1960).

72. J. H. DeVan and R. B. Evans III, *Corrosion Behavior of Reactor Materials in Fluoride Salt Mixtures*, ORNL/TM-328, Oak Ridge National Laboratory, Oak Ridge, TN, 1962.

73. W. D. Manly, J. H. Coobs, J. H. DeVan, D. A. Douglas, H. Inouye, P. Patriarca, T. K. Roche, and J. L. Scott, "Metallurgical Problems in Molten Fluoride Systems," pp. 223–234 in *Proceedings of the Second U.N. International Conference on the Peaceful Uses of Atomic Energy*, **Volume 7—Reactor Technology**, Geneva, , September 1–13, 1958.

74. M. Kondo, T. Nagasaka, A. Sagara, N. Noda, T. Muroga, Q. Xu, M. Nagura, A. Suzuki, and T. Terai, "Metallurgical Study on Corrosion of Austenitic Steels in Molten Salt LiF-BeF_2 (Flibe)," *Journal of Nuclear Materials*, **386–388**, pp. 685–688 (2009).

75. R. B. Evans III, J. H. DeVan, and G. M. Watson, *Self-Diffusion of Chromium in Nickel-Base Alloys*, ORNL-2982, Oak Ridge National Laboratory, Oak Ridge, TN, 1960.

76. J. R. Keiser, *Compatibility Studies of Potential Molten-Salt Breeder Reactor Materials in Molten Fluoride Salts*, ORNL/TM-5783, Oak Ridge National Laboratory, Oak Ridge, TN, May 1977.

77. J. H. Shaffer, *Preparation and Handling of Salt Mixtures for the Molten Salt Reactor Experiment*, ORNL-4616, Oak Ridge National Laboratory, Oak Ridge, TN, January 1971.

78. J. R. Hightower, Jr., "Predicted Corrosion Rates in Continuous Fluorinators Employing Frozen-Wall Protection," *Engineering Development Studies for Molten-Salt Breeder Reactor Processing*, No. 9, ORNL-TM-3259, Oak Ridge National Laboratory, Oak Ridge, TN, December 1972.

79. J. R. Hightower, Jr., "Frozen-Wall Fluorinator Development: Experiments on Induction Heating in a Continuous Fluorinator Simulation," in *Engineering Development Studies for Molten-Salt Breeder Reactor Processing*, No. 10, ORNL-TM-3352, Oak Ridge National Laboratory, Oak Ridge, TN, December 1972.

80. P. Calderoni, P. Sharpe, H. Nishimura, and T. Terai, "Control of Molten Salt Corrosion of Fusion Structural Materials by Metallic Beryllium," *Journal of Nuclear Materials*, **386–388**, pp. 1102–1106 (2009).

81. J. R. Keiser, J. H. DeVan, and E. J. Lawrence, "Compatibility of Molten Salts with Type 316 Stainless Steel and Lithium," *Journal of Nuclear Materials*, **85–86**, pp. 295–298 (1979).

82. J. H. Shaffer, *Preparation and Handling of Salt Mixtures for the Molten Salt Reactor Experiment*, ORNL-4616, Oak Ridge National Laboratory, Oak Ridge, TN, January 1971.

83. P. Vanýsek, “Electrochemical Series,” in *Handbook of Chemistry and Physics: 66th Edition*, Chemical Rubber Company (1985).

84. N. D. Greene, *Measurements of the Electrical Conductivity of Molten Fluorides*, ORNL CF 54-8-64, Oak Ridge National Laboratory, Oak Ridge, TN, August 1954.

85. S. I. Cohen, W. D. Powers, and N. D. Greene, *A Physical Property Summary for ANP Fluoride Mixtures*, ORNL-2150, Oak Ridge National Laboratory, Oak Ridge, TN, August 1956.

86. G. D. Del Cul, D. F. Williams, L. M. Toth, and J. Caja, “Redox Potential of Novel Electrochemical Buffers useful for Corrosion Prevention in Molten Fluorides,” in *Proceedings of the Thirteenth International Symposium on Molten Salts*, held during the 201st meeting of the Electrochemical Society, Philadelphia, PA, May 12–17, 2002.

INTERNAL DISTRIBUTION

1. J. T. Busby (busbyjt@ornl.gov)
2. M. S. Cetiner (cetinerms@ornl.gov)
3. W. R. Corwin (corwinwr@ornl.gov)
4. G. F. Flanagan (flanagangf@ornl.gov)
5. J. C. Gehin (gehinjc@ornl.gov)
6. S. R. Greene (greenesr@ornl.gov)
7. D. E. Holcomb (holcombde@ornl.gov)
8. D. T. Ingersoll (ingersolldt@ornl.gov)
9. G. T. Mays (maysgt@ornl.gov)
10. C. V. Parks (parkscv@ornl.gov)
11. F. J. Peretz (peretzfj@ornl.gov_
12. J. E. Rushton (rushtonje@ornl.gov)
13. J. C. Wagner (wagnerjc@ornl.gov)
14. D. F. Williams (williamsdf2@ornl.gov)
15. G. L. Yoder, Jr. (yodergljr@ornl.gov)
16. ORNL Laboratory Records—RC (hamrindr@ornl.gov)

EXTERNAL DISTRIBUTION

17. M. H. Anderson, University of Wisconsin, 737 Engineering Research Building, 1500 Engineering Drive, Madison, WI 53706 (manderson@engr.wisc.edu)
18. Richard L. Black, NE-3/Germantown Building, U.S. Department of Energy, 1000 Independence Ave., SW., Washington, DC 20585-1290 (richard.black@hq.doe.gov)
19. C. W. Forsberg, Massachusetts Institute of Technology, MIT Nuclear Fuel Cycle Study Department of Nuclear Science and Engineering, 77 Massachusetts Ave., Room 24-207a, Cambridge, MA 02139 (cforsber@mit.edu)
20. P. F. Peterson, University of California–Berkeley, Nuclear Engineering Department, 4153 Etcheverry Hall, Berkeley, CA 94720-1730 (Peterson@nuc.berkeley.edu)
21. R. D. Scheele, Pacific Northwest National Laboratory, P. O. Box 999, Richland, WA 99352 (randall.scheele@pnl.gov)
22. Richard A. Kendall, NE-74/Germantown Building, U.S. Department of Energy, 1000 Independence Ave., S.W., Washington, DC 20585-1290 (rick.kendall@nuclear.energy.gov)